Atomic and Molecular Adsorption on Superconducting Pb as Basis for the Realization of Qubits

Inauguraldissertation

zur

Erlangung der Würde eines Doktors der Philosophie

vorgelegt der

Philosophisch-Naturwissenschaftlichen Fakultät

der Universität Basel

von

Carl Drechsel

2022

Originaldokument gespeichert auf dem Dokumentenserver der Universität Basel
edoc.unibas.ch

Genehmigt von der Philosophisch-Naturwissenschaftlichen Fakultät
auf Antrag von:

Prof. Dr. Ernst Meyer
Prof. Dr. Martino Poggio
Prof. Dr. Katharina J. Franke

Basel, den 22. Juni 2021

Prof. Dr. Marcel Mayor, Dekan

"*Das Schönste aber hier auf Erden*
ist lieben und geliebt zu werden."

Wilhelm Busch (1832 – 1908)

Abstract

Just as bits are the basic unit for conventional computers, qubits are the basic unit for quantum computers. They are expected to model quantum mechanical systems such as large molecules, unfeasible with today's computational resources. This thesis presents measurements regarding to two platforms, which are seen as suitable for their implementation: Majorana bond states (MBS) in topological superconductors and quantum dots (QDs).

As a basis for both approaches, atomic and molecular adsorption on superconducting Pb surfaces is investigated with the use of scanning probe methods (SPM). Since promising results for atomic Fe chains on Pb surfaces have already indicated the existence of an MBS, it is the aim of this thesis, to gain further knowledge about the adsorption of CO, NaCl and Fe on Pb surfaces. This might be relevant for future experiments to perform high-resolution imaging or to build atomic chains by moving single atoms in a controlled way over the surface.

A second aim of this thesis is to investigate 2D molecular layers, self-assembled on Pb, that show strong evidence for the confinement of electrons. Hence, they act as single-electron transistors and can be seen as molecular QDs. In summary, the measurements in this thesis draw attention on the high potential that Pb might offer for the realization of qubits.

Kurzbeschreibung

So wie Bits als Basiseinheit für herkömmliche Computer dienen, sind Qubits die Basiseinheit für Quantencomputer. Mit ihnen sollen sich quantenmechanische Systeme, wie z.B. grössere Moleküle, modellieren lassen, was mit der heutigen Rechenleistung undurchführbar ist. In dieser Arbeit werden Messergebnisse an zwei Fallbeispielen vorgestellt, die zur Realisierung von Qubits als geeignet angesehen werden: Dies sind einerseits gebundene Majoranazustände (MBS) in topologischen Supraleitern und andererseits Quantenpunkte (QDs).

Als Grundlage für beide Ansätze wird die atomare und molekulare Adsorption auf supraleitenden Pb-Oberflächen mit Hilfe von Rastersondenmikroskopie (SPM) untersucht. Da für atomare Fe-Ketten auf Pb-Oberflächen bereits vielversprechende Ergebnisse auf die Existenz eines MBS hinweisen, ist es ein Ziel dieser Arbeit, weitere Erkenntnisse zur Adsorption von CO, NaCl und Fe auf Pb-Oberflächen zu gewinnen. Dies könnte für zukünftige Experimente relevant sein, um z.B. eine hochauflösende Bildgebung zu erzielen oder durch die kontrollierte Verschiebung einzelner Atome atomare Ketten auf der Oberfläche zu bilden.

Ein zweites Ziel dieser Dissertation ist die Untersuchung von selbstorganisierten 2D-Molekülschichten auf Pb, die starke Hinweise auf das Confinement von Elektronen zeigen. Sie wirken als Transistoren für einzelne Elektronen und können daher als molekulare QDs angesehen werden. Zusammenfassend machen die Messungen dieser Arbeit auf das hohe Potential aufmerksam, das Pb bei der Realisierung von Qubits bieten kann.

Contents

Abstract / Kurzbeschreibung **v**

Introduction **1**

1 Techniques: Scanning Probe Microscopy **5**
1.1 Scanning Tunneling Microscopy (STM) 6
1.1.1 Tunneling Effect 7
1.1.2 Operating the STM 10
1.1.3 Scanning tunneling spectroscopy (STS) 12
1.2 Atomic Force Microscopy (AFM) 13
1.2.1 Interaction forces between tip and sample 14
1.2.2 Operating the AFM 17
1.2.3 Kelvin probe force microscopy (KPFM) 18
1.3 Summary 20

2 Setup & Implemetation **21**
2.1 Setup of the Ultra High Vacuum System 21
2.1.1 Preparation Chamber 22
2.1.2 Sublimation of atoms and molecules 23
2.2 Cryostat and Low-temperature Scanning probe microscope 24
2.2.1 Tuning-fork sensor 25
2.2.2 Preparation of the tip 26
2.2.3 Modification of the tip 27
2.2.4 Measurement control and evaluation software 28
2.3 Preparation of clean Pb samples 28
2.4 Adsorption of single atoms and molecules 30
2.4.1 Adsorption of single Fe-atoms 30
2.4.2 Adsorption of TBPP molecular layers 30
2.5 Summary 31

3 Basics of Majorana bound states & molecular quantum dots **33**
3.1 Introduction to Superconductivity and Majorana bound states (MBS) . 33
3.1.1 Bardeen-Cooper-Schrieffer theory 34
3.1.2 Properties of superconducting Pb 35
3.1.3 Magnetic impurities on superconductors 36
3.1.4 MBS in engineered topological superconductors 37
3.1.5 Detection of MBS by SPM techniques 38
3.2 Introduction to single-electron charging and molecular quantum dots . 43
3.2.1 Single-electron transistors (SETs) 43
3.2.2 Quantum dots (QDs) 44
3.2.3 Detection of quantum dots by SPM techniques 45
3.2.4 Quantum dots in molecular layers 48
3.3 Summary 51

4 Adsorption of CO, NaCl & Fe on Pb surfaces **53**
4.1 CO adsorption on bare Pb surfaces 54
4.2 Growth of NaCl islands on Pb(111) 57
4.3 Adsorption and manipulation of Fe atoms on Pb(111) 58
4.4 Summary 60

5 Charge state control of molecular quantum dots on Pb **61**
5.1 Self-assembled layers of TBPP on Pb(111) 62
5.1.1 Structure determination of TBPP/Pb(111) by STM & AFM . . 62
5.1.2 Influence of bias voltage on TBPP/Pb(111) 64
5.2 Arrays of Coulomb rings in molecular TBPP layers 66
5.2.1 Influence of bias voltage on Coulomb rings 66
5.2.2 Influence of tip-sample distance on Coulomb rings 70
5.2.3 Distance dependence of the charge transfer based on dI/dV . . . 73
5.3 Frequency shift due to Coulomb rings 74
5.3.1 Influence of tip-sample distance on Coulomb rings in AFM . . . 74
5.3.2 Distance dependence of the charge transfer based on AFM . . . 76
5.4 Summary 76

Conclusion **79**

Bibliography **81**

Nomenclature **103**

Acknowledgements **107**

List of publications & communications **109**

Curriculum Vitae **111**

Introduction

Approximately since the end of the 1990s, the increasing transformation from analog data processing to digital systems is known as *"digital revolution"*. It marks a technological change that, analogous to industrialization, has radical effects on almost all areas of human life. An essential basis for this change is the continuous miniaturization of microprocessors, which has massively improved the performance of digital machines. Since the first development of integrated circuits in 1958 (by later Nobel Prize winner Jack Kilby) their integration density (number of transistors per unit area) has always doubled within ca. 2 years. In 1965, this regularity was observed by Gordon Moore and became famous as "Moore's law" [1]. For a long time "Moore's Law" served as a key motivation of leading companies to maintain the high pace of this persistent progress. Although Moore predicted in 2007 an end of this regularity for ca. 2020, the development so far seems to be continuing with the development of a metal-oxide-semiconductor field-effect transistor (MOSFET) featuring a gate length of 5 nm. However, in the next few years, further miniaturization must inevitably slow down and come to a complete end, since the gates of the transistors would have separations of only a few atomic radii and therefore become influenced by quantum mechanical uncertainty [2]. In addition, higher integration densities cause due to waste heat negative effects on the operational stability [1, 3].

A possible continuation of the digital revolution could therefore consist in a paradigm shift towards a new basic unit for all computing processes: While until now computers use bits as the smallest information unit, which can assume exactly one of two possible states, an information unit based on quantum mechanical principles, so-called quantum bits (*qubits*), consist of a superposition of both states [4]. Only at an instant measurement the superposition collapses into one of the two states. Furthermore, the qubits can be entangled, which means that multiple qubits exist in a single quantum state and a change to the state of one qubit also changes instantaneously all the qubits entangled to it. Hence, the measurement of one single qubit enables a direct deduction of the properties from all qubits entangled with it.

The advantage of qubits can be exemplified with the comparison of 4 bits: While 4 classical bits represent exactly one out of $2^4 = 16$ possible combinations, 4 entangled qubits can assume all 16 combinations at the same time. This synchronized processing of several calculation steps enables quantum computers an enormous time advantage in iterative processes. It becomes evident in the comparison of a sequence of classical logical gates with quantum gates: While a classical gate generates exactly one definitive output per calculation step, a quantum gate processes probabilities and generates a superposition of them as output. Due to the entanglement of qubits, the execution of one single calculation step would also solve all other steps at the same time.

However, it is questionable whether this advantage plays a role in everyday computer use. Much more, quantum computers could offer an enormous advance in the simulation of material properties, which is even with today's supercomputers very intense and lacks accuracy [5]. This would possibly enable the individual design of specific drugs or molecules that are superconducting at room temperature. Another area of application could be the search in very large databases or the further development of cryptographic methods, since previous methods could be decrypted by entangling a large number of qubits [6].

The implementation of powerful quantum computers in practice is still failing due to two major problems: On the one hand, it is very difficult to keep a qubit in the state of superposition, since it can be influenced by small thermal fluctuations changes, radiation or even the earth's magnetic field. The duration, in which the superposition can be maintained in a controlled manner is known as the coherence time. On the other hand, the entanglement becomes more difficult with each new qubit added, as their states become more and more difficult to control. To illustrate the order of magnitude, in which the realization seems to be possible, reference can be made to recent publications by Google with an entanglement of 53 qubits and a coherence time of 12 ns [7] as well as IBM with an entanglement of 65 qubits and a coherence time of 71 µs [8]. Both companies have already announced to realize significant progress on that within the next two years. The huge interest in improving the implementation of quantum computers is also expressed by the worldwide rapidly growing private and state investments in this area [9].

The most cited approach, how qubits can be realized, was presented in 1998 by Daniel Loss and David DiVincenzo [10]. In their concept, the spin of an electron contained in a quantum dot (QD) is used as a qubit and is based on the gate voltage between two coupled single-electron QDs. It causes exchange operations and local magnetic fields and thus creates a controlled NOT gate (CNOT), which is necessary for entangling the qubits. More details on this concept as well as on first experimental implementations can be found in the review by Christoph Kloeffel and Daniel Loss [11].

Due to the high sensitivity of the spin to external influences, a certain stability is desirable when looking for further systems to realize qubits. In 2001, Alexei Kitaev published a model [12] that uses the Majorana fermion, a particle described by Ettore

Majorana in 1937 that is also its own anti-particle [13], as the basis for qubits. Another article by Liang Fu and Charles L. Kane from 2008 postulated the realization of such Majorana bound states (MBS) in the ends of atomic chains on s-wave superconductors [14]. Shortly afterwards, the first experimental implementation of MBS succeeded and this model is also seen as very promising for the creation of qubits [15].

In order to achieve superconductivity, however, temperatures in the cryogenic range are necessary, which usually requires a greater effort and higher expenses. But apart from that, the low temperatures foster the implementation of qubits, since they prevent thermal fluctuations. Additionally, the use of superconductors offers due to the Meissner-Ochsenfeld effect the advantage that external magnetic fields are displaced [16] and thus works against another disturbing influence.

Scanning probe microscopy (SPM) has played a significant role in the implementation and observation of MBSs, as it enables atomic resolution of the entire system of superconductor and chain as well as the localization of MBSs in the sub-nm range [17–19]. Additionally, it allows in situ modifications by manipulating individual atoms [20, 21]. In recent years it has been shown, that SPM methods can also be used to characterize QDs. The addition or removal of individual single electrons in QDs can namely be observed in SPM on the basis of charge rings that represent individual energy levels of the QD [22–26]. Since the formation of charge rings has also been shown in the case of individual organic molecules, it can be assumed that these behave analogously as molecular QDs [27–30].

A connection between both topics, MBSs and QDs, is not only given by qubits as a shared domain of application, but can also be made by the use of superconducting Pb as substrate. The superconductor Pb is characterized by its high critical temperature ($T_C = 7.2$ K), which is the third highest among elementary superconductors. In the past, it was already well known for its low melting point ($\Theta = 327.4$ °C) and its malleability, which made it to a widely used metal. One of the most famous uses of Pb is the manufacture of leaded water pipes, which began in the Roman Empire and continued into the 20th century. The English word "plumber", for example, can be traced back to the Latin word for lead "plumbum" and explains the element symbol "Pb". Lead was also of great importance for the creation of scriptures: The use of lead pencils goes e.g. back to the Romans and Johannes Gutenberg's invention of movable lead letters for book printing from 1450 is seen as a prerequisite for the scientific revolution and the beginning of modernity. Later it was widely used in projectiles for weapons, as color pigments and as a gasoline additive to increase knock resistance.

In the 19th century, for the first time the consequences of Pb poisoning were discussed in broader public, as it turned out that Pb can be stored in bones and blood, which can lead to severe damage to the nervous and cardiovascular systems. The harmful effects of Pb became more apparent in the course of the 20th century. Its use as a gasoline additive (in particular from ≈1920-1980) led to an enormous increase of Pb pollution in the air and e.g. the Pb amount in human bones increased tenfold com-

pared to bone samples from ancient times. For this reason, more and more restrictions and bans arose on the use of Pb. A first success of these measures can be already demonstrated by the decrease in the measured Pb concentration of air and water. For example, the average Pb pollution in the Rhine at Basel fell from over 2.0 µg/l in the 1980s to below 0.5 µg/l in the 2010s [31]. Today, in industrialized countries Pb is used almost exclusively in applications that exclude the formation of Pb-containing dust or waste water. The most common applications are car batteries or shielding devices against radioactive radiation.

Aware of the harmful effects on human health, the use of Pb with any direct contact to people must be avoided in the future. Nevertheless, mankind could continue to benefit from its advantages: For example, the implementation of qubits based on Pb only requires extremely small amounts of material and emissions into the environment can be completely ruled out. The relatively high critical temperature could even be a decisive advantage over other superconductors, since cooling down to the LT range requires a very high amount of energy. Furthermore, Pb is commonly occurring on earth compared to other elements, since its isotopes Pb-206, Pb-207 and Pb-208 are at the end of the three natural decay series of radioactive elements.

Considering the great importance of quantum computers for the progress of the digital revolution, the question arises nowadays, whether Pb as a promising basis for the implementation of qubits can once again serve as a door opener into a new technological era for mankind. Hence, in this thesis two promising platforms to realize qubits, the adsorption of Fe atoms on Pb for the creation of MBSs and the adsorption of TBPP molecules for achieving molecular QDs, are investigated.

In chapter 1, the concept and development of SPM, which is the basic technique used for all presented measurements, is described in details. In chapter 2 the setup of the microscope the experimental implementation and the preparation of the samples is explained. Then, in chapter 3 a detailed review on superconductivity and the theory as well as the experimental confirmation of MBSs is given. In addition to that, the phenomenon of single-electron charging, which is the basis of QDs, is presented and the literature on SPM-related investigations is discussed. In chapter 4, results on the adsorption of CO, NaCl and Fe on Pb surfaces are presented as basis for future experiments to perform high-resolution imaging or to create atomic chains of Fe on Pb. Finally, in chapter 5, the observation of molecular QDs is reported. Here, SPM-methods are applied to show a signature for single-electron charging and fulfill thereby a charge state control.

1 Techniques: Scanning Probe Microscopy

The basis of any experimental work is a precise knowledge and control of the measurement methods used. For this reason, the following chapter gives a description of the experimental methods used in this work, all of which can be classified as part of the so-called *Scanning Probe Microscopy* (SPM). The decisive factor with this type of microscopy is that, in contrast to light or electron microscopy, the measurement is made by using a fine probe (tip). It is located on a scanner, which is moved in a grid pattern over a surface. The interaction between tip and surface provides information about the nature of the sample, namely by measuring a tunneling current (see section 1.1) or atomic forces (see section 1.2). Magnetic, thermal, chemical, or other interactions can also be considered for SPM, but this is beyond the scope of this thesis.

SPM was developed in 1981 by a team from IBM Zurich Research Laboratory (Gerd Binnig, Heinrich Rohrer, Christoph Gerber and Edmund Weibel) with the first successful tunneling experiment through a vacuum gap [32]. As decisive criterion, why this experiment was successful in contrast to previous ones, the authors indicate the suppression of vibrations and external oscillations, which was achieved through excellent decoupling of the scanner. For all SPM methods, damping plays a crucial role to obtain atomic resolution.

Another characteristic of SPM is the use of piezoelectric drive elements. Only with their help the scanner can be moved over the surface with atomic precision and thus a high resolution can be guaranteed. The piezoelectric effect was first discovered by Jacques and Pierre Curie in 1880 [33] and describes that in the event of a deformation for certain materials an electrical voltage occurs (direct piezo effect), or when an electrical voltage is applied, a deformation takes place (inverse piezo effect).

For SPM measurements always the inverse piezo effect is used. In total, three piezo elements are required to move the scanner: an x- and a y-piezo to position the tip in the plane of the sample surface and a z-piezo to adjust the distance between sample and

tip. Usually, lead zirconate titanate (PZT) with the chemical formula $Pb[Zr_xTi_{1-x}]O_3$ ($0 \leq x \leq 1$) is used as piezo material, since this exhibits a high voltage/deformation-sensitivity. However, the piezoelectric response is strongly temperature-dependent, so even a small variety in the temperature causes a significant drift. With falling temperatures the sensitivity decreases, but remains even at low temperatures good enough for SPM measurements [34].

In this work, the main focus is the atomic-scale characterization of adsorbates on superconducting surfaces and the exploration of charge states. For this reason, the characteristics of applying SPM on superconductors (see section 3.1.5) and exploring charge states with STM (see section 3.2.3) is explained in particular detail by reference to the state of the art.

1.1 Scanning Tunneling Microscopy (STM)

The principle behind the first tunneling experiment through a vacuum gap [32, 35] is based on an electric bias voltage between tip and sample and the approach of a very thin probe (ideally atomically thin tip) close to the surface until a so called *tunneling current* starts to flow between sample and tip. This current is caused by the quantum-mechanical tunneling effect, which depends on the distance between sample and tip and also on the density of electronic states (DOS) at the surface and at the tip. In fig. 1.1, the principle of the tunneling is shown by an energy scheme. A more detailed description of the theory behind the quantum-mechanical tunneling effect is given in section 1.1.1.

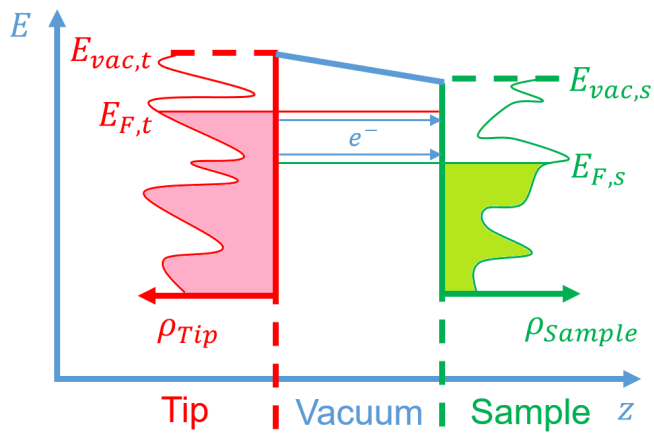

Figure 1.1: *Energy scheme of an barrier tunnel junction: E_F denotes the Fermi level, which is the highest occupied state and E_{vac} is the vacuum level. The difference $E_{vac} - E_F$ defines the work function ϕ, which is the minimal energy to remove an electron into the vacuum. The distribution in the density of states ρ shows the filled and unfilled states. At very small distances between tip and sample, electrons can tunnel from the filled states of the tip into the unfilled states of the sample.*

Shortly after the successful tunneling experiment, Gerd Binnig, Heinrich Rohrer and their team added to the tip the ability to scan over a sample surface and developed thus *Scanning Tunneling Microscopy* (STM). Their first STM publication dealt with topographies of $CaIrSn_4$(110)- and Au(110) surfaces [36]. Special attention was received in 1983, when Binnig and Rohrer reported on the first real space determination of the Si(111)-(7×7) surface [37]. In 1986 they were awarded on that account with the Nobel Prize in Physics.

In the following years STM became a key method for analyzing the morphology of conductive surfaces. Regarding to the content of this work, further mile stones with STM were the following: In 1987 R. S. Becker *et al.* reported about first surface modifications at atomic scale caused by the STM tip [38]. Shortly after, in 1990, Don M. Eigler and Erhard K. Schweizer used STM for a first lateral manipulation by building "IBM" with single Xe atoms on a Ni(110) surface [39]. With the decoupling of adatoms from metallic surfaces by using ultrathin, insulating NaCl layers, Jascha Repp *et al.* showed in 2004 by adding or removing single electrons the control of the charge state of Au adatoms on Cu surface [40]. One year later he used this decoupling to image the orbitals of pentacene molecules [41].

A more precise description about operating an STM is given in section 1.1.2. The concept of *Scanning Tunneling Spectroscopy* (STS), which is the measurement of the tunneling current depending on various voltages at a distinct position, is described in section 1.1.3.

1.1.1 Tunneling Effect

With the occurrence of quantum mechanics in the 1920s, the concept of quantum mechanical tunneling was developed. According to this, a particle has a certain probability to overcome a potential barrier, although it has a lower energy than the peak of the barrier. Graphically, the particle behaves as if it was using a tunnel through the barrier. According to Eugen Merzbacher's investigation [42] the term "tunneling" was first used by Walter Schottky [43] and Jacov (Yakov) Frenkel [44] for this process.

By interpreting molecular spectra, Friedrich Hund was in 1927 able to give the first characterization of a tunneling effect with bound states [45, 46] and in 1928 Lothar Nordheim published the first article on the penetration of a barrier into an energy continuum [47]. The first general expression of the tunneling current in condensed matter Physics was published in 1930 by Jacov Frenkel [48].

Meanwhile, the theoretical treatment of the tunneling current became quite diverse and depends strongly on the given constraints. In the following paragraphs the main principle of the quantum-mechanical tunneling current is illustrated. For a more detailed description, the established textbooks of Roland Wiesendanger [49] and C. Julian Chen [50] are recommended.

The easiest way to describe the tunneling process is to consider an electron in an one-dimensional potential $V(z)$ and to assume the electron as wave function $\psi(z)$, that satisfies the Schrödinger equation:

$$\left[-\frac{\hbar^2}{2m}\frac{d^2}{dz^2}+V(z)\right]\psi(z)=E\psi(z) \tag{1.1}$$

Here, m and E represent mass and energy of the electron. For an one-dimensional potential barrier $V_0 > E$ with the separation width $s = 2a$, as shown in figure 1.2 b), the Schrödinger equation is solved in three different parts: on the left of the barrier, inside the barrier and on the right of the barrier. This results in the following transmission coefficient $T(E, V_0)$:

$$T(E,V_0)\approx\frac{16(V_0-E)}{V_0^2}\cdot \mathrm{e}^{-2s\frac{\sqrt{2m(V_0-E)}}{\hbar}} \tag{1.2}$$

The important result of this expression is the strong dependence of T from the exponential factor. For typical values, as $s = 5$ Å and $V_0 = 4$ eV, the exponential factor is $\approx 10^{-5}$. If the barrier width is reduced by only 1 Å, the exponential factor would increase by a factor of 10 [49], which demonstrates the high atomic precision of this method and explains the advantage of using the tunneling current to determine surface morphologies.

Bardeen Approach

A different approach to describe the tunneling process of electrons was published in 1961 by John Bardeen [51]. Instead of solving the Schrödinger equation for the total system, two subsystems (representing tip and sample) are considered. Then, the whole electron transfer rate is estimated by time-dependent perturbation theory. The time-independent state Ψ of each subsystem is determined by the eigenfunctions ψ_μ (for the occupied state) and χ_ν (for the unoccupied state). If both subsystems are apart from each other, ψ_μ and χ_ν decrease exponentially into the vacuum, as showed in figure 1.2 a).
However, if the distance between both systems is small enough for electrons to tunnel from occupied states in system A to unoccupied states in system B, the Schrödinger equation of each subsystem can be transformed in an equation of the whole system:

$$i\hbar\frac{\partial\Psi}{\partial t}=\left[-\frac{\hbar^2}{2m}\frac{\partial^2}{\partial z^2}+U_A+U_B\right]\Psi \tag{1.3}$$

Here, U_A and U_B represent the potential function of each system. However, a state ψ_μ of system A can now pass into a state of system B. Therefore a new wave function of the total system has to be formulated:

$$\Psi=\psi_\mu\exp\left(\frac{-iE_\mu t}{\hbar}\right)+\sum_{\nu=1}^{\propto}c_\nu(t)\chi_\nu\exp\left(\frac{-iE_\nu t}{\hbar}\right) \tag{1.4}$$

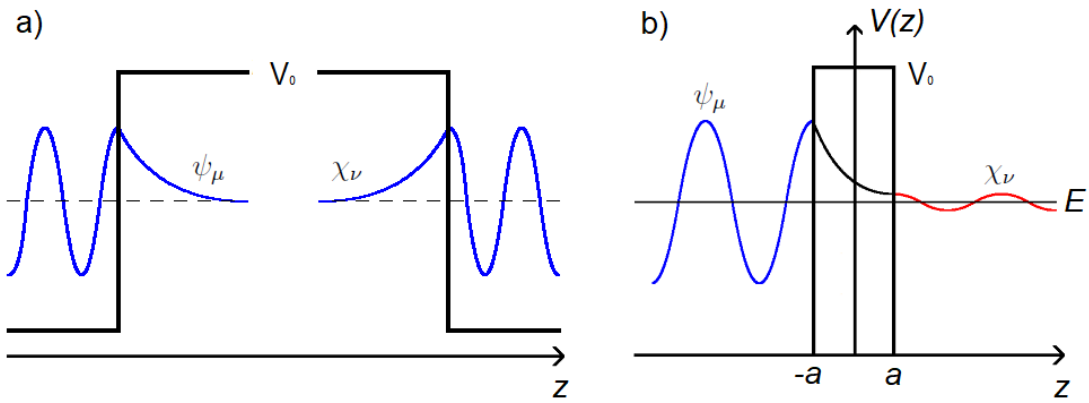

Figure 1.2: *Tunneling effect through an one-dimensional potential barrier V_0. a) Inside the barrier, the wave function of the electron on each site (ψ_μ and χ_ν) leaks exponentially out. If the barrier width is too large, no tunneling is possible. b) Reducing the barrier width enables a probability of appearing on the other site. The initial wave function of the filled state and the final wave function of the unoccupied state transfer through the barrier.*

The coefficient $c_\nu(t)$ with $c_\nu(0) = 0$ has to be determined by putting equation 1.4 in 1.3 and neglecting infinitesimal small parts. It follows:

$$c_\nu(t) = \frac{\exp\left(\frac{-i(E_\mu - E_\nu)}{\hbar}\right) - 1}{E_\mu - E_\nu} \cdot \int\limits_{z>z_0} \psi_\mu U_B \chi_\nu^* d^3\vec{r} = \frac{\exp\left(\frac{-i(E_\mu - E_\nu)}{\hbar}\right) - 1}{E_\mu - E_\nu} \cdot M_{\mu\nu} \tag{1.5}$$

By assuming an elastic tunneling process, which means, that tunneling is only possible into a state of the same energy ($E_\mu = E_\nu$) and extracting one derivative and evaluating the integral just at $z = z_0$, the typical form of Bardeen's tunneling matrix element can be determined:

$$M_{\mu\nu} = -\frac{\hbar^2}{2m} \int\limits_{z=z_0} \left(\chi_\nu^* \frac{\partial \psi_\mu}{\partial z} - \psi_\mu \frac{\partial \chi_\nu^*}{\partial z} \right) \tag{1.6}$$

With Bardeen's formalism, the tunneling current I is determined by first order time-dependent perturbation theory:

$$I = \frac{2\pi e}{\hbar} \sum_{\mu,\nu} \{ f(E_\mu)[1 - f(E_\nu + E_\mathrm{e})] - f(E_\nu + E_\mathrm{e})[1 - f(E_\mu)] \} \, \|M_{\mu\nu}\|^2 \rho_B(E_\mu) \tag{1.7}$$

Here, $f(E) = \{1 + \exp[(E - E_F)/(k_B T)]\}^{-1}$ corresponds to the Fermi function and E_e is the electric energy per electron caused by the applied sample bias voltage. The $\rho_B = \delta(E_\nu - E)$ represents the density of states (DOS) in subsystem B.

Tersoff-Hamann-Approximation

In 1983, Jerry Tersoff and Donald R. Hamann were the first, who applied Bardeen's approach with the tunneling matrix element explicitly to STM [52]. By assuming

limits of a small bias voltage and a low temperature they got from eq. 1.7:

$$I = \frac{2\pi e^2}{\hbar} U \sum_{\mu,\nu} \|M_{\mu\nu}\|^2 \rho_A(E_F)\rho_B(E_F) \tag{1.8}$$

It is remarkable that the ρ of both subsystems (representing sample and tip) contribute equally to the current. Here E_F indicates the Fermi energy.

The important approximation of Tersoff and Hamann is, to take also the tip shape into account. They approximated the tip's wave function as spherical potential, where the outermost atom has an s-wave function [52]. If the tip's density of states is ρ_A and the one of the sample is ρ_B, the charge density of electronic states at E_F is evaluated at the center of curvature of the closest tip-atom. Then for the tunneling current can be obtained:

$$I \propto U\rho_A(E_F)\rho_B(E_F)\exp(2\kappa r_0) \tag{1.9}$$

Here κ represents the decay rate $\kappa = (2m\Phi)/\hbar$ of the tip's local potential barrier height Φ and r_0 the radius of the closest tip-atom. So, the tunneling current is proportional to the local density of states at E_F, evaluated at the center of curvature of the tip.

$$I \propto U\rho_B(E_F, r_0) \tag{1.10}$$

Due to the fact, that the wave functions of tip and surface leak out exponentially, the tunneling current depends exponentially on the distance $r_0 + d$, or simply on the distance s between tip and surface.

$$I \propto \mathrm{e}^{-2\kappa s} \tag{1.11}$$

For higher bias voltages or non-s-wave functions, the Tersoff-Hamann-approximation is no longer valid. In this case, a finite bias can lead to distortions in the wave functions and energy eigenvalues of tip and sample. A more generalized approximation considering this was made by C. Julian Chen in 1988 [53].

To simplify the results of the different theories, Binnig et al. used for the tunneling current I, the following expression, that summarizes the main contribution [35]:

$$I = f(V_{\mathrm{Bias}}) \cdot \mathrm{e}^{-\sqrt{\overline{\phi}}\cdot s} \tag{1.12}$$

Here, $f(V_{\mathrm{Bias}})$ describes a weighted, local density of states for tip and sample, $\overline{\phi}$ is the averaged tunnel barrier height in eV and s is the distance between tip and sample.

1.1.2 Operating the STM

A typical setup of an STM is shown in fig. 1.3. At the beginning of an STM-measurement, the scanning unit is approached by eye close to the surface. After

applying a bias-voltage between 0 and $\approx \pm 2$ V, the approach of the tip is continued until a tunneling current starts to flow between sample and tip. Very common for this tunneling approach is a scanner of the so called *Besocke beetle type*, where the scanner approaches stepwise by applying consecutively voltage ramps on the piezoelectric feet of the scanner [54] [55].

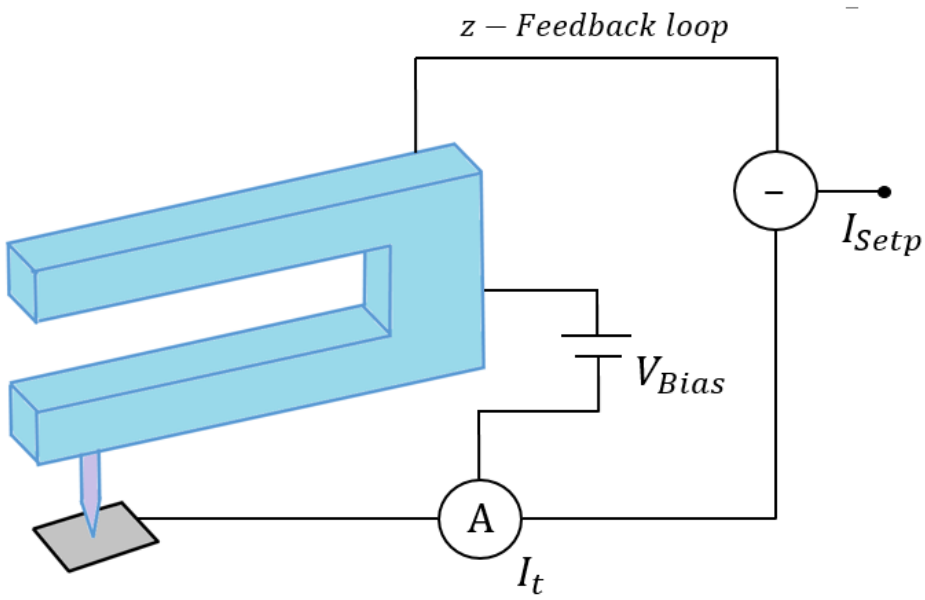

Figure 1.3: *Setup of a scanning tunneling microscope (STM) with tuning fork sensor. The bias voltage V_{bias} between sample and tip causes the tunneling current I_t, which can be put in relation to a setpoint current I_{setp} to keep a certain z-position.*

There are two different modes to operate an STM. If the STM is operated in the *constant height mode*, the distance between sample and tip remains constant over the complete scan and the tunneling current changes depending on the distance between tip and surface atoms.

However, if the STM is operated in the *constant current mode*, the current is maintained at a preset value (setpoint) and the z-position of the tip is regulated with a piezo by an electronic feedback, that keeps the distance between tip and sample dynamically constant. When the tip e.g. approaches to a terrace of the surface, the tunneling current changes due to the different sample-tip distance. This leads via feedback loop (see fig. 1.3) to a change of the sample-tip distance until the tunneling current is again equal to the setpoint. This permanent regulation of the tip is plotted as z-value of the surface morphology.

The advantage of the *constant current mode* is a safer scanning and a better vertical resolution. Whereas the *constant height mode* allows without regulations a higher scanning velocity, that can minimize the influence of thermal drift [56]. Fig. 1.4 shows the principles of both operating modes.

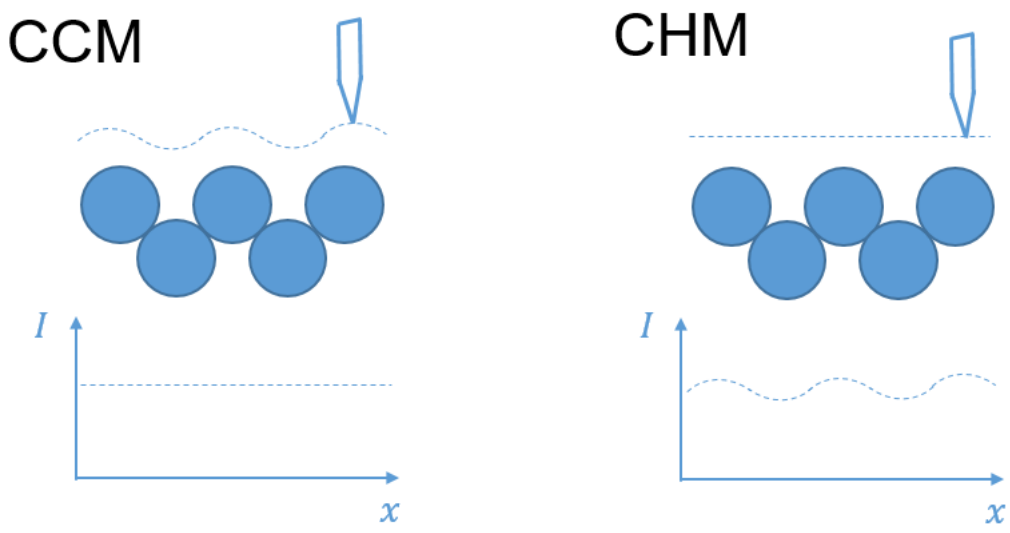

Figure 1.4: *Scheme of the two STM-operation-modes, constant current mode (CCM) and constant height mode (CHM): The tip movement in dependence of the surface morphology is contrasted to the related tunneling current I in dependence of the lateral position x.*

Regardless of the operating mode, the tip itself is very relevant for the STM-measurement: To gain an atomic resolution, the tip should ideally terminate in a single atom. Otherwise there could be additional imaging artefacts. The methods to improve a tip are described in section 2.2.2. The material of the tip should be conductive and rather hard, since otherwise an accidental contact between tip and sample could destroy the tip completely. Most widely used for STM-studies in UHV are tungsten tips; alternative materials are molybdenum (Mo), iridium (Ir) and platinum-iridium (Pt-Ir) [49].

1.1.3 Scanning tunneling spectroscopy (STS)

Shortly after topographic maps of surfaces constituted the success of STM, the attention to this technique was expanded to the dependence of the bias-voltage. As discussed in section 1.1.1 and summarized in equation 1.12, the tunneling current depends not only from the distance z between tip and sample, but from the arrangement of the electrons in real space (x,y), which is described as local density of states (LDOS). The LDOS itself depends from the bias voltage, since this is the electrical potential difference, that influences the energy of the electrons. Therefore, the measurement of a tunneling current depending on the bias voltage is called *tunneling spectroscopy* (TS).

Typically, the course of the curve I-V-curve rises for increasing voltages. Jumps in the tunneling current indicate when a new electronic state is filled. Determining the *differential conductance* (dI/dV), shows these jumps as peaks and displays for this reason the LDOS. It is equal to the distribution showed in figure 1.3. However, if the dI/dV-value is derived numerically from the I-V-curve, it might be dominated

by instrumental noise. An alternative is to measure the dI/dV by using the lock-in technique, that adds an AC voltage ($U_{\mathrm{LI}} = U_0 \cos(\omega_{\mathrm{LI}} t)$) to the DC bias voltage. The dI/dV-signal is measured by the lock-in amplifier, which detects the signal proportional to $\cos(\omega_{\mathrm{LI}} t)$ [57, 58]. Since this can be done simultaneously in the scanning constant current mode, the whole method is known as *scanning tunneling spectroscopy* (STS).

Another type of spectroscopy, that can be done with STM is $I_t(z)$-spectroscopy. Here, the tip is approached with a specific value z closer to the sample, which causes regarding to equation (1.12) an exponential increase at the tunneling current I_t. An example of a typical $I(z)$-curve is given in figure 2.5. The course of this curve provides information on the tip's quality, since artefacts at the tip would cause noise or jumps. It can also be used to modify the tip, as described in section 2.2.2. Furthermore, the local potential barrier can be obtained from the $I(z)$-curve [59].

1.2 Atomic Force Microscopy (AFM)

The development of *Atomic Force Microscopy* (AFM) can be seen as a direct consequence of the successful establishment of STM: A probe (tip), which is located on a cantilever, is brought into the influence of a surface, so that atomic forces between the tip and the sample become effective (a summary about the interacting forces is given in section 1.2.1). These interaction forces cause a deflection of the cantilever. In comparison to STM, AFM is independent of whether the sample is conductive. In their first publication about AFM from 1986, Gerd Binnig, Calvin F. Quate and Christoph Gerber described the use of an STM to detect this deflection of the cantilever [60]. There, the use of the STM causes the achievement of atomic resolution and outlines the innovation character of AFM compared to former stylus profilometer as developed in 1929 by Gustav Schmaltz [61] and improved by Russell D. Young (1971) [62] and E. Clayton Teague *et al.* (1982) [63]. A general overview of AFM, which was used as a basic reference for this work, can be found in the textbooks by Jacob N. Israelachvili [64] and Bert Voigtländer [65] or in the review by Franz J. Giessibl [66].

In the following years, AFM was developed enormously, so that today a large number of different operating modes exist. An overview on these modes is given is section 1.2.2. In 2016, the Kavli Foundation described AFM as "a breakthrough in measurement technology and nanosculpting that continues to have a transformative impact on nanoscience and technology" [67] and awarded Binnig, Gerber and Quate with the Kavli Prize.

Milestones in the development of AFM are the first quasi-atomically resolution by Ernst Meyer *et al.* (1989) [68], the introduction of contactless AFM through frequency modulation by Thomas R. Albrecht, Peter Grütter *et al.* (1991) [69], the atomic resolution of the Si(111)-(7×7) surface by Franz J. Giessibl (1995) [70] and the atomic resolution within molecules through tip functionalization by Leo Gross *et al.* (2009) [71].

An expansion of AFM is the *Kelvin Probe Force Microscopy*, where the atomic force is measured in dependence of the contact potential [72]. This and the related spectroscopy mode (KPFS), where the atomic force is measured in dependence from the bias voltage are described in section 1.2.3.

1.2.1 Interaction forces between tip and sample

The force amount, which is measured by AFM, is first of all dependent on the distance z between tip and sample and has different origins. For a first specification it can be differentiated on the basis of two attributes: The range of the forces (long-range or short range) and their effective direction (attractive or repulsive). Regarding to these attributes, figure 1.5 displays a classification of the most important interaction forces, which are discussed below.

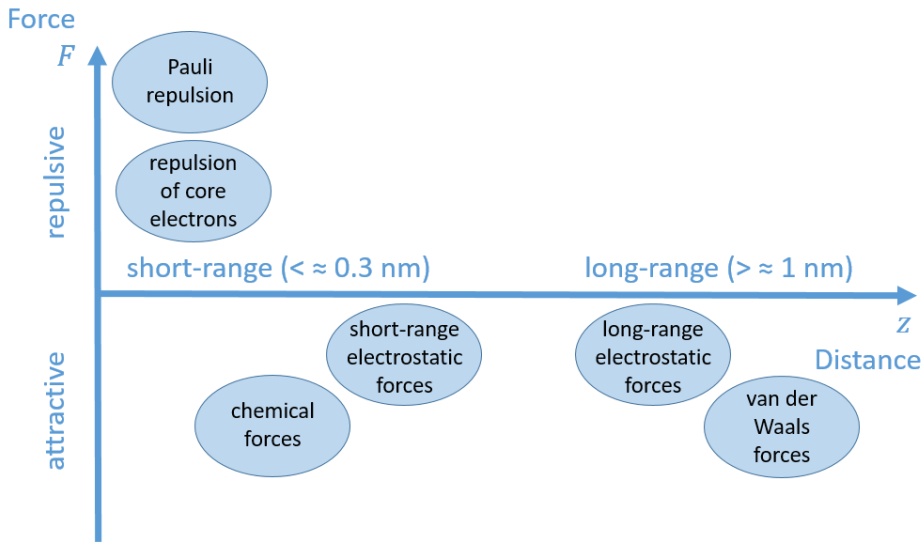

Figure 1.5: *Overview on the interacting forces within the gap of tip and sample classified by range (size of gap) and effective direction (amount of force).*

By reducing the gap between tip and sample up to ≈ 100 nm, the long-range forces start to appear [66]. Among them, the most dominant component is the **van der Waals force**. This term contains a combination of three different forces, which occur between two permanent molecular dipoles (Keesom forces), a permanent molecular dipole and a spontaneous formation of a dipole in a neutral molecule (Debye forces), or between two spontaneously induced dipoles in two neutral molecules (London forces). Their origin is from quantum mechanics and share a potential with z^{-6}-dependence from the tip-sample distance z. Usually, the London forces have the strongest influence, which results in a total attractive action for the van der Waals force. A very exact approximation is the description as so-called *Casimir-Polder force* [73], that deals with it as a quantum-electrodynamical phenomenon [65]. An easier approach assumes a spherical tip apex with radius R and summarizes the strength of the van der Waals

interaction for different materials in the so-called Hamaker constant H [64, 74]:

$$F_{\mathrm{VdW}}(z) = -\frac{H \cdot R}{6z^2} \tag{1.13}$$

Another kind of long-range interacting forces are attractive **electrostatic forces**, which appear due to the different electrostatic potential of tip and sample. This difference ΔV is also measured as *contact potential difference* (CPD) in force spectroscopy (see figure 1.8). To approximate these forces, the tip-sample system is seen as plate capacitor and the tip as sphere with radius R. From the electrostatic force E_{el} it follows with the vacuum permittivity ε [65, 75]:

$$F_{\mathrm{el}}(z, \Delta V) = -\frac{\partial E_{\mathrm{el}}(z)}{\partial z} = \frac{1}{2}\frac{\partial C(z)}{\partial z}(\Delta V)^2 = -\pi\varepsilon\frac{R^2}{z(z+R)}(\Delta V)^2 \tag{1.14}$$

Additionally, attractive electrostatic forces can also appear in the short-range regime [76]. This can be explained as local charge distributions in single molecules or charge states of adatoms [77, 78]. A more detailed description about the background and the detection of charge states with AFM and other SPM-methods is given in section 3.2).

The main component of the total force between tip and sample in the short-range regime is caused by attractive **chemical forces**. Their origin lies in the overlap of electron wave function of the outer shells, which leads to a formation of covalent bonds between tip and force. Due to the movement of the tip, these bonds are only temporarily. An approximation to this interaction can be made with a potential established by Philip M. Morse [79]:

$$E_{\mathrm{chem}}(z) = -E_{\mathrm{bond}}(2e^{-a(z-z_0)} - e^{-2a(z-z_0)}) \tag{1.15}$$

Here, E_{bond} is the bonding energy, a is the decay (interaction) length and z_0 the distance in equilibrium. From this, the corresponding chemical force can be derived as [80]:

$$F_{\mathrm{chem}}(z) = -\frac{\partial E_{\mathrm{chem}}(z)}{\partial z} = -2a \cdot E_{\mathrm{bond}}(e^{-a(z-z_0)} - e^{-2a(z-z_0)}) \tag{1.16}$$

If the distance between tip and sample becomes smaller than necessary for a chemical bond, repulsive forces dominate the interaction between tip and sample. They can be explained by two different origins:

On the one hand, the inner, filled core shells interact with each other. Due to the same electrostatic charge this leads to a **repulsion of core electrons**. The influence of the nuclei can be neglected, since the they are well shielded by the inner electron shells [65].

On the other hand, the overlap of the inner core shells results also in a quantum-mechanical repulsion, the **Pauli repulsion**. This goes back to the exclusion principle by Wolfgang Pauli, after which two or more electrons in a quantum system can not occupy the same quantum state [81].

To approximate both repulsive interaction forces, a quantum mechanical treatment is necessary, which requires the solution of the Schrödinger equation for a multi-electron system. Since this is in the most cases quite complicated, it became common to use models with qualitative approximations. One of the most common models, used for the interaction of two neutral atoms, is the *Lennard-Jones potential* [64], named after John Edward Lennard-Jones:

$$E_{\mathrm{LJ}}(z) = -E_{\mathrm{bond}} \left[\left(\frac{z_0}{z} \right)^{12} - 2 \left(\frac{z_0}{z} \right)^{6} \right]. \tag{1.17}$$

As in equation 1.15, E_{bond} describes here the bonding energy and z_0 the equilibrium distance ($E_{\mathrm{LJ}}(z_0) = 0$). The Lennard-Jones potential clearly distinguishes between attractive long-range and repulsive short-range forces: The attractive ones (mainly van der Waals) are assumed to be proportional to $-1/z^6$ and the repulsive ones to $1/z^{12}$. From this potential the following total force for the tip-sample interaction $F_{\mathrm{ts}}(z)$ can be derived:

$$F_{\mathrm{ts}}(z) = -\frac{\partial E_{\mathrm{LJ}}(z)}{\partial z} = \frac{12 E_{\mathrm{bond}}}{z_0} \left[\left(\frac{z_0}{z} \right)^{13} - \left(\frac{z_0}{z} \right)^{7} \right]. \tag{1.18}$$

The graphical course of the total force $F_{\mathrm{ts}}(z)$ is displayed together with the repulsive and the attractive forces in figure 1.6.

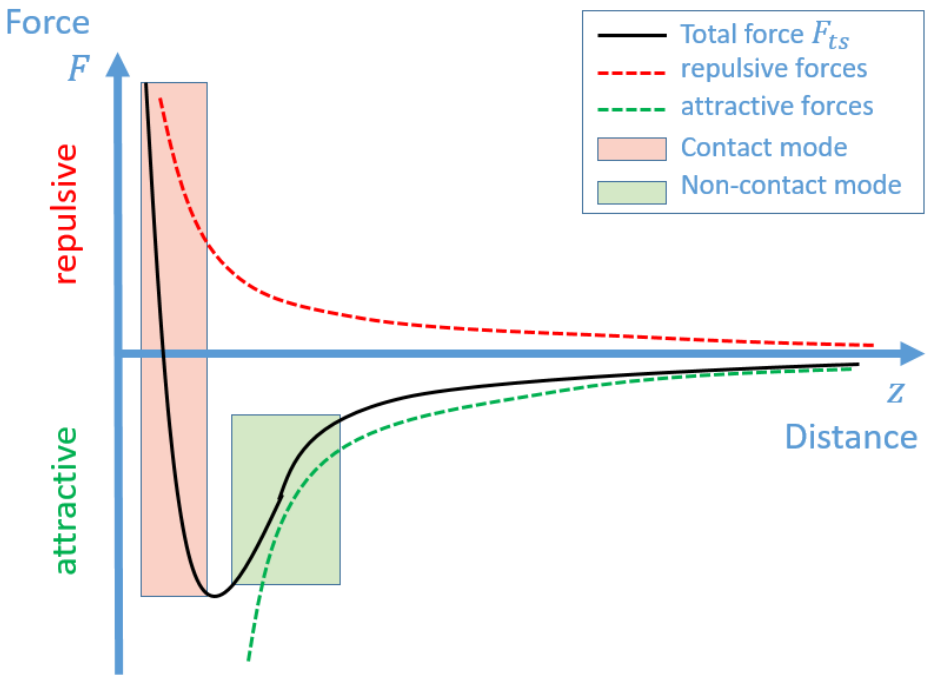

Figure 1.6: *Comparison of repulsive, attractive and total force between tip and sample. The distance range, where contact and non-contact mode can be applied, is marked.*

1.2.2 Operating the AFM

The operation modes of AFM are very numerous and include several different methods of measurement. A first differentiation can be done based on two factors: The behavior of the cantilever, which can be *static* or *dynamic*, and the type of probing the interaction, which can be in *contact* (repulsive), in *non-contact* (attractive) or in *intermittent contact* (tapping of the cantilever). The characteristics of each cantilever type and further distinctions are described in the following.

In **static** AFM, a static cantilever is scanned in the x-y-plane over the surface and the forces between tip and sample cause a deflection Δz of the cantilever. Starting from an equilibrium position, the effective deflection is according to Hooke's law proportional to the local force between tip and sample. Hence, the cantilever has to be rather soft in comparison to the bulk atoms of tip and sample [66]. It can be realized in the *constant force mode* [60], where a feedback loop enables to continue with a certain setpoint force, or in the *constant height mode*, where no feedback loop is needed and the cantilever deflection changes regarding to surface morphology. This is in analogy to the two operation modes in STM, displayed in figure 1.4. Static AFM is very often used in the repulsive force regime and therefore mostly connected to the contact mode. However, it is also possible to perform AFM with a static cantilever in the non-contact regime [65].

The **dynamic** AFM uses a cantilever with a resonance frequency f_0, excited by a fixed amplitude A_{drive} at a fixed driving frequency f_{drive}, that is close to f_0. If the distance between tip and sample is decreased, the interaction forces cause a shift Δf of the resonance frequency, that leads also to a shift of the oscillation amplitude A and a phase Φ between excitation and oscillation.
In the **amplitude modulation mode (AM)**, the driving amplitude is used as setpoint and the oscillation amplitude is taken as reference for a feedback loop to guarantee a constant tip-sample height [82]. In comparison to static AFM, this technique is more precise to measure attractive forces. However, the amplitude feedback depends linearly on the Q factor, which describes as damping parameter the energy loss of an oscillator (high Q indicates less energy loss and less damping) [66]. Hence, a well oscillating cantilever worsens the feedback time in the AM-mode.
With the **frequency modulation mode (FM)**, Thomas R. Albrecht *et al.* worked this out by using the shift of the resonance frequency Δf for the feedback and adjusting the driving frequency f_{drive} with a phase-locked-loop (PLL) detector [69]. Here, the feedback is no longer dependent from the Q factor [66]. To find a connection between Δf and the total force $F_{\text{ts}}(z)$ numerical and analytical calculations must be done. An approximation, where the force gradient $k_{\text{ts}} = -\partial F_{\text{ts}}(z)/\partial z$ is assumed to be constant results in [66]:

$$\Delta f = \frac{f_0}{2k_{\text{c}}} k_{\text{ts}} = -\frac{f_0}{2k_{\text{c}}} \frac{\partial F_{\text{ts}}(z)}{\partial z} \tag{1.19}$$

The k_{c} describes here the stiffness of the cantilever. According to equation 1.19, an attractive force with $\partial F_{\text{ts}}(z)/\partial z > 0$ leads to a negative frequency shift ($\Delta f < 0$) and a repulsive force to a positive one ($\Delta f > 0$).

Due to the dynamics of the cantilever, the AM- and the FM-mode are normally connected to the non-contact range. An adaption of the AM mode to closer distances and the measurement of repulsive forces succeeded with the establishment of the **tapping mode (TM)**, where the amplitude was increased up to 20-100 nm [83]. At the lowest part of the oscillation, the tip is in contact with the surface, but in comparison to the static mode, the lateral influence of the forces is greatly reduced. Hence, this operating mode is denoted to be in intermittent contact.

In principle, the static mode is used in the contact range, where repulsive forces are dominant, the dynamic modes in the non-contact range, where attractive forces are dominant and the tapping mode with its intermittent contact in both ranges (see also figure 1.6). Further limits and expansions to this general principle and to the efficiency of these operation modes are given e.g. by the usage of ultra high vacuum (UHV), low temperature (LT) and quartz tuning fork sensors (QTF). Their influence will be discussed in sections 2.1 and 2.2.

1.2.3 Kelvin probe force microscopy (KPFM)

The nc-AFM method can be expanded by adding the measurement of the work function. Then it is called *Kelvin Probe Force Microscopy* (KPFM), which refers to the probe, Lord Kelvin used to show the potential difference between different metals (see figure 1.7 a) [84]. It has been introduced in 1991 by Martin Nonnenmacher *et al.* [72] with measurements of the contact potential difference (CPD).

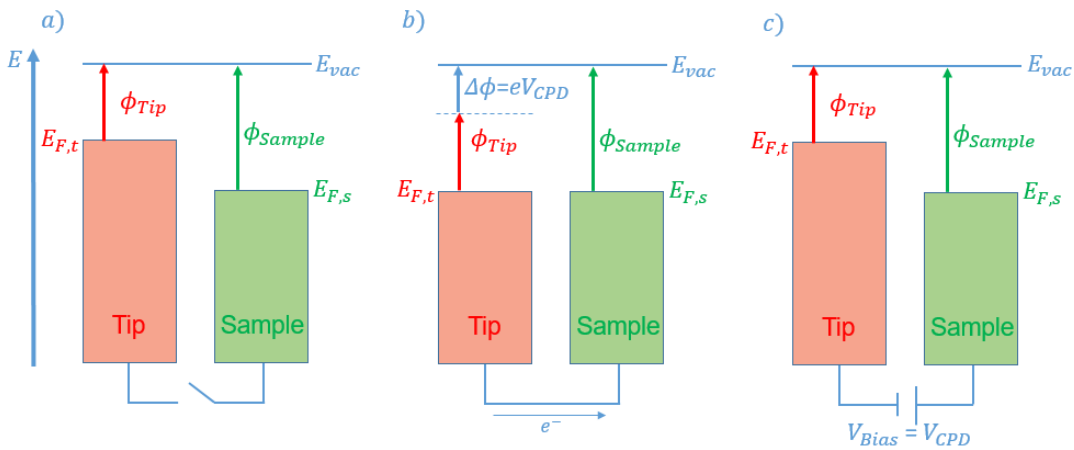

Figure 1.7: Contact potential difference (CPD). ***a,*** *Tip and sample (different materials) are in close contact, but not electrically connected* ***b,*** *Their Fermi levels equalize by connecting both electrically, a CPD ($\Delta\Phi = V_{CPD}$) arises and electrons flow from the filled states to unfilled states* ***c,*** *The CPD can be compensated by applying a bias voltage U_{bias}, so that no current occurs anymore ($U_{bias} = V_{CPD}$).*

If the different metals (for SPM: tip and sample) get electrically connected, the CPD causes a current between tip and sample until their Fermi levels are equal (see figure

1.7 b). This current can be compensated to zero by applying a voltage U_{bias}, that thus indicates the contact potential difference V_{CPD} (see figure 1.7 c) [85]:

$$V_{CPD} = U_{\text{bias}} = \frac{\Phi_{\text{Sample}} - \Phi_{\text{Tip}}}{e} \Delta\Phi \tag{1.20}$$

The e is here the elementary charge. If the determination of the CPD is done with dynamic AFM, an additional AC voltage with the frequency f_{AC} is applied to between tip and sample, which modulates the force between tip and sample as well as the cantilever deflection. Concurrent with dynamic AFM, the amplitude of the cantilever (amplitude modulation, AM) [86] or the variation in the frequency shift Δf (frequency modulation, FM) can be used as setpoint to compensate the CPD. While in AM-mode the measured amplitude of the cantilever is proportional to the electrostatic forces, it is in FM-mode only proportional to the gradient of the force, which leads to a better contrast in FM-mode [87]. According to equations 1.19 and 1.14, the correlation between frequency shift Δf and the compensation difference $\Delta V = U_{\text{bias}} - V_{\text{CPD}}$ can be approximated by:

$$\Delta f = -\frac{f_0}{2k_{\text{c}}} \frac{\partial F_{\text{ts}}(z)}{\partial z} = -\frac{f_0}{2k_{\text{c}}} \cdot \frac{1}{2} \cdot \frac{\partial^2 C(z)}{\partial z^2} (\Delta V)^2 \tag{1.21}$$

If this method is used as spectroscopic technique to investigate local contact potential differences (LCPD), the frequency shift curve is measured at constant height for different voltages. The resulting $\Delta f(V_{\text{bias}})$ curve can be fitted in accordance to the quadratic dependence from equation 1.21 with a parabola. The maximum of the parabola is equal to the LCPD-value and the frequency of the uninfluenced interaction force [85], as imaged in figure 1.8.

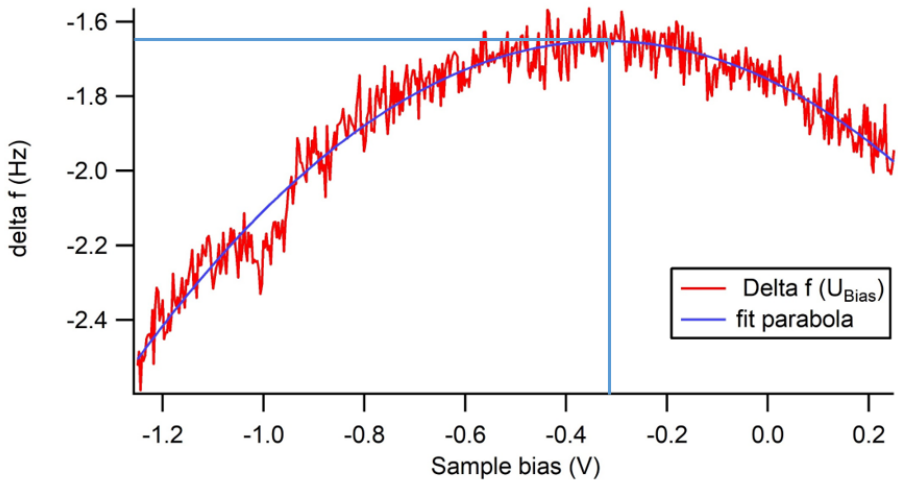

Figure 1.8: *Example of a $\Delta f(U_{bias})$-curve. The maximum at $V_{LCPD} = -0.32$ V and at $\Delta f = -1.65$ Hz refers to the LCPD and to the frequency of the uninfluenced interaction force. The deviation from the parabola at ≈ -1.0 V refers to a local charge state.*

The spectroscopic mode is known under the name *LCPD mapping* or *Kelvin probe force spectroscopy* (KPFS) and provides even submolecular resolution. Hence, it can be used to investigate charge states of atoms [77] and molecules [88, 89], or even to induce charges on molecular layers by the KPFS-measurement [90]. Further descriptions on the detection of charges with SPM methods are given in section 3.2.3.

1.3 Summary

This chapter describes the principles, the history of development and the implementation of the measurement methods, which were used to achieve the results presented in the following chapters. This is Scanning Probe Microscopy (SPM), which can be used in either Scanning Tunneling Microscopy (STM) or Atomic Force Microscopy (AFM). Both methods combine the ability to scan the surface morphology with atomic resolution. Regarding to the focus of this work, two special applications have been discussed: on the one hand, Scanning Tunneling Spectroscopy (STS), which enables to measure the Local Density of States (LDOS) of a surface, and on the other hand, Kelvin Probe Force Microscopy (KPFM), which enables to measure the local contact potential difference (LCPD). From the description of theses methods, it becomes clear that the use of both methods is an important tool to determine and control the charge state within a molecule.

2 Setup & Implemetation

In this chapter, the setup of the measurement system, a low temperature Scanning probe microscope (LT-SPM) in ultra-high vacuum (UHV), is described in details. In the first section, the UHV system itself and the connected evaporators are discussed (see section 2.1). Then, the cryostat and the microscope inside are described in more detail, which includes the tuning fork sensor, the preparation of the tip and the software used to control the measurement (see section 2.2). Finally, the procedures for preparing the Pb samples are characterized (see section 2.3) and the adsorbed atoms and molecules are described in details (see section 2.4).

2.1 Setup of the Ultra High Vacuum System

All samples have been prepared and investigated under UHV conditions. The term "UHV" refers to a pressure below $1 \cdot 10^{-9}$ mbar (= 100 nPa). The employment of UHV is necessary to avoid contaminations from the atmosphere. Each sample, that has been exposed to air, was cleaned by several procedures to ensure the absence of contaminants from air (see section 2.3). But even if samples are kept in vacuum, a contamination with residual gases can not be excluded. The most common residual gases are H_2 ($m_{H_2} = 2$ u), CH_4 ($m_{CH_4} = 16$ u), CO ($m_{CO} = 28$ u) and CO_2 ($m_{CO_2} = 44$ u), which can be checked by using a mass spectrometer [91]. For this reason, the facility to clean a sample and to sublimate molecular layers *in situ* is crucial for the correct implementation of the measurement. In the utilized UHV-system, the samples are prepared in the preparation chamber and then transferred into the analysis chamber, where the cryostat with the microscope is located. Both chambers are separated by a valve, to reduce contaminations in the analysis chamber. The total UHV system is shown in figure 2.1. The devices of the preparation chamber are presented in subsection 2.1.1 and the process of sublimating molecules and atoms is described in subsection 2.1.2. The cryostat and the microscope inside are described separately (see section 2.2).

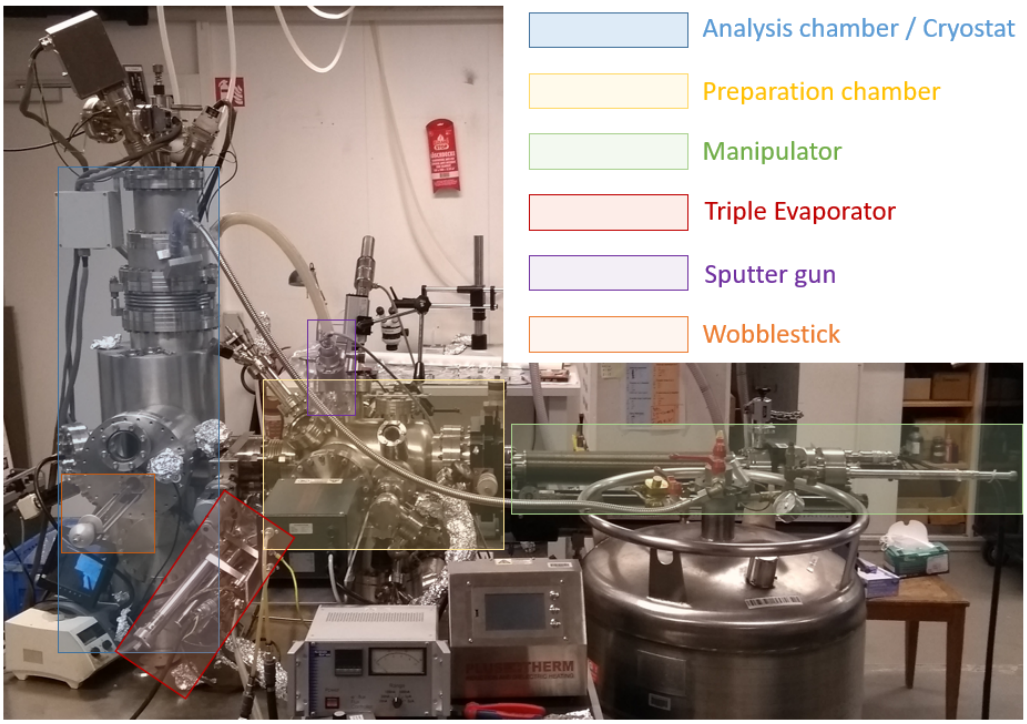

Figure 2.1: *Overview on the UHV measurement system. The two main parts, the analysis chamber with cryostat (blue), where the microscope is located, and the preparation chamber (yellow), where cleaning and evaporation is applied to the samples can be separated by a valve.*

2.1.1 Preparation Chamber

On the one hand, the preparation chamber fulfills the purpose of preparing samples by cleaning them or sublimating atoms or molecules on them. On the other hand, it is located between the analysis chamber and the load lock, where the samples can be introduced into the system. Hence, the base pressure is around one order of magnitude lower than in the analysis chamber at the range of 10^{-10} mbar. The vacuum is achieved by an ion getter pump (IGP) and a turbo molecular pump (TMP). In case that high amounts of residual gases from former sublimations worsen the pressure, an additional Titanium sublimation pump (TSP) can be switched on to improve again. The instantaneous pressure in the chamber can be read out via ionization gauges. Each sample can be transferred within the chamber and to other chambers by means of a rotatable manipulator arm that can be moved in all dimensions.

Beneath the sample on the manipulator, an e-beam heating system enables to outgas the sample by annealing to a maximum temperature of about 1000 °C. The respective temperature can be determined by a thermocouple on the sample holder or a pyrometer. For the cleaning of samples with argon sputtering (see also section 2.3), a sputter gun is connected to the preparation chamber. The needed Ar atmosphere with a pressure of $5 \cdot 10^{-6}$ mbar can be regulated by means of an UHV leak valve.

2.1.2 Sublimation of atoms and molecules

Additionally, the preparation chamber is also equipped with a triple evaporator to sublimate molecules and adsorb them on the sample. The evaporator exhibits three crucibles, which can be filled with different molecules and heated individually. The crucibles are heated up by electron bombardment and a water cooling is mandatory to guarantee a precise control of the flux. This kind of evaporators is often known as *Knudsen cell*, since Martin Knudsen described the working principle of this method in 1909 to measure the vapor pressure of gases within tubes and at their orifices [92, 93]. The deposition rate on the sample can be checked by a quartz micro balance (QMB). It is important to ensure a stable rate before the evaporation on the sample is started.

In addition to the evaporation in the preparation chamber, the deposition of molecules can also be done in the analysis chamber in front of the microscope. This has the advantage that the sample can remain at LT. This is crucial for the deposition on thin insulating layers (as NaCl or KBr), since the molecule would diffuse to the metal at higher temperatures. It can be obtained by small silicon wafers, sticked on a mobile evaporator (see figure 2.2 a). The evaporator is first placed in the same way as the sample in front of the Knudsen cell to get adsorbed with molecules. However, the deposition rate has to be higher as for the direct adsorption. After that, it is transferred into the analysis chamber, positioned in front of the microscope and the silicon is heated by a direct current up to 500°C.

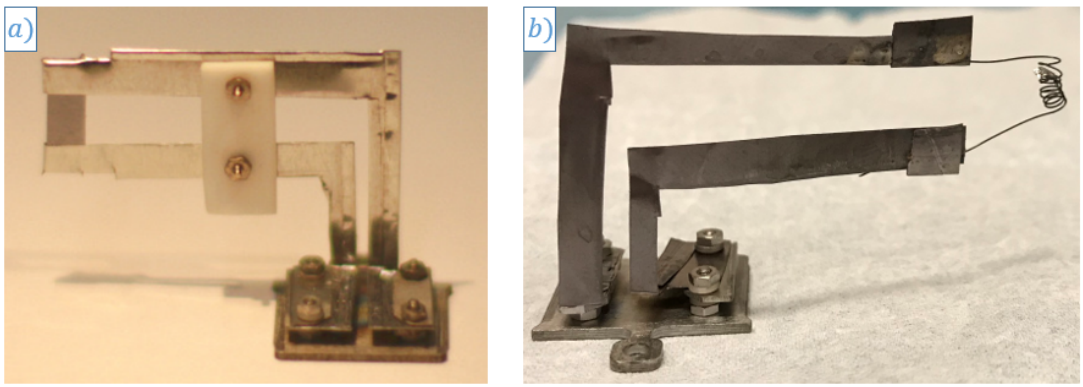

Figure 2.2: *Image of the mobile evaporators:* ***a,*** *Mobile evaporator with silicon wafer to transmit molecules.* ***b,*** *Mobile evaporator with a piece of Fe inside a coiled tungsten filament to evaporate single Fe atoms.*

For the deposition of single atoms, an alternative mobile evaporator can be used: Here, instead of a silicon wafer, a piece of the material, from which atoms shall be adsorbed, is put within a coiled tungsten filament (see figure 2.2 b). When the filament is heated up to temperatures of $\approx$ 1300°C, the Fe sublimates and scatters - similarly to the molecules from the silicon - also into the microscope.

2.2 Cryostat and Low-temperature Scanning probe microscope

The most crucial part among the experimental devices is the scanning probe microscope itself, which is located within a cryostat to allow measurements at low temperatures. The use of low temperature (LT) for SPM, which means < 5 K, has certain advantages compared to room temperature (RT) measurements: Most important is the reduction of thermal diffusion. Additionally, vibrational and rotational movements of single atoms can be reduced enormously, which makes STM images clearer and sharper [94]. The cooling also increases the stability of the whole system, which is crucial for AFM, since thermally excited vibrations of the cantilever influence the sensitivity of the measurement [95]. Furthermore, the contamination rate in the cryostat is reduced dramatically for time intervals of several weeks, which is the basis for prolonged investigations as e.g. the manipulation of single atoms [39].

First experiments with STM in the LT-range have been applied to investigate the electronic structures of superconductors [96]. This refers back to first electron tunneling experiments at single positions [97, 98], for which the new 2D investigation with LT-SPM methods denotes a crucial step in development. However, in the first setups the microscope had to be fully immersed with liquid helium. The first LT-SPM in an UHV-system has been developed in 1989 by Don M. Eigler and Erhard K. Schweizer [39]. It provided a high thermal stability, but exhibited comparably long turn-around durations. A first LT-SPM in UHV with a fully flexible, controllable tip has been achieved in 1992 by IBM Zurich Lab [99]. This approach constitutes the basis, on which Omicron NanoTechnology GmbH (now: ScientaOmicron) developed a standard LT-SPM [100], which is also used for this work.

The cryostat of the Omicron LT-SPM consists of an outer chamber, cooled down with liquid nitrogen ($T_{\mathrm{N}_2} = 77.3$ K), and an inner chamber, cooled down with liquid helium ($T_{\mathrm{He}} = 4.2$ K). After a refill with N_2 and He, the system can hold a constant coldness of ≈ 4.7 K for ≈ 17.5 h. However, measurements can also be done at 77 K, at RT, or with the help of a heater at a desired temperature. Inside the cryostat, the microscope is located on a piezoelectric scanner (see subsection 1.1.2) and exhibits a tuning-fork tip, which is described more detailed in subsection 2.2.1. Separate subsections explain also the preparation routine of the tip (subsection 2.2.2), its modification (subsection 2.2.3) and the used software to control the tip movement and the measurements (subsection 2.2.4). The whole microscope can be decoupled from external vibrations with a spring and in addition to that it is damped by an eddy current damping system.

Two shutters separate the cryostat from the surrounding analysis chamber, from where a sample can be inserted by a wobblestick. A carousel in the analysis chamber allows to store 18 samples or spare tips. The base pressure of $\approx 10^{-11}$ mbar is achieved by an IGP, a TMP and if required by a TSP. The instantaneous pressure is read out via ionization gauges.

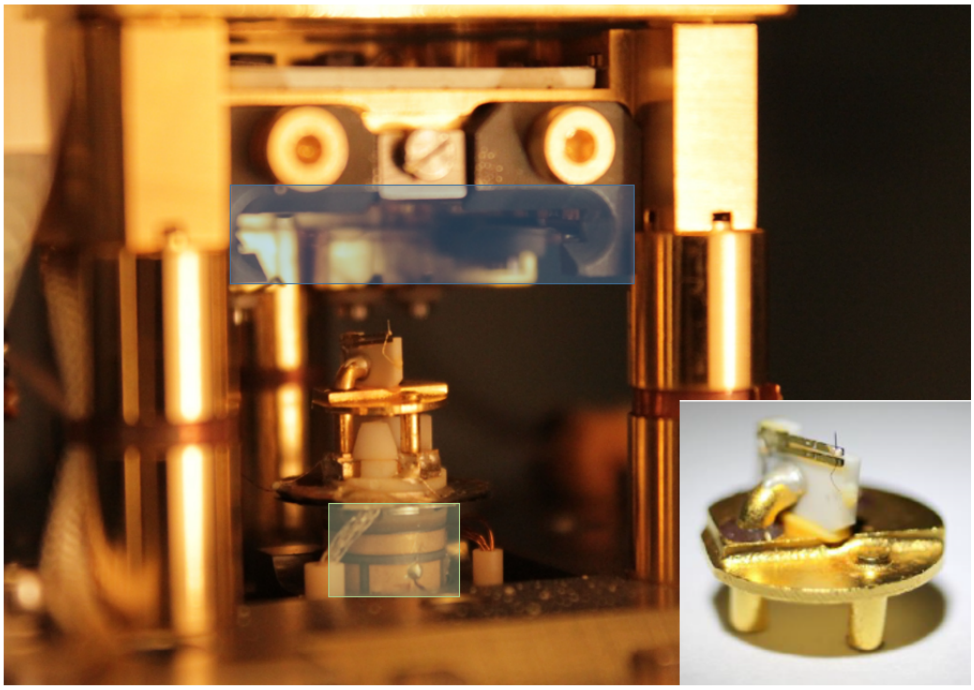

Figure 2.3: *Side view of the UHV LT-SPM head: Above the scanner with the qPlus sensor on top of it is the drawer for the sample located (blue). The scanner (green), moved by three piezo tubes can be approached. Inlet: Enlargement of the qPlus sensor.*

2.2.1 Tuning-fork sensor

Due to the advantages of FM-AFM (see subsection 1.2.2), the microscope uses the qPlus design, a quartz tuning fork (QTF) sensor to facilitate the stability of the frequency of the tip. The idea to use a QTF for the AFM tip [101] has been developed by Franz J. Giessibl in 1996 [102], who was inspired by quartz watches with high Q factors. The success of this design in AFM and the advantages towards conventional cantilevers have been proven by demonstrating the achievement of atomic resolution on Si(111)-(7×7) [103]. However outside of AFM, first experiments with QTF sensors have already been carried out in 1989 by the group of Klaus Dransfeld in near field acoustic microscopy [104].

The qPlus sensor uses a tuning fork, from which one prong is immobilized, since it is glued onto a mount on an actuator. This is connected with an I-V converter to detect the deflection. The other prong is able to oscillate and exhibits the tip of the microscope at its end, which is connected separately with a wire to apply a tunneling current. Figure 2.3 gives an overview on the head of the microscope and the qPlus sensor on top of the scanner.

The tip used for this work is made of tungsten (see subsection 2.2.2). The stiffness of the qPlus sensor is about $k = 1800$ N/m and its resonance frequency at about 25 kHz. These mechanical characteristics can be varied with home-built qPlus senors [105].

2.2.2 Preparation of the tip

In SPM measurements, the preparation of the tip is a key success factor for the quality of the posterior image. In an optimum scenario it terminates in a single atom, since the topmost atom has the major influence on the tip-surface interaction. A variety of different methods can be used to fulfill this goal [106]. In this work, the preparation can be divided into two fundamental routines: The anticipated, rough sharpening of the tip by means of a focused ion beam (FIB) and the improvement of the current tip geometry carried out immediately before the measurement by dipping the tip in a controlled way into a sample surface. As tip material tungsten is chosen, which is due to its relatively high hardness a standard material for SPM measurements in UHV [49].

The first rough sharpening step assumes prefabricated tips, attached to the qPlus sensor. These tips are produced by chemical etching, a standard procedure to get preferably sharp tips.

As figure 2.4 a) shows, the prefabricated tips still might exhibit curvatures or blunt terminates, which demand an additional preparation. In 1987, D. K. Biegelsen *et al.* could show that ion milling with a FIB is very suitable for the preparation of tungsten tips: Not only the tip radius can be reduced dramatically, but also contaminations of oxides (WO_x) can be removed and an oxide-free tip is observable for more then 24 h in air [107]. Figure 2.4 b) shows the shape of the tip after ion milling.

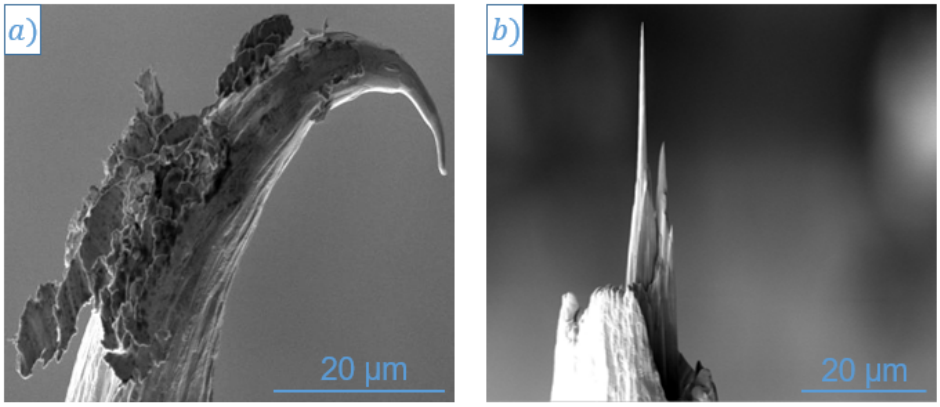

Figure 2.4: *Tip terminus of a qPlus sensor imaged by scanning electron microscopy (SEM): a) Without preparation by FIB the tip exhibits a curvature. b) After preparation with FIB the curved part has been removed and the sharpness improved.*

After inserting the tip into the microscope, a bad local geometry of the tip apex can still reduce the attainable resolution. A typical problem is a so-called double or even multiple tip, which means that two or various apexes influence the tip-sample interaction and cause in the image artificial "ghost" copies of sample structures. This problem can be approached in a rough way by employing pulses with voltages of ± (2-8) V or in a more accurate way by making a controlled contact with $I(z)$-spectroscopy. The latter consists of a exponential approach behavior and a sudden break of the contact.

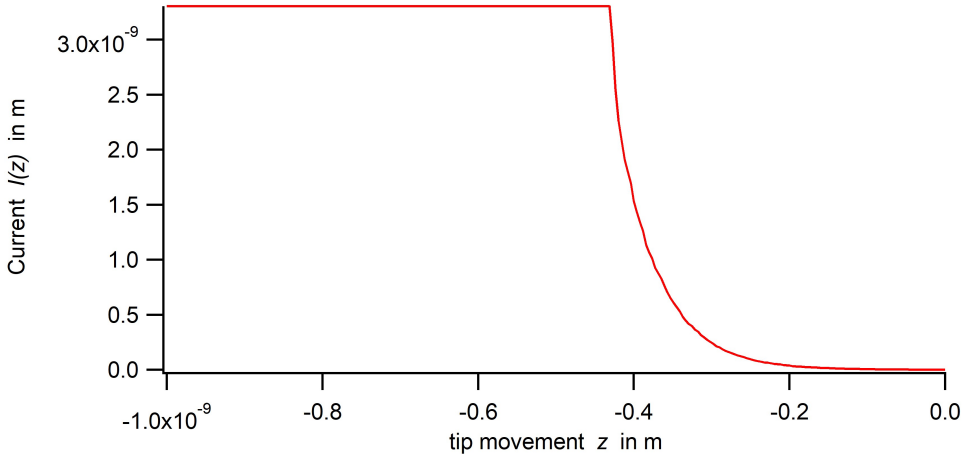

Figure 2.5: *Standard $I(z)$-curve for a controlled tip dip of 1 nm into the Pb surface. The course of the curve shows an exponential $I(z)$-dependence without deviations, which refers to the absence of deposition or adsorption at the tip terminus.*

Deviations or bumps in the curve indicate the deposition or adsorption of surface atoms and refer to a repetitive cleaning step until the curve shows no derivation. In fig. 2.5 a standard example for this case is illustrated. It should be noted that by the use of pulses and $I(z)$-spectroscopy, the tip picks up surface atoms from the respective sample surface. In case of superconducting Pb samples, the tip will become also superconductive. Hence, the tip preparation should only be carried out at clean, stepless terraces on the sample. In addition to these active preparation methods, the selection of an appropriate tip-sample distance also affects the tip geometry and the scanning stability very strongly.

2.2.3 Modification of the tip

In addition to the preparation of the tip, also its modification with a single molecule (such as CO) adsorbed at its apex leads to a chemical contrast [108]. This means that the visible contrast by SPM differs in dependence of the chemical state of the sample. Among different molecules used for the modification, the functionalization with single CO molecules received special attention after Leo Gross *et al.* succeeded in resolving a pentacene molecule on Cu(111) atomically with NC-AFM measurements [71]. The origin of the high atomic contrast can be explained by the Pauli repulsion, which is especially dominant at high electron densities. Since the CO molecule is chemically inert, it can be approached very close to the surface without forming a chemical bond (if it would form a bond to the surface, it would break the bond to the tip). Hence, it can measure the short-range Pauli repulsion better than other functionalizations, which are able to form a bond to the sample and keep the one to the tip [109].

To pick up a CO molecule, CO has to be first adsorbed on the sample. This can be done at LT inside the microscope by floating the whole analysis chamber at a

pressure of $p = 5.0 \times 10^{-8}$ mbar with CO. Depending on the chemical state of tip and sample, it appears in STM as protrusion or depression. The CO molecule can be picked up by positioning the tip on top of it, applying a $I(z)$-spectroscopy until a current jump in the spectroscopy occurs. The CO molecule predominantly forms a bond with the carbon atom, both to the sample and to the tip and rotates therefore by 180° with the picking procedure [110].

2.2.4 Measurement control and evaluation software

The measurements are controlled and carried out by using RC5 electronics operated with Nanonis V5 software. For their implementation a power supply, a real-time controller, an oscillation controller, a high-voltage amplifier, a signal converter and an Omicron interface converter by Nanonis is used. Additionally, a home-made piezo motor controller enables the control of the scanner in x-, y- and z-direction.

The evaluations of the SPM- and AFM-images are predominantly executed with the help of *Gwyddion*, an open-source platform for various data processing and image analysis methods [111].

2.3 Preparation of clean Pb samples

The experimental work presented in this thesis is entirely executed on top of Pb(111) or Pb(110) single crystals. The crystals are purchased by Mateck GmbH, which have already polished them electrochemically and guarantee a purity of 99.99 %. Pb crystallizes in a face-centered cubic (fcc) crystal structure with a constant lattice parameter of $a = 4.950$ Å [112]. The (111) plane is the closest packed structure among the low-index surfaces and its rhombic unit cell has a length of $a/\sqrt{2} = 3.500$ Å with an angle of 60°. In contrast, the (110) plane is the less compact one and shows in the top most layer a rectangular unit cell with a distance of $a/\sqrt{2} = 3.500$ Å within the atomic rows and $a = 4.950$ Å between them. In figure 2.6 both surface structures are illustrated.

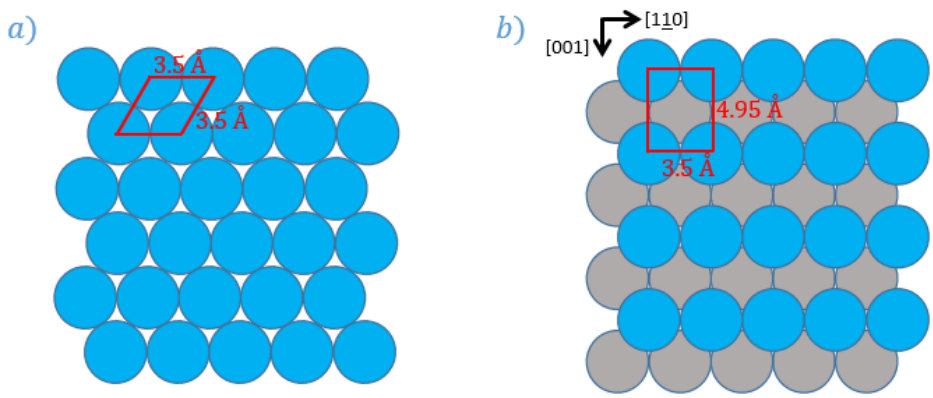

Figure 2.6: *Surface structure for* ***(a)*** *Pb(111) and* ***(b)*** *Pb(110) crystals. The unit cell of the surface structure is marked in red.*

The cleaning of the Pb crystals consists of 3-4 cycles of 10 minutes sputtering with Ar^+-ions and 10 minutes of annealing at $T \approx 150$ °C. If samples are introduced into the system from outside more cleaning cycles are necessary. The purity of the samples can be assessed on the basis of STM measurements (see figure 2.7).

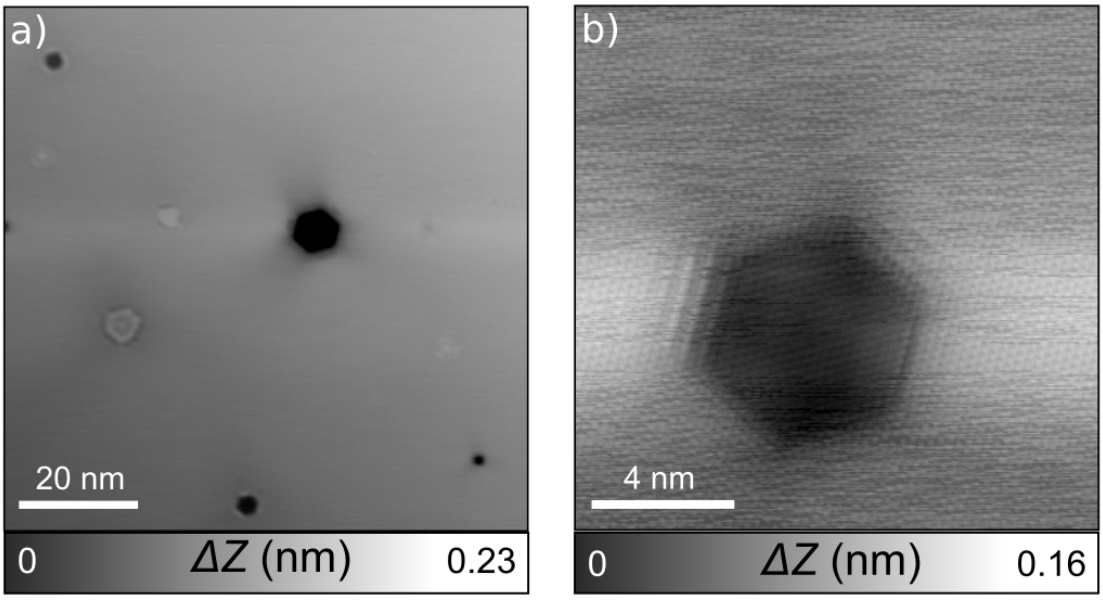

Figure 2.7: Pb(111) sample after cleaning procedure. ***(a)*** *The overview STM image of Pb(111) (I_t = 1 pA, V_b = -50 mV) shows various hexagonal features in the size of 1-10 nm.* ***(b)*** *A more detailed view (I_t = 1 pA, V_b = -10 mV) exhibits an apparent height of ≈ 1 Å and also faint symmetric frames with larger diameters around the features.*

The STM-images after the cleaning procedure show in the most parts of the surface large, clean Pb terraces with an average size of ≈ 200 nm^2. However, as figure 2.7 illustrates, also some hexagonal features in the size of 1-10 nm with an apparent height of ≈ ± 1 Å can be found. Their appearance with positive or negative corrugation can be changed by varying the bias voltage. All these characteristics are in accordance with an electronic interference phenomenon, known for Al(111) and Pb(111) surfaces: The occurrence of the hexagonal features is interpreted as interference of bulk states, which form a quantum well between the top most and a subsurface layer [113]. In turn, the origin for the reflecting behavior of the bulk states is explained by gas bubbles of Ar, which originate from the sputtering process [114]. The hexagonal shape of the interferences harks back to the Wulff construction of fcc (111) surfaces, a method to calculate the equilibrium shape of a fixed volume within a separate phase.

The scaling of the microscope can be checked by using the clean Pb(111) surface as a reference. It has turned out that the measured unit cell is in accordance with the model shown in Figure 2.6.

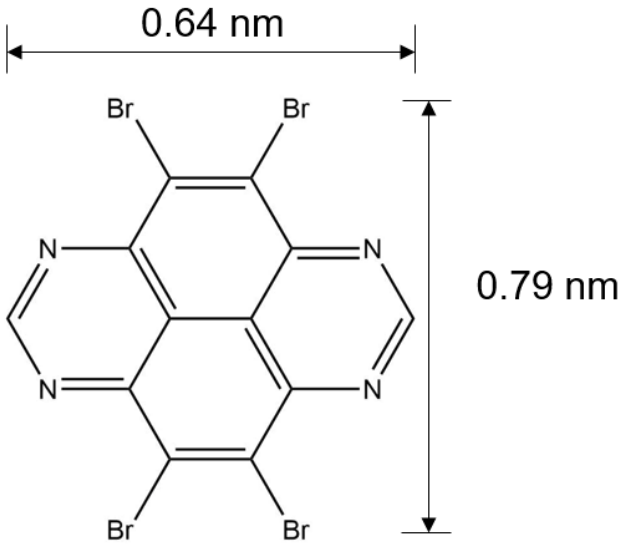

Figure 2.8: *Structure formula with approximate size of TBPP ($C_{12}H_2Br_4N_4$).*

2.4 Adsorption of single atoms and molecules

In this section the adsorbates used in this work, Fe-atoms (see section 2.4.1) and TBPP molecules (see section 2.4.2), are described individually. This includes their evaporation parameters and - if available - a summary of the published literature on it.

2.4.1 Adsorption of single Fe-atoms

The adsorption of single Fe atoms is performed at LT with a mobile evaporator in front of the microscope, where a piece of Fe is inside a coiled W filament, as described in subsection 2.1.2. The duration of the adsorption was 15 minutes. The Pb sample was kept in the microscope and investigated afterwards by SPM methods.

This preparation has also been performed in other studies, however, the sample was kept there ar room temperature [17, 18] or heated up to 400 K [19]. The results of theis adsorption are presented in chapter 4.

2.4.2 Adsorption of TBPP molecular layers

The 4,5,9,10-**t**etra**b**romo**p**yrimido[4,5,6-gh]**p**erimidine molecule ($C_{12}H_2Br_4N_4$, short: TBPP) is based on a two pyridazine rings which are connected by two benzene rings with each bond to two bromine substituents (see structure in figure 2.8). The molecule is a 2D organic monomer with an aromatic scaffold and bromine substituents. It has been synthesized by the group of Shi-Xia Liu and Silvio Decurtins at the University of Bern. So far, it has not been investigated in more detail in the literature.

At room temperature the powder of the molecule exhibits a yellow color. For the evaporation it was heated up in the triple evaporator (see figure 2.1) to 170-200°C and a rate of $\approx$ 2.4 Å/min was measured with the QMB. The Pb sample was kept at room temperature and immediately after the adsorption, it was given into the LT-microscope.

2.5 Summary

This chapter describes the requirements for the implementation of the experiments described in this thesis. It underlines the importance of UHV conditions to obtain atomic resolution and to fulfill manipulations in the atomic regime. The description of the UHV system is subdivided into various parts and contains also a specification of single devices connected to the system and used for the preparation of samples. Additionally, the microscope itself and its application in the measurement is characterized. Hereby, a special attention is given to the tip and its preparation.

In the following, the preparation of the Pb samples is described, which includes an explanation on the surface structure and the characteristics of a clean surface in STM. Finally, the evaporated molecules are described in a fundamental way, which is essential for the interpretation of the following chapters.

3

Basics of Majorana bound states & molecular quantum dots

THIS chapter introduces the basic physical principles that are necessary to initiate experimental investigations and summarizes previous results with reference to the literature published so far.

Since all the work of this thesis has been performed on superconducting lead (Pb), this chapter begins with a general description of superconductivity, which in the further course also contains the influence of magnetic impurities, as well as the realization and experimental observation of Majorana bound states (MBS) (section 3.1). Subsequently, the focus is set on charge states in molecular quantum dots, which includes the implementation of charges between a superconducting SPM tip and single molecules, as well as the characterization of charge states with different SPM techniques (section 3.2).

3.1 Introduction to Superconductivity and Majorana bound states (MBS)

Superconductivity is the ability of a material to conduct electricity without resistance at temperatures below a critical temperature T_C. Unlike ordinary metals, whose electrical resistance gradually decreases for lower temperatures, they exhibit a sudden disappearance of the electrical resistance at T_C. The first observation of superconductivity was measured at $T_C = 4.2$ K on mercury in the laboratory of Heike Kamerlingh-Onnes [115]. Simultaneously to the lack of electrical resistance, external magnetic fields are displaced and inside the superconductor no magnetic field intensity can be measured. This is known as "Meissner-Ochsenfeld effect" and was first described by Walther Meissner and Robert Ochsenfeld in 1933 [16]. A distinction is made between superconductors of the type-I and type-II: While the superconductivity and the displacement of external magnetic fields collapse for type-I superconductors also above

a critical external magnetic field strength H_C, type-II superconductors exhibit a first critical field strength H_{C1} from which only the Meissner-Ochsenfeld-Effect suspends and a second critical field strength H_{C2} from which the superconductivity also stops.

The field of application for superconductors is wide and ranges from powerful magnetic fields and lossless power lines up to superconducting quantum interference devices (SQUIDs). The latter are generated with the help of the so-called Josephson effect, measure extremely small changes in a magnetic field and can also be used as a thermometer or bolometer. In addition to that, SQUIDS are due to their Josephson junctions seen as possible basis for implementing qubits, the basic unit of quantum computers with first successes in its experimental realization. [116–119]. Here, one possible usage of SQUIDs is based on the detection and manipulation of so-called Majorana bound state (MBS) [14,120,121], whose formation is explained in the following.

In principle, the Bardeen-Cooper-Schrieffer theory (see subsection 3.1.1) is generally used to describe type-I superconductors, such as Pb (see subsection 3.1.2). With the help of this knowledge, the effect of magnetic impurities on superconductors can be discussed (see subsection 3.1.3), which might ultimately be used in topological superconductors for the experimental realization of Majorana bound states (MBS) (see subsection 3.1.4). Finally, the detection of MBSs with SPM-related methods is described in subsection 3.1.5, which includes a review on the most important experimental achievements published in the literature.

3.1.1 Bardeen-Cooper-Schrieffer theory

In 1957 John Bardeen, Leon Cooper and John Robert Schrieffer published the first comprehensive theory that describes superconductivity on a microscopic level [122, 123]. It is known as *BCS theory* in relation to the developers' last names and its core is the assumption that two electrons combine to form a so-called "Cooper pair" as carrier of the supercurrent. The Cooper pair is created by phonons, the quantized oscillations of the atomic lattice, as an electron moving in it interacts with the positively charged ion cores and changes the lattice oscillation by releasing energy. Since the inert ion cores swing back more slowly than the electron moves, a second electron can absorb this change in energy. Finally, the two electrons overcome the Coulomb repulsion and are connected by the phonon to form a Cooper pair. The maximum distance between the electrons, at which this interaction is attractive, is called the coherence length. In addition, there is also a correlation time, which indicates the life time of a Cooper pair and depends on the duration of the lattice oscillation.

In BCS theory, the formation of a Cooper pair requires that momentum and spin of both electrons, are antiparallel. This in turn leads to the fact that the spin is compensated to zero and the Cooper pair is therefore a boson with an integer spin (spin-singlet pair) in contrast to electrons with half-integer spin. As a consequence, Cooper pairs do not have to comply with the Pauli principle and can occupy the same energy level more than once.

The energy gain of two electrons to form a Cooper pair is also known as energy gap, which indicates a zone of suppressed density of states around the Fermi energy. The size of the gap Δ is predicted by BCS theory for $T = 0$ K with use of the Boltzmann constant k_B and the critical temperature T_C as:

$$\Delta(T = 0) = \pm 1.764 \cdot k_B \cdot T_C \tag{3.1}$$

The totality of the Cooper pairs can thus be described with a single wave function, which is valid as a continuum for the entire solid. Local scattering centers cannot influence this continuum, which explains, why the charge transport occurs without resistance. When the external energy becomes too great, such as the supply of heat above the critical temperature T_C or above the critical magnetic field H_C, the electrons can no longer combine to form Cooper pairs, remain in their fermionic properties and the superconductivity collapses.

It must be pointed out that the BCS theory is based on s-wave superconductors, as they predominantly occur in nature. However, artificially produced materials with a d-wave superconductivity could already be proven [124, 125] and in theory a p-wave superconductivity was postulated shortly after the publication of the BCS theory [126]. A crucial difference here is that two electrons with the same spin combine to form a pair and thus the total spin of the pair is $S = 1$. This in turn results in an odd spatial parity, an odd orbital angular momentum $L = 1$ and a triplet spin state [127]. Despite various publications on possible realizations, the undisputed proof of a p-superconductor is still pending [128]. In this context, the proof is considerably more difficult, since some p-wave states cannot be distinguished thermodynamically from s-wave or d-wave states [127].

3.1.2 Properties of superconducting Pb

When characterizing Pb as a type-I superconductor, the comparatively high critical temperature of $T_C = 7.2$ K is initially noticeable. It is (if high pressure is excluded) the third highest among the elementary superconductors (after Nb and Tc) and the highest among the type-I superconductors. The high critical temperature might be the reason, why Heike Kamerlingh Onnes detected Pb in 1913 as second superconducting material [129].

To explain the origin of the high critical temperature, the concept of multi-band superconductivity can be used, which leads to higher critical temperatures in superconductors made of different elements due to the overlapping of the bands [130, 131]. DFT calculations have shown that Pb exhibits a hybridization of the p-bands with the s- and d-bands, which behaves analogously to the multi-band concept [132]. This two-band nature of Pb was experimentally proven by Michael Ruby *et al.*, who observed a selective tunneling into different bands, strongly depending on the crystal orientation [133].

3.1.3 Magnetic impurities on superconductors

The behavior of superconductors can be influenced by different sorts of impurities: Non-magnetic impurities, such as surface defects, step edges or non-magnetic adsorbates, exert a scattering effect on the potential and break thereby the particle-hole symmetry of the superconductor [134]. This symmetry can be derived from the limitation of the BdG Hamilton function for electrons in superconductors according to Nikolay N. Bogoliubov [135] and Pierre-Gille de Gennes [136], in detail reviewed by Masatoshi Sato and Satoshi Fujimoto [134].

Magnetic impurities, on the other hand, interact due to their magnetic potential with the spin of the Cooper pairs, which leads to the formation of localized bound states within the superconducting gap. These states correspond to quasi-particle excitations and were independently described by L. Yu, H. Shiba and A. I. Rusinov in the end of the 1960s [137–139]. They are termed as Yu-Shiba-Rusinov states (YSR-states), or briefly as Shiba states. It is important to distinguish them from the so-called Andreev bound states, which can also be found within the superconducting gap, but represent a scattering at the boundaries of non-uniform superconductors, analogous to the Andreev reflection [140] of quasiparticles at the boundary between superconductors and non-superconductors.

The YSR states arise from the scattering of incident bulk spins with the spins of magnetic impurities and reduce the pairing energy of Cooper pairs. Due to the particle-hole symmetry of the superconductor, each YSR state can be identified in the DOS by a peak above and a peak below the Fermi level, representing electron and hole [139]. For a scattering phase difference between electron-like and hole-like resonances of $\pi/2$, the interaction between bulk and impurity becomes unstable against quantum phase transitions and the YSR bound gets occupied. Then the ground state of the superconductor changes from a spin $S = 0$ to $S = 1/2$ [141]. This change in the spin can also be achieved by adding/removing an electron in or out of the YSR state by tunneling [142].

Recent experimental studies with Mn or Cr atoms adsorbed on Pb(111) have shown that a single magnetic impurity can induce multiple pairs of YSR resonances (see e.g. figure 3.1) [143–146]. If the exchange coupling among the spins of a single impurity is lower than the coupling of each spin to the impurity itself, multiple pairs of YSR resonances can be observed for each impurity, depending on the adsorption site of the adatom that causes the impurity [147]. This observation makes it interesting to investigate, how neighboring impurities affect each other. It has been shown that the wave functions of YSR bound states, originating from different impurities, overlap and couple [147]. The different bound states of each single atom induce due to the hybridization of neighboring YSR states extended subgap bands.

From this it can be concluded that magnetic adatoms, adsorbed on conventional s-wave superconductors, behave equivalent to a p-wave superconductor due to their particle-hole symmetry and their characteristic of connecting the excitation of electrons and

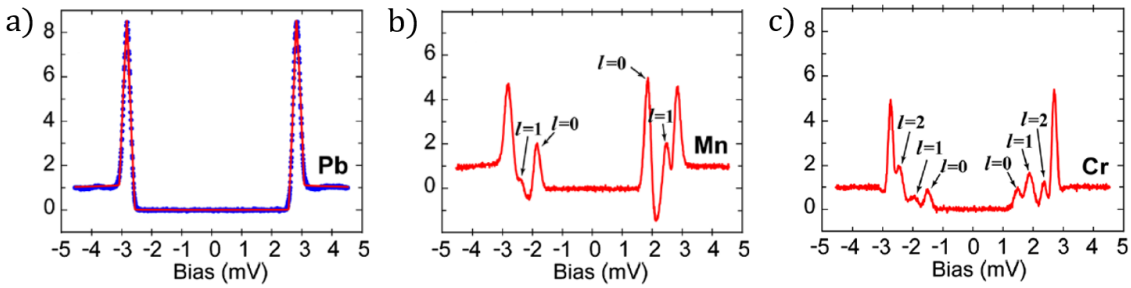

Figure 3.1: *Series of dI/dV spectra at T = 0.4 K, using a superconducting tip, on (**a**) a thin Pb film, showing the superconducting gap* $\Delta = \Delta_{tip} + \Delta_{sample}$*, (**b**) Pb and Mn adatoms, showing the gap and one pair of peaks representing YSR-states and (**c**) Pb film and Mn adatoms, showing the gap and two pairs of peaks representing YSR-states. Source: Reprinted figure with permission from Shuai-Hua Ji et al., High-Resolution Scanning Tunneling Spectroscopy of Magnetic Impurity Induced Bound States in the Superconducting Gap of Pb Thin Films, Phys. Rev. Lett.,* ***100****, 226801 (2008).* *©2008 by the American Physical Society.*

holes with Cooper pairs [14]. Since the structure of the magnetic order can be deformed without closing the bulk energy gap, the topological invariability is kept and the whole system, consisting of magnetic impurities on an s-wave superconductor can be denoted as a "topological superconductor" [120, 134].

3.1.4 MBS in engineered topological superconductors

The topological nature of the superconductor is responsible for the fact that zero-energy Bogoliubov quasiparticles can form at the boundaries, which due to their particle-hole symmetry (a zero-energy state corresponds to the equal-weight superposition of particle and hole) map themselves in their Hermitian conjugate [120, 134, 148]. This in turn has the consequence that a particle is equal to its own antiparticle and thus this state is a solution of the Dirac equation [149] described by Ettore Majorana in 1937 [13]. The so-called Majorana fermion itself is chargeless, spinless, has zero energy and fulfills due to the bounding to a topological defect non-Abelian statistics. This means that exchange operations of particles are not commutative [134].

In 2001, Alexei Kitaev was the first to publish the idea of using Majorana fermions as qubits to store quantum information [12]. His conception refers to the fact that the two states $|0\rangle$ and $|1\rangle$ can be distinguished by the presence or absence of a quasi-particle. His so-called "toy model" is based on the pairing of a chain consisting of operators that can generate or annihilate spinless fermions and each of them represents the sum of two Majorana operators. While in a non-topological phase always two Majorana operators of the same fermionic operator are paired, there is in a topological phase a pairing of Majorana operators of two neighboring fermionic operators and Majorana-like states, termed as *Majorana bound states* (MBS) or *Majorana zero modes* (MZM), arise at the ends of the chain (see figure 3.2).

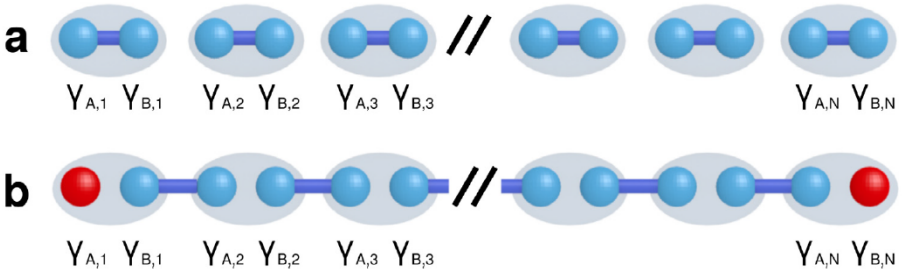

Figure 3.2: *Kitaev's "toy model" of 1D-spinless p-wave superconductors, showing the (**a**) trivial phase and (**b**) topological phase, that leads to unpaired Majorana operators in the chain end (red). Source: Reprinted figure with permission from Rémy Pawlak et al., Majorana fermions in magnetic chains, Progress in Particle and Nuclear Physics, **107**, 1-19 (2019). ©2019 by Elsevier B.V.*

But while in the Kitaev model a p-wave superconductor was required, the concept can be transferred as well to s-wave superconductors, as they exhibit in interaction with adsorbed magnetic impurities similar properties [14]. Therefore, semiconducting nanowires with large spin-orbit coupling (due to the Rashba effect) [15, 150–153] and atomic chains [154–158], both proximitized to an s-wave superconductor, have been predicted to be the most promising candidates to realize a Majorana fermion. More information on the theoretical implementation of MBS and their suitability for the use as qubits can be found in the reviews by Jason Alicea [148], Carlo Beenakker [120] and Masatoshi Sato and Satoshi Fujimoto [134].

The experimental realization and observation of MBSs was first published in 2012 by Vincent Mourik *et al.* by means of the investigation of semi-conducting InSb nanowires in contact with the superconductor NbTiN [15]. Here, tunnel barriers in the nanowire were created and the transport through the gate used to estimate spectroscopic properties at various position on the nanowire. Although this study and several similar ones [159–161] agreed with the calculations of the theory [150, 151], a direct localization of the MBS at the end of the nanowire by transport measurements has not been achieved so far. This reveals a general limitation of the transport measurement and indicates the advantages of using direct localizing methods, such as SPM [162].

3.1.5 Detection of MBS by SPM techniques

After a first experimental evidence of YSR-states with SPM has already been shown in 1997 by Ali Yazdani *et al.*, who investigated the local conductivity of Mn adatoms on Nb(110) [143], the first experimental proof of an MBS in real space was also achieved by Yazdani's group: In 2014, Stevan Nadj-Perge *et al.* provided this evidence by studying chains of Fe atoms on a Pb(110) surface in an STM under UHV conditions [17]. The Fe atoms assembled themselves as atomic chains along the [110] axis of the Pb(110) crystal. While each chain was attached to a cluster of several Fe atoms, the clusters have also been observed on other regions of the Pb terraces independently from the chains (see figure 3.3 a).

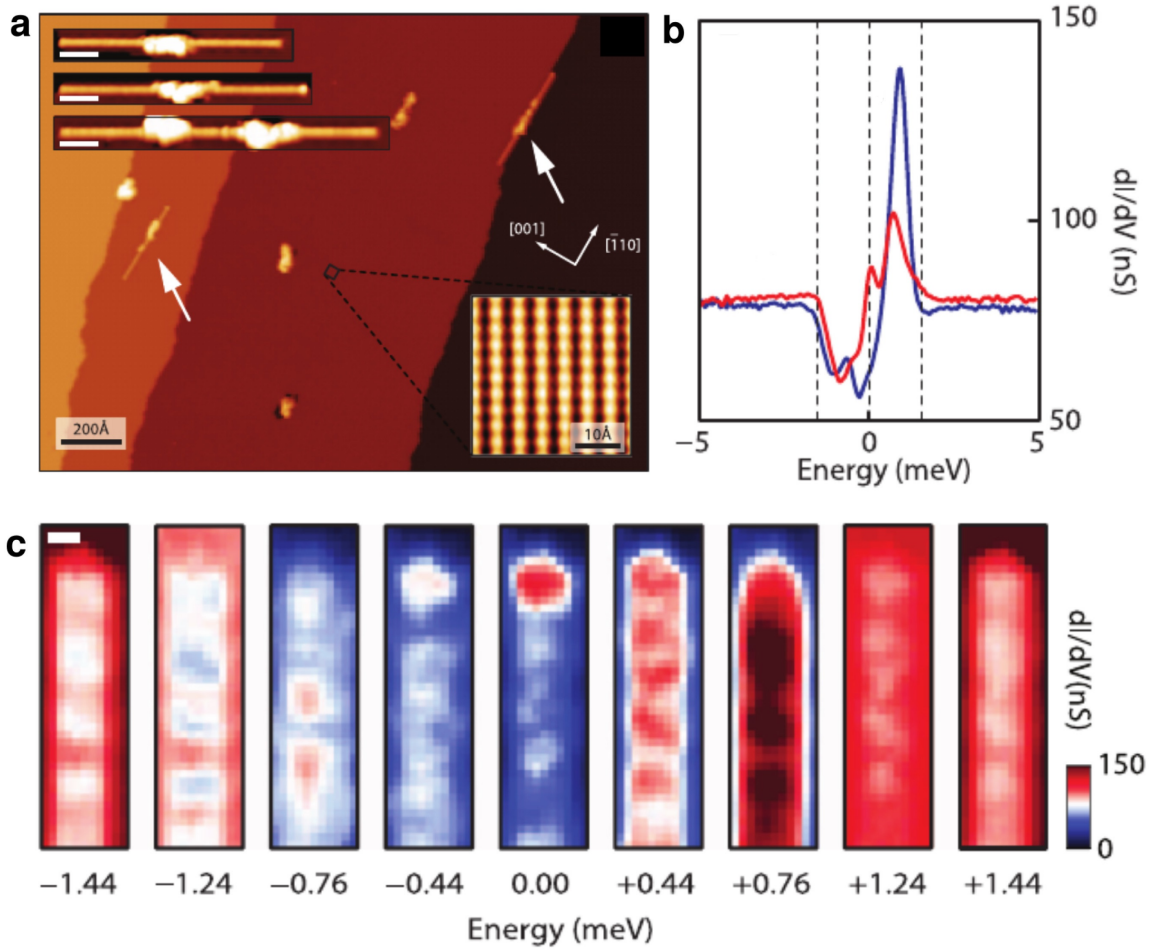

Figure 3.3: *(**a**) STM overview image after Fe adsorption on Pb(110). The arrows indicate the position of the self-assembled atomic Fe chains. (**b**) dI/dV conductance measurement in the middle of an atomic Fe chain (blue) and at its terminus. The superconducting gap ($\Delta = \pm 1.44$ V) and the zero bias line is marked with dotted lines. (**c**) dI/dV maps of the chain terminus for different bias voltages within the gap Δ (scale bar is 1 nm). Source: Nadj-Perge et al., Science **346**, 602-607 (2014). Reprinted with permission from AAAS.*

The MBS was verified by observing a zero bias conductance peak (ZBCP) in a local dI/dV-spectrum at the chain end, which does not appear in the middle of the chain (see figure 3.3 b). In addition to that, dI/dV-maps at different bias voltages (see figure 3.3 c) showed for $E = 0$ V a high LDOS only at the end of the chain [17]. This can be seen as further evidence for a ZBCP and thus it supports the suitability of STM for proving the zero energy resonance at the boundary of the chain.

The first visualization of individual atoms within the chain by AFM was achieved in 2016 by Rémy Pawlak *et al.*, who observed on Pb(110) similar chains with impurities (see figure 3.4 a,b), but as well defect-free chains (see figure 3.4 c,d) [19]. In the AFM image individual atoms of the chain appeared as protrusions (see figure 3.4 b).

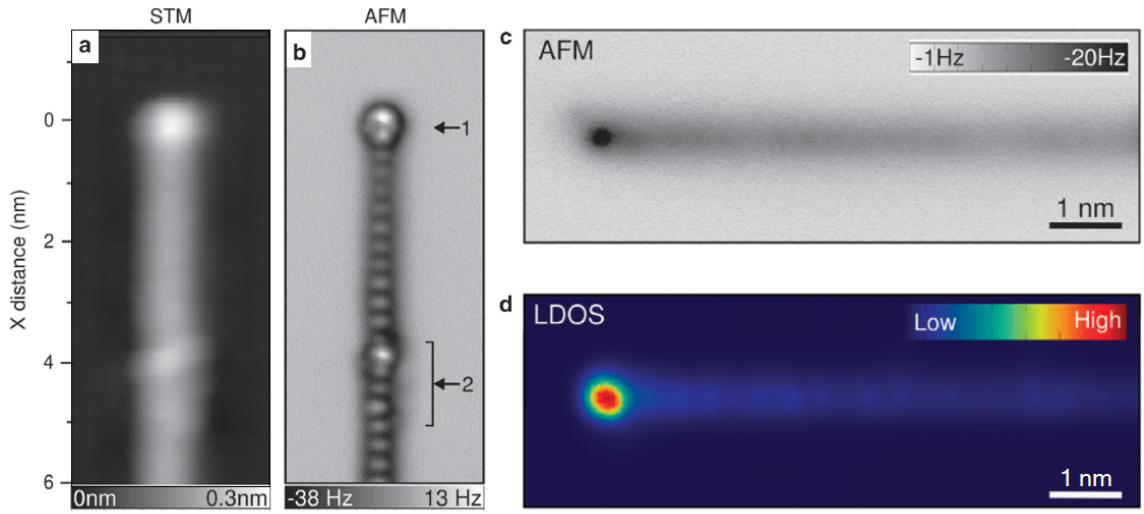

Figure 3.4: *(**a**) STM image (I_t = 10 pA, V_b = -10 mV) of a Fe chain with impurity on Pb(110) and (**b**) corresponding AFM image at constant height. (**c**) AFM image of a defect-free chain (according to (**a**) $\Delta z \approx 50$ pm) and (**d**) corresponding zero-bias dI/dV-map. Source: Pawlak et al., npj Quantum Information **2**, 16035 (2016).*

At the end of the chains with defects (arrow 1), a significantly lower negative frequency change was measured (Δf = -2 Hz instead of -20 Hz), which indicates an increase in repulsive forces. In addition, the formation of a round halo has been observed as further signature for the MBS. At the impurity (arrow 2), on the other hand, this halo is missing and the frequency change is significantly lower (Δf = -10 Hz).

An AFM measurement on a defect-free chain (see figure 3.4 c) exhibited also a distinct signature at the terminus of the chain. However, the frequency change relative to the rest of the chain is here negative, which was attributed to a larger tip-sample distance compared to figure 3.4 b) (+50 pm). The larger distance has also been seen as an explanation for the lack of atomic resolution. A measurement of the LDOS at zero-bias confirmed analogous to the measurements by Nadj-Perge *et al.* [17] the presence of an MBS, both in chains with defects (not shown) and in those without (see figure 3.4 d).

Further experiments on self-assembled atomic Fe chains on Pb surfaces confirmed the presence of an MBS at the terminus of the chain and obtained by spin-polarized measurements additional information on the sup-gap states and the ZBCP [18, 163, 164].

Michael Ruby *et al.* reported e.g. in 2015 on similar measurements of Fe chains on Pb(111) [18]. Here, dI/dV measurements with superconducting tips showed a significant improvement in the spatial resolution. However, due to the use of these tips the ZBCP was split and shifted by $\Delta_{tip} = \pm$ 1.42 meV, which represents the gap of the tip. Furthermore, a difference in the intensity of both ZBCP indicated an additional contribution from YSR resonances. Nevertheless, a comparison with measurements above the critical temperature approved the origin of the ZBCP from the MBS.

In addition to the experiments with Fe chains on Pb, other types of adatoms have also been examined by Michael Ruby *et al.* for the appearance of an MBS. In experiments with Co adatoms similar atomic chains could be formed, but no ZBCP has been measured at the terminus of the chain. Although the conditions for the formation of an MBS are met analogously to Pb (see subsection 3.1.4), the lack of a ZBCP and an increased LDOS at the end of the chain has been explained by the different position of the Fermi level. This could result in hybridization between the Fermi points, which prevents the formation of the topological phase [165].

In his PhD Thesis, which deals with magnetic impurities on superconducting Pb [166], Ruby also reported on the adsorption of Mn adatoms on Pb(110), but under similar preparation conditions the Mn adatoms did not self-assemble to chains. Only for growth temperatures 100 K lower, chains have been found, however, the chain appears as depression and seemed to be embedded into the Pb surface and did not exhibit signatures for MBSs [166]. Nevertheless, measurements of Mn dimers on top of the Pb surface showed a hybridization of YSR-states and thus a realization of an MBS seems still possible if longer chains could be formed by a manipulated shift of adatoms [167].

Indeed, Scanning probe microscopy (SPM) has already proven the possibility of a controlled repositioning of adsorbates, both in vertical and lateral direction. Atoms as well as molecules can be pushed, pulled or slid over a surface [168–170], but also picked up and dropped with the probing tip [171–174]. Lateral repositioning of adatoms is also an promising asset as it could serve as unique opportunity to design fault-less atomic structures with novel electronic properties [168, 175, 176].

However, advances in manipulation experiments or contrast enhancement with functionalized tips are hitherto at their infancy when studying superconducting surfaces by STM/AFM. Although the earliest proposal for observing MBSs suggested a one-by-one manipulation of Fe adatoms to form atomic chains on an *s*-wave superconductor [154], this strategy has not been fulfilled yet on Pb surfaces. In 2018, Howon Kim *et al.* first reported on the atom-by-atom construction of atomic Fe chains on superconducting Re(0001) surfaces [20]. The length varied from 3 up to 40 atoms (see figure 3.5 c).

The manipulation has been performed first vertically by picking up several Fe atoms from ML-thick Fe islands on Re(0001) and releasing them on bare Re(0001) terraces (see figure 3.5 a), following a routine developed for Ag and Cu adatoms [177]. Then, the adatoms were checked by STS measurements to exhibit the characteristics for YSR-states. If so, the Fe adatoms were shifted laterally to form dimers and chains (see figure 3.5 b + c). For this purpose, the set-point was increased from 5 nA to 90-120 nA, the tip was placed next to the atom and then moved to the desired target position. The MBS could be verified by zero-bias dI/dV maps [20].

Additionally, Anand Kamlapure *et al.* reported in 2018 on the atom-by-atom construction of atomic Fe chains on oxygen-reconstructed tantalum (Ta(100)-(3×3)O). They were able to perform the formation of the chains solely by vertical manipulation

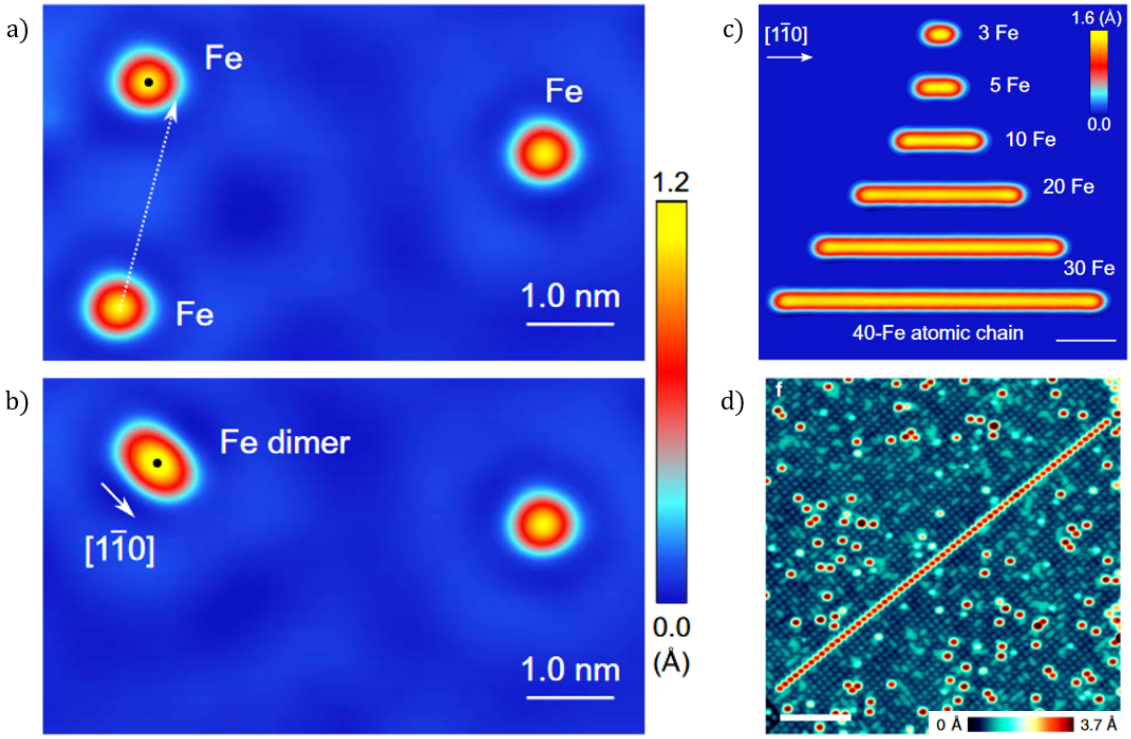

Figure 3.5: *(**a+b**) STM image (I_t = 5 nA, V_b = 3 mV) of isolated Fe atoms on clean Re(0001). The dotted arrow indicates the lateral shift, performed to obtain a Fe dimer. (**c**) STM image (I_t = 5 nA, V_b = 3 mV) of artificially formed atomic Fe chains on Re(0001), scale bar 2 nm. Source: Kim et al. Sci. Adv.* ***4****, eaar5251 (2018).*
*(**d**) STM image of an atom-by-atom formed chain of 63 Fe atoms on Ta(100)-O, scale bar 10 nm. Source: Kamlapure et al. Nature Communications* ***9****, 3253 (2018).*

and achieved chains of up to 63 Fe atoms (see figure 3.5 d) [21]. Although, the single adatoms showed typical characteristics for YSR-states, the emergence of MBSs at the chain end has not been detected for this system, which the authors explain by an inhomogeneous and weak exchange coupling among the Fe atoms in the chain and the substrate.

Nevertheless, the results of atom-by-atom manipulation on superconductors published so far can be seen as an important initiation for future experiments to design complex atomic structures of variable length on various superconductors. Since the system of Fe chains on Pb surfaces has been investigated most frequently so far, it would be very promising to be able to carry out the manipulation of Fe adatoms on Pb surfaces as well. Here, also an electronic decoupling of adatoms and molecules from the superconducting Pb surface could be used as a possibility to simplify the manipulation process.

More information on the manipulation process with SPM techniques in general [178] and an overview on the published literature dealing with the detection of MBSs by SPM methods in magnetic chains on superconductors [179] can be found in reviews .

3.2 Introduction to single-electron charging and molecular quantum dots

Within the last thirty years, the field of single-electron charging has developed into an enormously important area in nanoscience. This can mainly be explained by the application of this principle in single-electron transistors (SET), which are able to confine individual charges to discrete energy levels [180–183]. Contrary to conventional transistors, where the switching is dependent on adding or removing an electron flux, SETs turn on and off by adding a single electron [184].

Quantum dots (QDs) represent a typical possibility of realizing SETs. They are also seen as basis for realizing qubits [10]. For the investigation of various types of QDs, SPM techniques have proven in several studies to be particularly suitable, as their high resolution enables them to sense the tunneling of single electrons at the atomic level [22, 25, 185–190]. QDs are mostly realized by lithographic methods, self-assembly or the insertion of defects in molecular layers. Within the last ten years, however, an analogous behavior has also been observed in two-dimensional molecular layers, where individual molecules have shown the function of a QD [27–30, 191–193].

The following subsections will first give a short general introduction on single-electron transistors (subsection 3.2.1) and quantum dots (subsection 3.2.2). Thereafter, the focus will be put on the investigation of QDs with SPM methods (subsection 3.2.3). Finally, a review of the already available literature on the QD-like behavior of 2D molecular films is given (subsection 3.2.4).

3.2.1 Single-electron transistors (SETs)

The starting point of the research on single-electron transistors (SETs) is often associated with a publication of the later Nobel Prize winner David James Thouless in 1978, in which he pointed out that the miniaturization of a conductor has a decisive influence on its electronic properties [194]. In recent days this topic was known as *Mesoscopic physics*, since the systems were in sub-micron size between the atomic and macroscopic range [184]. The first single-electron transistor has been achieved by Dmitri V. Averin and Konstantin K. Likharev in 1986 [195]. The decisive factor here was the utilization of the so-called Coulomb blockade, which describes the disappearance of the electrical conductivity for an object, when - due to its low electrical capacity - it cannot longer accept or release an electrical charge. Hence, it creates a strong Coulomb repulsion and does not conduct above or beneath a certain threshold voltage.

While classical field effect transistors (FETs) turn on only once as electrons are added to it, submicron-size transistors, such as SETs, turn on and off by adding a single electron. This is primarily a consequence of the quantization of charge and explains, why a single electron can cause a dramatical change of the capacitance. However, it is crucial for such phenomena to confine electrons in a small region. If, for example,

electrons are confined to a very small area with the help of insulators or electric fields, this system can only be filled with a limited number of electrons, which are on discrete energy levels. It thus resembles the electronic levels of a single atom, which is why the term "*artificial atom*" is also used to describe it [196].

Fully occupied, a system with confined states is able to develop the previously mentioned Coulomb blockade and it fulfills at a correspondingly low degree of miniaturization already quantum mechanical laws. The developed Coulomb blockade has the function of a tunnel barrier here and the conductance through the barrier shows for voltages in the mV range oscillations which are representing the energy needed to add single electrons into the confined pool of electrons [197, 198]. The area, in which the confinement of electrons is made possible, represents thus the central component of an SET and has been called *quantum dot* or *Coulomb island* [196], although the latter name is today not very common anymore.

3.2.2 Quantum dots (QDs)

In general, the term QD is used to describe a semiconductor particle with a size of a few nm, that - due to quantum mechanical effects - has different electronic and optical properties than a macroscopic particle of the same material. Similar to atoms or molecules they can confine electrons or electron holes with discrete energy states and wave functions. In contrast to atoms, their shape, size or the number of confined electrons can be manipulated and therefore certain electronic or optical properties can be tailored. The coupling of single QDs to a so-called double-dot system exhibits a molecular-like state and is also known as *artificial molecule* [199]. Furthermore, the coupling makes QDs to a promising platform for the realization of qubits [10].

In addition to the utilization in SETs or as platform for qubits, quantum dots (QDs) are also famous for being used in optical applications. Their confinement of electrons is e.g. the basis for a specific optical absorption coefficient [200] and influences their fluorescence spectrum. The fluorescence lifetime depends on the size of the quantum dot and can be prolonged by increasing the size of a QD [201]. A more specific description on this and other applications related to their optical properties can be found in the literature [202].

Today, QDs are mainly produced by lithographic methods, wet chemical processes, molecular beam epitaxy, self-assembly or the insertion of defects into molecular layers (such as doping of semi-conductors). Their occurence is also possible in quantum wells [203]. When dealing with QDs, it is important to point out possible toxic effects. This is relevant due to the fact that engineered QDs might also differ significantly from comparable macroscopic objects in their physiochemical properties [204]. Especially in the case of already toxic raw materials such as Cd, Pb, Se or As, composed quantum dots can represent a particular hazard potential. This can be also a motivation to investigate on toxicologically harmless molecular layers with QD-like properties.

3.2.3 Detection of quantum dots by SPM techniques

The experimental investigations on the phenomenon of a Coulomb blockade as a characteristic for QDs were first characterized by transport measurements of electrons [205]. Although these observations confirmed the confinement of electrons for certain applications, they did not offer a spatial resolution of the system and were not applicable to all types of quantum dots. A remedy for this showed the application of scanning probe microscopy (SPM), which has proven itself by applying it to the various types of QDs: In the first years by using the experimentally demanding techniques of scanning capacitance microscopy (SCM) and scanning single-electron transistor microscopy (SSET), later also by the standard STM- and AFM-techniques.

The first experimental evidence of single electron recombinations with SPM methods was achieved in 1990 by Christian Schönenberger and Santos F. Alvarado, who demonstrated the discharge of single electrons with the help of AFM and propagated the suitability of SPM for measuring charge quantization [206]. After investigations on the electrical conductivity of nanotubes delivered first signs for a single-electron charging, the presence of a Coulomb blockade in nanotubes was concluded [207]. Shortly afterwards, Marc Bockrath *et al.* [208] as well as Michael T. Woodside and Paul L. McEuen [22] reported for the first time on ring-like structures in Scanning Gate Microscopy (SGM) measurements, which have been assigned to individual Coulomb oscillations. The oscillations can be directly associated with the overcoming of the Coulomb blockade by single electrons and thus revealed the existence of a QD [197, 198]. The rings as a signature for QDs were confirmed shortly afterwards also by differential conductance (dI/dV) measurements [186]. In addition to that, the overcome of the Coulomb blockade is also represented by quantized jumps in the conductance (dI/dV) or force signal (Δf) [187,206]. By now, the phenomenon of single-electron charging has been proven with these rings or leaps in a variety of systems, which can be subdivided into the following groups:

- charge states in nanotubes [22, 185, 190, 207–209]
- charge states in various heterostructures [25, 186–189, 206, 210]
- charge states in graphene-related heterostructures [211–218]
- charge states in single impurities or single adatoms [23, 24, 26, 40, 77, 219–222]
- charge states of single molecules: [192, 215, 223–225]
- charge states within 2D molecular layers [27–30, 191–193]

It has to be noted that this enumeration is not exhaustive and the observation of the confinement of electrons is sometimes described as charge state and not directly associated with QDs. Additionally, for this multitude of different systems and applications, various explanatory models have been developed so far. In order to proceed structurally, the occurrence of QDs in 2D molecular layers is therefore considered separately (see subsection 3.2.4).

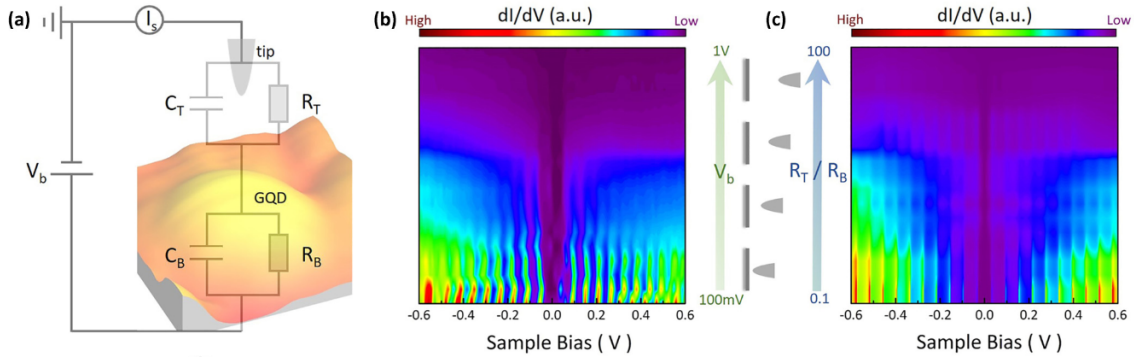

Figure 3.6: *(**a**) Scheme of the double-barrier tunnel junction (DBTJ), representing the interaction between SPM tip (capacitance C_T and resistance R_T) and QD (capacitance C_B and resistance R_B). (**b**) STS spectra for graphene QDs at different tip-sample distances (caused by varying tip bias V_b). (**c**) Simulated STS-spectrum by applying DBTJ for a similar situation as measured in (b); here the ratio R_T/R_B represents the change in the tip bias V_b. Source: Reprinted figure with permission from Jia-Bin Qiao et al., Bound States in nanoscale graphene quantum dots in a continous graphene sheet, Phys. Rev. B, **95**, 081409 (2017). ©2017 by the American Physical Society.*

The article by Jia-Bin Qiao *et al.* [214] provides a very good summary of the development of the leaps and ring-like features in the dI/dV-maps: Here, the theory of the so-called "orthodox Coulomb blockade", which was published in 1991 by Mark Amman *et al.* [226] and Ashraf Elfar Hanna and Michael Tinkham [227], is taken as basis. It deals with a double-barrier tunnel junction (DBTJ), which - applied to the investigation of QDs with SPM methods - treats the tip as well as the individual QD as a tunnel barrier junction.

Each junction consists of a capacitor and a resistor and it is also assumed that the QD is electronically isolated from the rest of the surface (see figure 3.6 a). If the distance between the tip and the QD is changed in this system, this corresponds to a change in the tunnel resistance of the tip R_T, which influences the entire tunnel spectrum of the DBTJ and can be verified using dI/dV-measurements. A very good agreement between the "orthodox Coulomb blockade" model and real dI/dV-measurements has been demonstrated on graphene QDs by varying the tip-distance (see figure 3.6 b and c). For high distances the spectra showed the a zero-conductance gap as signature for the Coulomb blockade (CB) and at smaller distances they exhibited tunneling peaks as signature for a Coulomb staircase (CS) [214].

In accordance with this model, the emergence of the ring-like structures is explained by the fact that the STM tip induces spatially varied band bending when scanning over the QD [212,213]. This type of gating causes the position of the measured energy levels of the QD to shift depending on the distance between tip and induction center. In the dI/dV-maps maxima arise, where the Fermi level overlaps with the CS-peaks of the bent energy bands. A schematic of this effect is shown in figure 3.7 a.

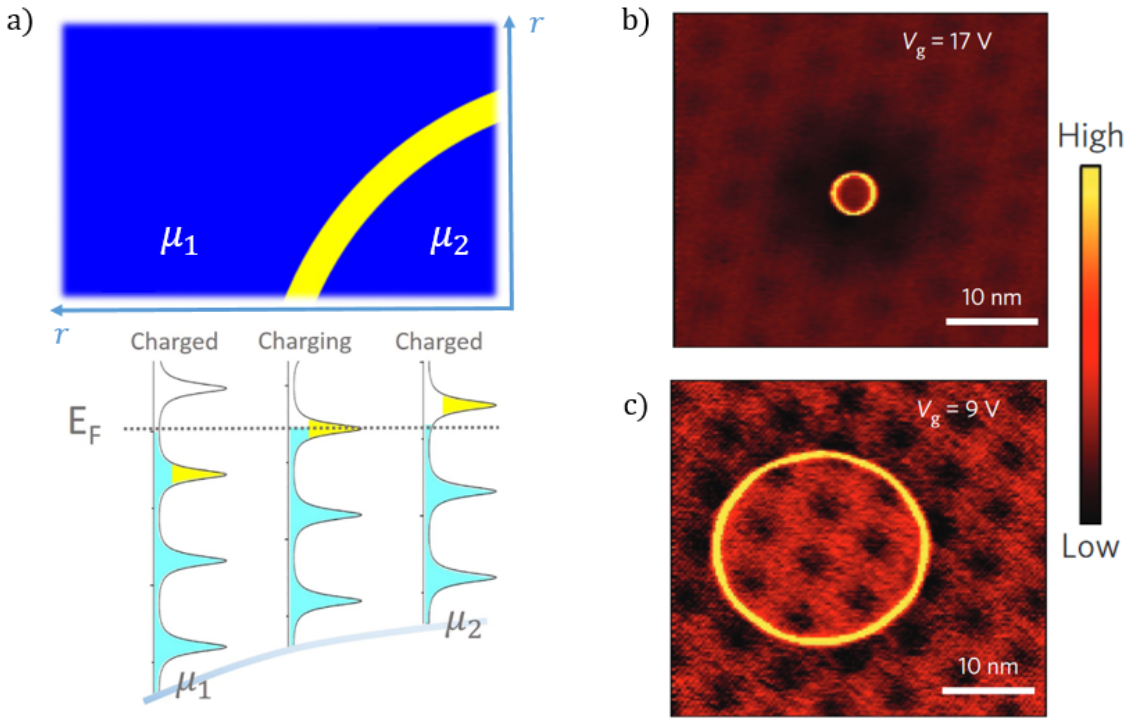

Figure 3.7: *(**a**) Schematic illustration of the origin of the charging rings in dI/dV-maps: For different radii r from the QD center, the scanning tip bends the energy bands of the QD (grey line on the bottom); only if the Fermi level overlaps with filled states (CS) caused by charging, a ring-like feature arises, otherwise (chemical potential μ_1 and μ_2) it is not detectable. Source: Reprinted figure with permission from Jia-Bin Qiao et al., Bound States in nanoscale graphene quantum dots in a continous graphene sheet, Phys. Rev. B, **95**, 081409 (2017). ©2017 by the American Physical Society. (**b**) dI/dV-map of a BN-defect on graphene (I_t = 0.4 nA, V_s = -0.3 V) at a backgate voltage V_g = 17 V. (**c**) Similar dI/dV-map for V_g = 9 V. Source: Reprinted figure with permission from Dilon Wong et al., Characterization and manipulation of individual defects in insulating hexagonal boron nitride using scanning tunnelling microscopy, Nature Nanotechnology, **10**, 949 (2015). ©2015.*

In case there are several electrons confined in a single QD, multiple ring-like features emerge, since each ring represents exactly one Coulomb oscillation, caused by exactly one confined electron [22]. However, as a consequence, the strength of the band-bending mechanism depends crucially on the tip-sample distance and hence on the tip bias voltage. According to each QD-system, the radii of the charging rings might increase or decrease for different tip voltages (see figure 3.7 b+c). Additionally, a specific threshold voltage has to be exceeded to initiate the occupation of an energy level in a QD. Although, according to the model, the band bending is expected to be equal in all directions and the charge ring thus circular, local asymmetries in the charge distribution of a QD or other electronic influences in its vicinity might influence the shape of the charging ring and cause elliptical features [228] or further irregularities [209]. An overlap of charging rings from neighboring QDs is also possible [22].

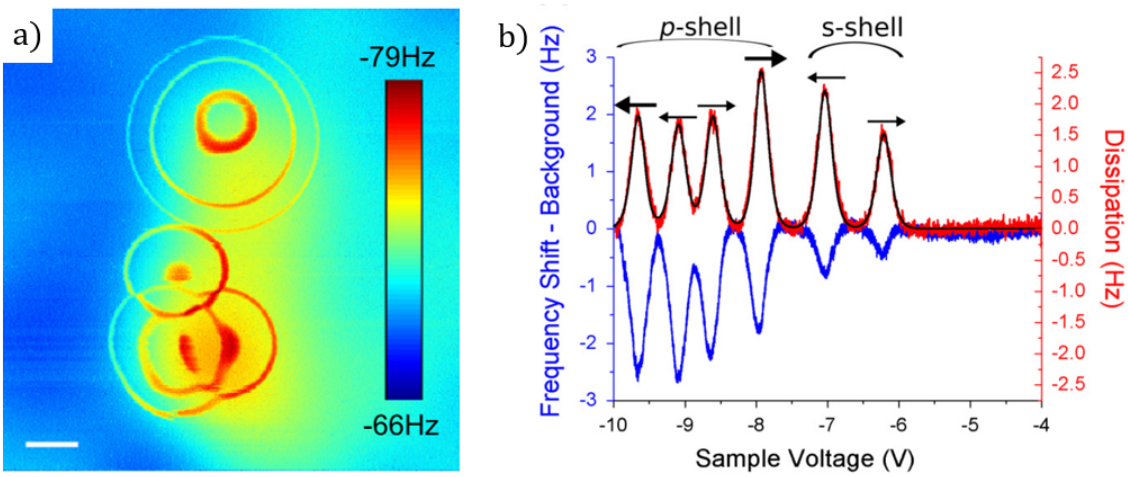

Figure 3.8: *(**a**) AFM-image (taken at 4.5 K, bias-voltage -8 V, scale bar: 20 nm) of self-assembled InAs QDs, grown on InP. (**b**) Δf-(blue) and dissipation-(red) spectra upon the upper set of concentric rings shown in (a), representing the occupation of energy levels. Source: Cockins et al., Energy levels of few-electron quantum dots imaged and characterized by atomic force microscopy, PNAS, **107**, 21, 9496-9501 (2010).*

In addition to dI/dV-maps, the peaks and ring-like features as signature for single-electron charging can also be measured by AFM- or dissipation measurements. Here, a tunneling from tip to QD is negligible, but the use of a bias voltage between cantilever and surface creates an oscillating electric field in the junction of the QD that might change its charge distribution, which can be detected in the feedback of the cantilever's oscillation [229]. As a result, similar rings as in dI/dV appear (see figure 3.8 a), but in the Δf-spectra similar dips mark the Coulomb oscillation of a single electron transfer (see figure 3.8 b). Due to their negative shift they are attributed to attractive forces and electrostatic forces are assumed to be the main cause for them [25, 29].

3.2.4 Quantum dots in molecular layers

The fact, that the confinement of electrons could also be detected in individual molecules within molecular layers, is included in a long-term development, in which individual molecules or even parts of molecules are assigned to have properties of electronic components. It deals with the question of how "smart" a single molecule can be, so that logical devices can be made from it [230]. In 1974, Ari Aviram and Mark Ratner described a theory of molecular rectifiers, where a single molecule has an electron donor moiety and an electron acceptor moiety and thus, due to its donor-acceptor character, becomes a kind of molecular P-N junction, in which the current flows only in a certain direction [231]. The advantage is, that miniaturization is here not tied to a resolution limit, as e.g. for lithographic methods. In addition, the use of quantum computing promises enormous advances in the design of specific molecules, which enable application-specific modifications much more easily than the adaptation of a lithographic manufacturing process could offer.

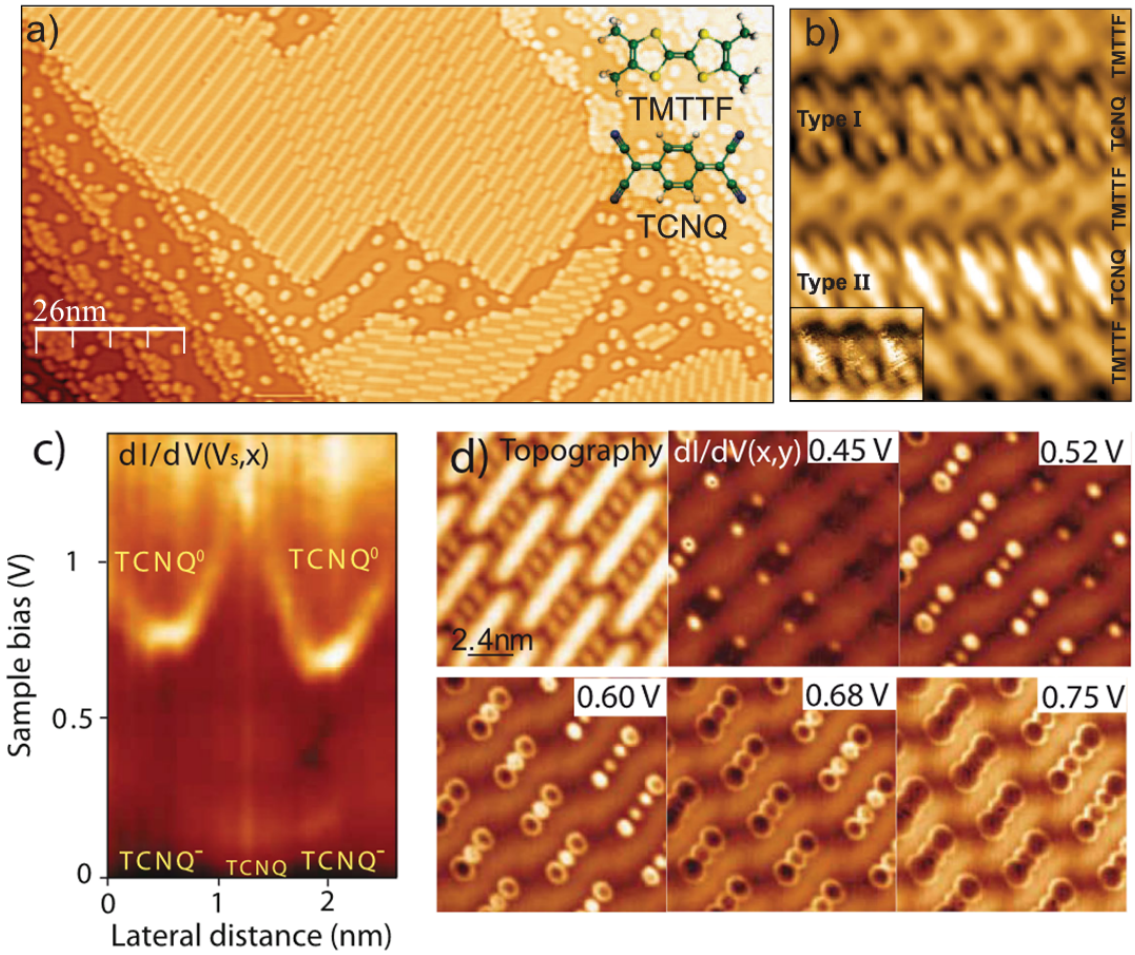

Figure 3.9: *(**a**) STM image of TMTTF-TCNQ domains on Au(111) (I_t = 0.4 nA, V_s = 1 V). (**b**) Detailed STM-image (I_t = 0.17 nA, V_s = 90 mV) of the mixed TMTTF-TCNQ monolayer, showing different charge states, tunable by the tip (see inset). (**c**) Spectral map of TCNQ molecules, showing dI/dV versus lateral position and sample bias. (**d**) dI/dV-maps of a mixed TMTTF-TCNQ monolayer for different tip bias voltages (I_t = 0.7 nA). Source: Reprinted figure with permission from I. Fernández-Torrente et al., Gating the Charge State of Single Molecules by Local Electric Fields, PRL, **108**, 036801 (2012). ©2012 by the American Physical Society.*

Following the idea of Aviram and Ratner, charge states can be measured as a donor-acceptor property depending on the respective adsorption site [232], or can be caused by incorporating dopants [233]. However, a regular confinement of electrons can also emerge within 2D molecular layers solely through the self-assembly of the molecules. Their signatures correspond to those from QDs and hence the properties in this kind of layers can be referred to as molecular quantum dots.

Such molecular quantum dots have been reported by Isabel Fernández-Torrente *et al.*, who investigated mixed monolayers of tetracyanoquinodimethane (TCNQ) and tetramethyltetrathiafulvalene (TMTTF) on an Au(111) surface (see figure 3.9 a) [27].

Here, the TCNQ is known as electron-acceptor and the TMTTF as electron-donor. Two different types of molecular rows could be determined for TCNQ (see figure 3.9 b): A type I, appearing dark in STM, exhibiting a zero-bias peak (ZBP) caused by the Kondo effect and revealing a strong and a weaker peak in the dI/dV-spectra that leads to ring-like bias- and lateral-dependent features in conductance maps (see figure 3.9 c+d) as well as a type II without ZBP, appearing bright in STM and exhibiting a strong and a weaker dip in the dI/dV-spectra with analogous behavior as for the peaks. In accordance to the model for single-electron confinement (cf. figure 3.7 b), the type I is interpreted as negative and the type II as neutral state. For type I, a positive bias voltage leads to a local discharging, which is revealed by the emergence of the dI/dV-peak and the ring-like features. It has to be above a specific threshold and depends on the lateral distance. On the other hand, an analogous negative bias voltage charges type II molecules and the dI/dV-dip occurs as signature.

The different graduation of the charging rings along the molecular rows shown in figure 3.9 d) is understood as a modulation of the LUMO alignment resulting from the inhomogeneous surface potential of the Au(111) herring-bone reconstruction. The modulation shifts the energy levels so strongly, that it already leads to different ground states without the gating of the tip. Thus, gating potential between the TCNQ molecule and the metal surface is tuned both by the tip-sample interaction and by a static potential from variations in the surface potential [27].

Further measurements showing molecular quantum dots have been performed by Nemanja Kocic *et al.*, who reported about a similar occurrence in the edges of a 1,6,7,12-tetraazaperylene (TAPE) monolayer on Ag(111) [28]. Here, the molecular layer consisted of one molecule self-assembled in two different orientations. While for low negative sample bias voltages below a certain threshold the molecular layer appeared similar in STM, it changed for stronger negative voltages: Every second molecule along the edges of the molecular terraces exhibited a larger apparent height and strong dip in the dI/dV-spectrum, that corresponded to a bias-dependent ring-like feature, similar to the one described for TCNQ on Au(111) [27]. Analogously, it has been interpreted as a tip-related gating effect, originated probably by the pair of N atoms sticking out of the molecular layer. The energy difference caused by this gating has been described as $\Delta E = eaV$, where e is the elementary charge, V the applied bias voltage and α the so-called *lever arm*, that depends on the tip-sample distance z. To couple the charge-state transition to the measured frequency shift Δf in AFM, this dependence has been investigated with Δf(V)- and Δf(z)-measurements (see figure 3.10).

Later, these measurements were expanded and resulted in a detailed analysis about the influence of charging events in AFM-measurements [29]. By applying the simple model of a plate capacitor, it has been made a satisfying explanation for the linear scaling of the threshold voltage with the tip-sample distance, which is coupled to the observed Δf-shift of the charging feature shown in figure 3.10. Additionally, these results allow also the estimation of the local contact potential difference (LCPD) and the length of the tip-sample distance.

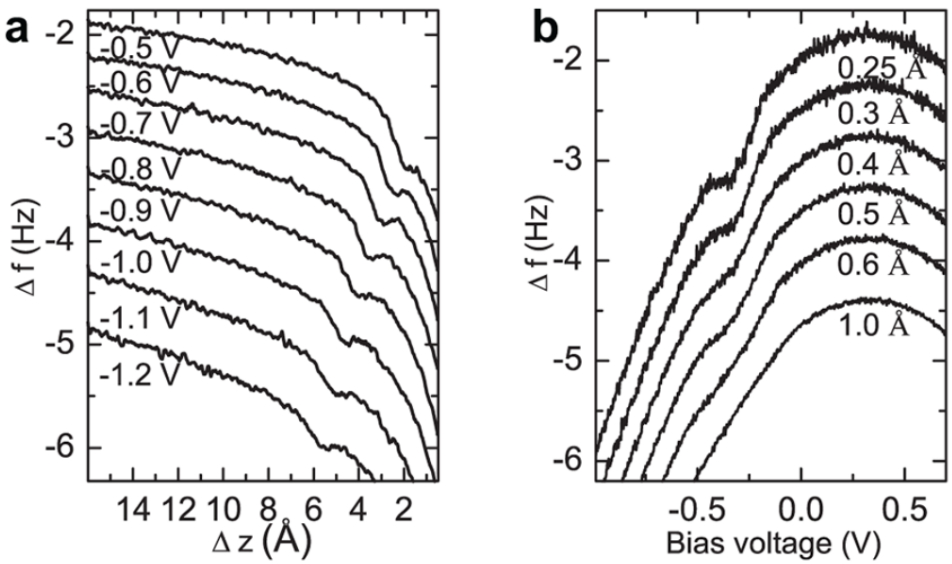

Figure 3.10: *(**a**) $\Delta f(z)$-curves for different sample bias voltages above TAPE edge molecules on Ag(111). (**b**) $\Delta f(V)$-curves for different oscillating amplitudes, representing different tip-sample distances on same position as (a). Source: Reprinted with permission from N. Kocic et al., Periodic Charging of Individual Molecules Coupled to the Motion of an Atomic Force Microscopy Tip, Nano Lett.,* ***15****, 4406-4411 (2015). ©2015, American Chemical Society.*

In a further study on this material system, Nemanja Kocic *et al.* showed the implementation of single-electron charging by scanning-probe-based manipulations [30]. The special chemical state of the edge molecules should be imitated by creating free bonds of the N pairs through the creation of vacancies within the molecular TAPE layer. After the complete removal of individual TAPE molecules succeeded without influencing the arrangement of the other molecules, a similar confinement could be shown with dI/dV-measurements as on the edge molecules, which however varied in detail depending on the chemical environment of the molecule. Thus, the free bonds of the N pair in the TAPE molecule could also be identified as the cause of the electron confinement and that charging of a molecule affects strongly the neighboring molecules.

3.3 Summary

This chapter describes the basic theoretical concepts for the implementation of the experiments shown in this thesis. It reviews the concept of superconductivity, puts the focus on the properties of superconducting Pb and gives an overview on the influence of magnetic impurities on superconductors and the emergence of Majorana bound states (MBS) in topological superconductors. Furthermore, the most important experimental investigations on this topic are summarized, which includes the illustration of a few selected important publications. With the help of this, it is easier to classify the significance of the results described in chapter 4.

In the following, the concept of single-electron charging is introduced and explained in its application in quantum dots (QDs). Thereafter, the focus is put on the experimental investigation on this phenomenon, so that a reference can be made to the later results. This includes the presentation of selected publications on single-charging effects within molecular layers, which are directly compared in the latter chapter on charge state control of molecular quantum dots (see chapter 5).

4

Adsorption of CO, NaCl & Fe on Pb surfaces

The development of functionalized tips obtained by picking a single molecule from a surface, has been an important milestone for low temperature STM/AFM techniques, since the CO tip nowadays enables systematic highly-resolved images of surfaces, molecules and atoms [71, 108, 234]. Despite being well-established on many noble metals, the use of CO-terminated tips still remains rather scarce in the literature [169], which severely limits the use of AFM as imaging tool on superconductors. Lastly, Heinrich *et al.* have demonstrated the possibility to tune the magnetic anisotropy of a single porphyrin molecule by perturbing its ligand field with the STM probe [235,236]. These results not only suggest the importance of future manipulations experiments but also shed new lights into the potential of the electronic decoupling of atoms and molecules from underlying superconductors. With this prospect, the use of alkali-halide islands adsorbed on a superconducting surface and acting as a buffer layer expands the field of functionalized tips. [41, 232, 237, 238].

On superconducting Pb surfaces, the functionalization of STM/AFM tips with CO and the adsorption of CO on Pb surfaces are of particular interest, since the adsorption of atomic chains proximitized to an *s*-wave superconductor is seen as promising platform to realize MBS (see subsection 3.1.4) [17–20, 239, 240]. This could also facilitate the manipulation of single Fe adatoms with STM to create atomic chains, as it has been suggested in the earliest proposal for observing MBSs [154]. Regarding to that, the adsorption of alkali-halide islands, acting as a buffer, might also help in the experimental observation of molecules adsorbed on Pb surfaces.

In this chapter, the topographic features of adsorbed carbon monoxide (CO) molecules on superconducting Pb(111) and Pb(110) surfaces are described in details by using STM at 4.8 K (see subsection 4.1). Additionally, the adsorption of sodium chloride (NaCl) on Pb(111) is investigated (see subsection 4.2). Finally, the adsorption of Fe adatoms on Pb(111) is examined, which includes investigations on their lateral manipulation (see subsection 4.3).

4.1 CO adsorption on bare Pb surfaces

In this section the adsorption of carbon monoxide (CO) molecules on superconducting Pb(111) and Pb(110) surfaces is reported. The investigations are based on STM. Here, the termination of the scanning tip with a CO molecule and its influence on the scanning images is included.

With a lattice parameter of $a_{\mathrm{Pb}} = 4.95$ Å, the height of mono-atomic steps of the Pb(111) surface is expected to be $h_{Pb} = a_{\mathrm{Pb}}/2\sqrt{3} = 1.4$ Å. Experimentally, a pure Pb(111) sample (see figure 4.1 a) shows after sputtering and annealing cycles (see subsection 2.3) typically steps of about 2 $\times h_{\mathrm{Pb}} = 2.7$ Å, which thus corresponds to diatomic steps. It is assumed that this peculiar step height distribution results from quantum size effect of the Pb(111) surface [241]. On the terraces, hexagonal dark spots are visible by STM, which exhibit different between 1.5 nm and 5 nm with and an apparent depression of 0.14 Å. According to subsection 2.3 they originate from the interference of bulk electrons with trapped subsurface Ar gas bubbles after sputtering [114, 242].

After dosing CO for 1 minute at a pressure of 5.0×10^{-8} mbar in the microscope chamber (while the sample is kept at 4.7 K), a coverage of about 0.1-0.2 monolayer CO is expected to adsorb on the metal surface, as observed on various noble metals [174,243]. Figures 4.1 b) and c) show STM topographic images after the adsorption process. While the surface topography remains unchanged in comparison to figure 4.1 a), numerous scan instabilities are now present, which can be attributed to adsorbed CO molecules, diffusing under gentle scan conditions (tunneling resistance of 200 GΩ is used).

Figure 4.1 d) shows an STM profile, taken along the white dashed line inserted in figure 4.1 c). It reveals systematic stochastic jumps, which can be interpreted as tip-induced displacements of single CO molecules [244–246]. It should be emphasized that various scan parameters, as well as tip indentations into the clean Pb surface, were conducted to avoid such instabilities without noticeable improvements.

In the STM scanning process this unintentional CO-tip termination causes an intermittent enhancement of the STM resolution, as illustrated in figure 4.1 e). Here, the atomic lattice of Pb(111) becomes apparent, when the tip is terminated with CO. Unfortunately, the termination is not always stable and is therefore lost at some places, but re-taken in continued scanning.

In comparison to the vertical tip functionalization with CO on (111) surface of various noble metals, the instabilities on Pb are much higher, which severely limits the use of CO-terminated STM/AFM imaging on Pb(111). It should be noted that also other tip terminations (such as Xe) are possible, which can be planned to explore in future measurements.

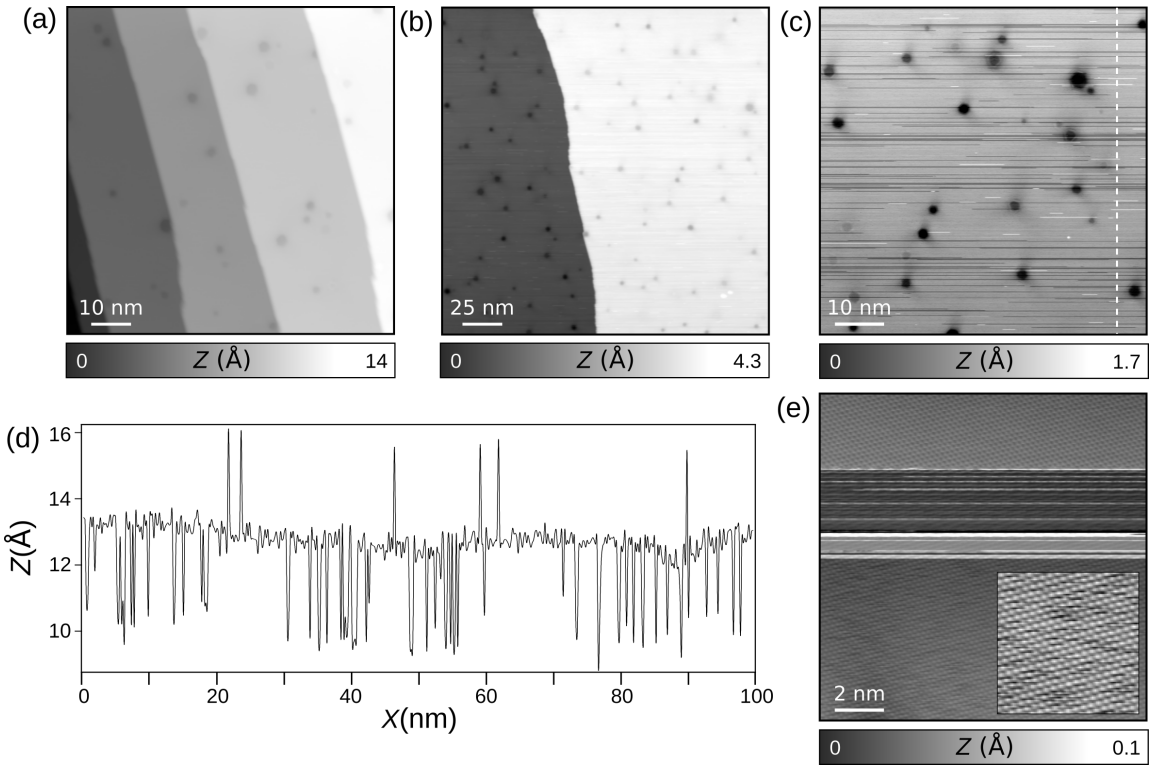

Figure 4.1: ***Carbon monoxide (CO) molecules adsorbed on Pb(111).*** *(**a**) STM overview image of pristine Pb(111) (V_t = -0.1 V, I_t = 1 pA). (**b**) STM image after CO deposition. The estimated coverage is below 0.2 monolayer. (**c**) Close-up STM topography of CO molecules diffusing on the surface during scanning (V_t = -0.1 V, I_t = 40 pA). (**d**) Profile taken along the dashed white line of (c) showing spontaneous CO displacement under tip action. (**e**) Enhanced STM resolution resulting from the termination of the tip by a CO molecule. The inset shows atomic resolution on Pb(111), (V_t = -0.2 V, I_t = 1 pA).*

Similar CO depositions have also been performed on a Pb(110) surface (see figure 4.2 a). Here, the CO molecules appear in STM images as linear aggregates of different lengths, aligned perpendicular to the upper atomic rows of the Pb(110) surface (see structure in figure 2.6). In figure 4.2 b) a detailed image of this aggregate is shown and the upper rows of the Pb(110) are marked with dashed lines.

The aggregates exhibit an apparent height of 0.28 Å (see figure 4.2 c), as extracted from the profile of figure 4.2 b). In this particular case, the protrusion length extends by 18 Å, which corresponds to four Pb rows of the reconstructed Pb(110) surface, as shown in the assumed model, illustrated in figure 4.2 d).

In conclusion, the assumed model displays a strong similarity with the adsorption of CO on a CuO-(2×1) reconstructed surface, as reported by Min Feng *et al.* [247]. There, the authors explain the different lengths of the CO aggregates by monomers or dimers of CO molecules. In accordance to them, it is assumed that the molecules,

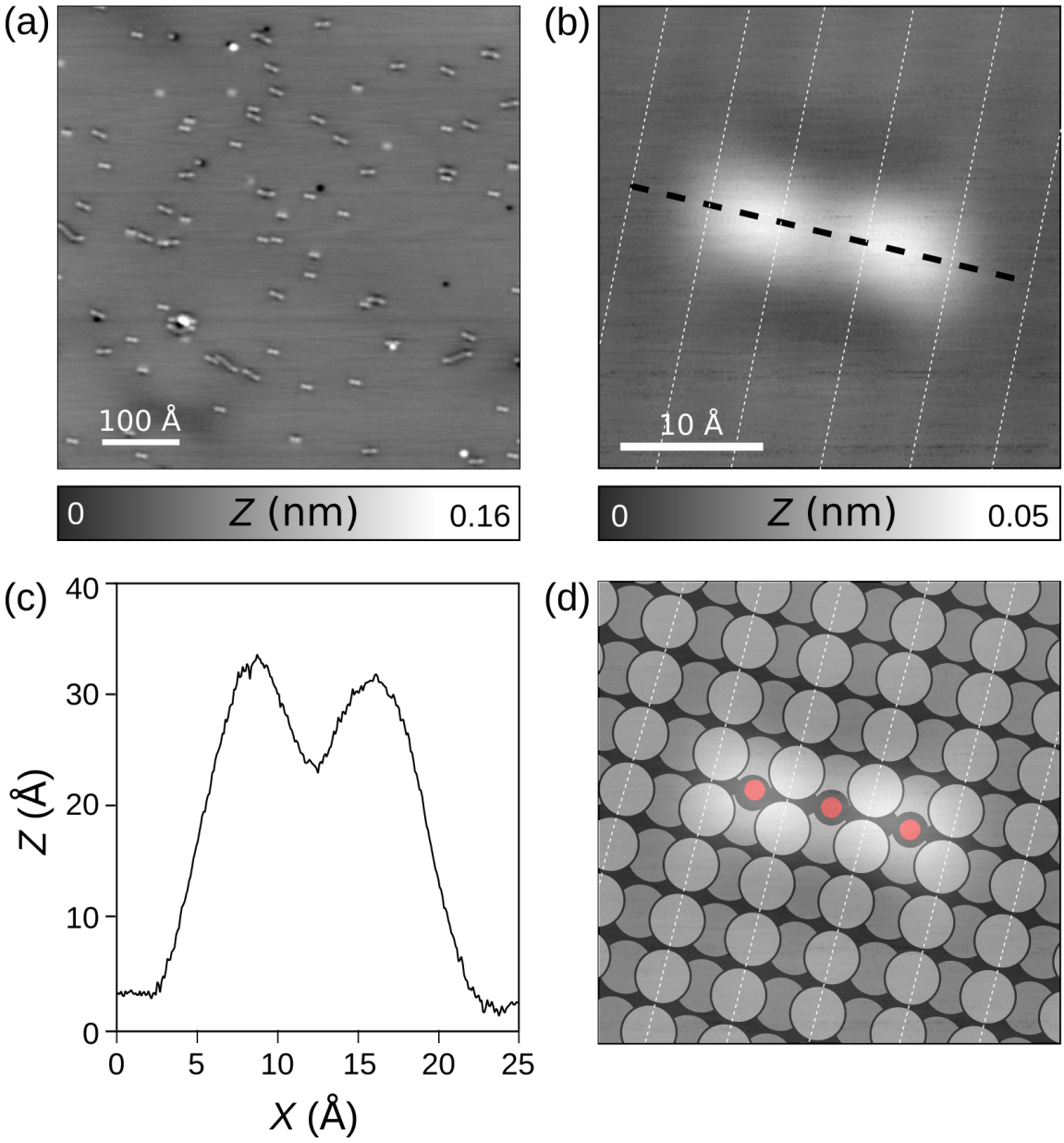

Figure 4.2: ***Adsorption of carbon monoxide (CO) molecules on Pb(110).*** *(**a**) STM overview image of Pb(110) with few CO molecules (V_t = -0.5 V, I_t = 0.5 pA). (**b**) Closed-up STM image of a single CO molecules (V_t = -0.1 V, I_t = 1 pA). (**c**) Profile taken along the dashed white line of (b). (**d**) Sphere model of CO adsorbed on Pb(110). The CO (red spheres) are standing up with protruding oxygen atoms, white gray and dark gray spheres refers to the topmost and downmost Pb atoms of the Pb(110) reconstruction.*

adsorbed in the trench of the Pb(110), are stabilized by forming linear aggregates, which enables STM scans. Thus, the adsorption on Pb(110) differs dramatically from that on Pb(111).

4.2 Growth of NaCl islands on Pb(111)

In this section the adsorption of sodium chloride (NaCl) on superconducting Pb(111) is reported. The investigations on the adsorption and their tip-induced rotation are again based on STM.

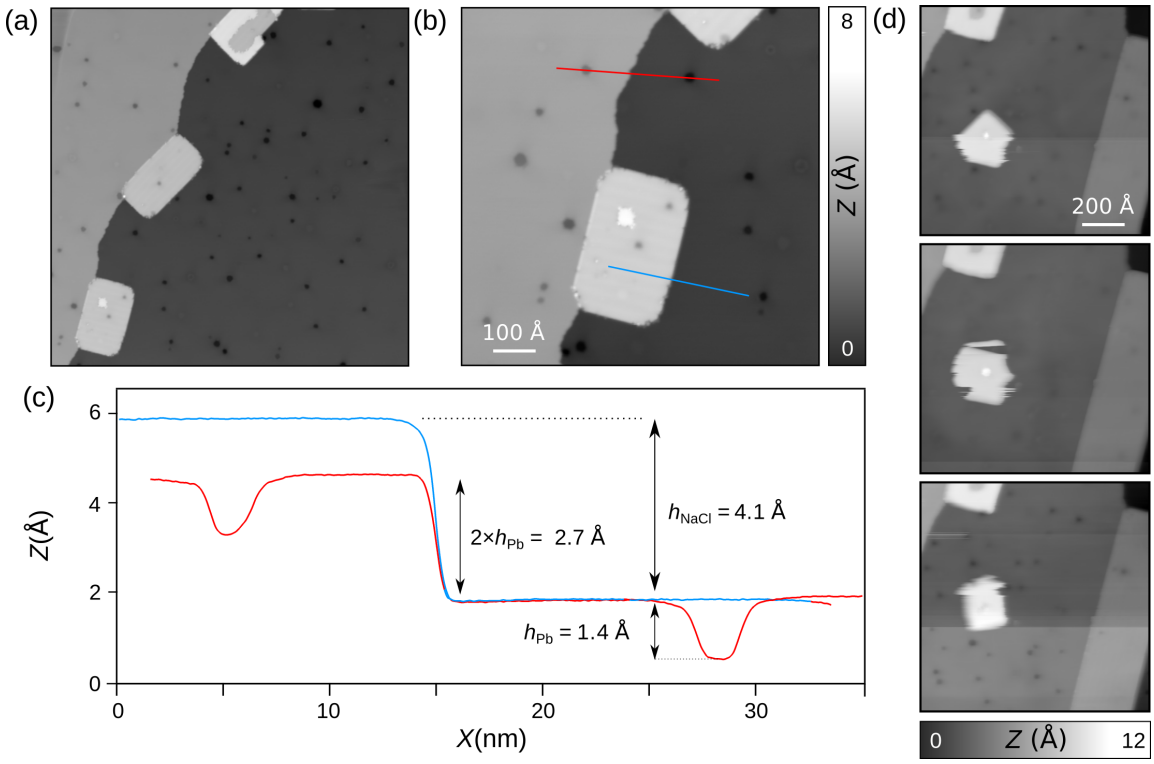

Figure 4.3: ***Adsorption of NaCl on Pb(111).*** *(**a-b**) STM overview image of Pb(111) with quadratic NaCl islands adsorbed at step edges (V_t = -0.4 V, I_t = 1 pA). (**c**) Height profile extracted along the red and blue lines of (b). (**d**) Series of STM image showing the tip-induced rotation of an NaCl island (V_t = -0.4 V, I_t = 40 pA).*

As figures 4.3 a) and b) show, NaCl forms after sublimation from a quartz crucible at room temperature quadratic islands on Pb(111), which are mostly attached to the Pb step edges, but also appear within the Pb terraces (see figure 4.3 d). This process happens without any post-annealing of the surface. The step heights between the NaCl island and the Pb layer underneath are equal to h_{NaCl} = 4.1 Å (see figure 4.3 c) and correspond to the NaCl bilayer, as the extracted profile of Figure 4.3 b) along the red and blue lines displays. This is in agreement with the reported growth of NaCl islands on Cu(111) [248].

The dark protrusions, originating from trapped Ar atoms in the Pb(111) surface [114], exhibit according to figure 4.3 c) an apparent height of 1.4 Å. It should be mentioned that they are still visible by STM within the NaCl layer.

In figure 4.3 d) series of consecutive STM images of one NaCl island adsorbed within a terrace are shown. Upon scanning with a tunneling resistance of about 10 GΩ, the entire island rotates under the tip action around an Ar pinning center, in contrast to NaCl islands pinned to step edges that remains always stable at 4.8 K independent to scanning conditions. As is, these islands exhibit similar characteristics to conventional metals [41,232,238] and are thus likely adequate for the electronic decoupling of single atoms or molecules from the superconducting Pb(111).

4.3 Adsorption and manipulation of Fe atoms on Pb(111)

In this section the deposition of Fe on a Pb(111) surface is reported. First, the adsorption is described in general, which includes a differentiation between monomers, dimers and trimers. Then, the controlled lateral manipulation of single Fe atoms with the STM tip is shown.

After the evaporation of Fe on the clean Pb(111) sample, which is kept in the opened LT microscope below 15 K (see subsection 2.1.2), several circular shaped protrusions of different sizes and heights can be observed by STM imaging (see figure 4.4 a). The diameter of these protrusions varies from 0.3 up to 1.5 nm, whereas their apparent heights exhibit values of 0.4, 1.2 and 1.7 Å. Although no atomic resolution of these aggregates have been obtained, their variation of heights is interpreted in the following as fingerprint for a Fe monomer, dimer and trimer, respectively (denoted as Fe_1, Fe_2 and Fe_3).

To confirm this assumption, single Fe adatoms were laterally manipulated with the STM tip to intentionally form dimers and trimers and measure their apparent STM heights. This process followed a description by Saw-Wai Hla *et al.* [249,250]. To do so, the STM tip was first positioned above a single Fe atom. The resistance of the STM junction was then decreased from ≈ 50 GΩ (imaging) to 3 GΩ (manipulation) in order to trap the Fe atom in the STM junction [251]. Upon lateral displacements of the tip with a velocity of about 500 pm/s, the trapped Fe atoms is pushed/pulled over the surface.

During this process, a so-called "atom manipulation image" [175] has been obtained, which illustrates such dragging of the Fe atom over Pb(111) (see figure 4.4 b). The geometric features of this image resemble typical patterns, observed in friction force measurements [169,170], since they share by the trajectory of atoms over the surface potential the same origin. For clarity, in figure 4.4 c) the Pb(111) surface lattice has been overlaid on top of the image. Between the darkest features a distance of 3.5 Å can be measured, which is in agreement with the lattice parameters of Pb(111) (see figure 2.6) and likely corresponds to its hollow sites, where the adatom preferentially is located.

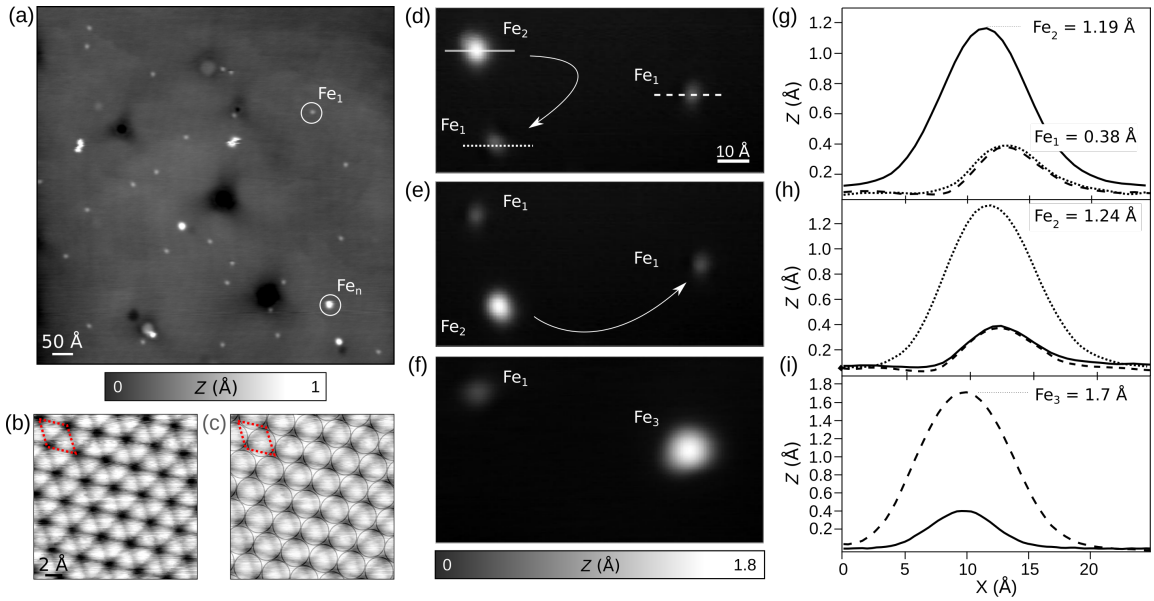

Figure 4.4: ***Fe adatoms on Pb(111) and their lateral manipulations.*** ***(a)*** *STM overview image of Pb(111) after deposition of Fe adatoms (V_t = -700 mV, I_t = 5 pA). Fe_1 and Fe_n correspond to single Fe adatom and clusters of n adatoms, respectively (V_t = -15 mV, I_t = 5 pA).* ***(b)*** *Topographic STM image during the manipulation of single Fe atoms, trapped in the STM junction.* ***(c)*** *Models of the Pb(111) lattice, corresponding to the STM image of (b). The red dashed parallelogram refers to the Pb(111) lattice.* ***(d-f)*** *Series of STM images of Fe adatoms and their successive lateral manipulations with the STM tip (marked by arrows in (d) and (e)). In (f), the STM image shows the formation of a Fe-trimer Fe_3 by successive tip manipulations (Imaging conditions, V_t = -30 mV, I_t = 60 pA).* ***(g-i)*** *Apparent STM heights extracted from images (d-f) enabling one to distinguish from their topographic signatures Fe_1, Fe_2 and Fe_3, respectively.*

The application of this method allowed it to transfer single Fe aggregates over the Pb(111) surface to other Fe aggregates. In figure 4.4 d), two single atoms (Fe_1) and an assumed dimer (Fe_2) are displayed. Figure 4.4 g) shows the corresponding apparent STM heights extracted from the plain, dotted and dashed lines of figure 4.4 d). Thus, the heights of Fe_1 and Fe_2 aggregates are inferred to be approximately $h_1 = 0.4$ Å and $h_2 = 1.2$ Å, respectively.

As a verification of these heights, then the transfer of a single Fe atom (marked by the arrow in figure 4.4 d) was conducted from the Fe_2 cluster to one surrounding Fe_1, in order to form a new dimer. The result of this first manipulation step is shown in figure 4.4 e). After the exchange of the Fe atom by tip manipulation, the apparent height in the STM-measurement indicates identical values for Fe_1 and Fe_2, but on different locations, as illustrated by the height profile in figure 4.4 h). Thus, the manipulation of an Fe monomer on Pb(111) is proven with STM.

Finally, by two successive tip manipulations the atoms of Fe_2 in Figure 4.4 e) were brought to a third single Fe atom (see arrow). The STM image after this manipulations reveals the formation of a Fe-trimer Fe_3 (see figure 4.4 f). Compared to the heights of Fe_1 and Fe_2, the Fe_3 height is approximately $h_3 = 1.7$ Å. This evolution of STM apparent heights as a function of number of atoms in small Fe clusters is in good agreement with a similar study of Fe clusters on Cu(111) [252].

4.4 Summary

In this chapter it is shown that CO molecules on Pb(111) are hardly visible in STM images due to their high diffusion induced by the tip even at low temperature. However there presence can be detected by their enhancement of the resolution in STM. On the other hand, in Pb(110) they can be displayed by STM-images, which is a hint that their occurrence between the atomic rows of the (110) lattice is more stable.

Furthermore, the growth of NaCl islands could be observed in STM. They appear close to step edges of the Pb surface or use the interaction of trapped Ar atoms in the subsurface layers as pinning center.

Finally, the adsorption of single Fe aggregates has been shown. Regarding to their apparent height in STM they could be identified as Fe-monomers, Fe-dimers or Fe-trimers. This identification has been proved by a tip-induced displacement of these adsorbates on the Pb(111) surface.

The results can be seen as an important step for future experiments to perform high-resolution STM/AFM imaging with CO-terminated tips, to decouple atoms and molecules electronically from the prototypical Pb(111) surface, or to manipulate them over the surface. This is of great importance with regard to the creation of atomic Fe chains on superconducting Pb surfaces and the detection of MBS states, since various studies make this system to one of the most promising platforms for their realization.

5

Charge state control of molecular quantum dots on Pb

The requested application of molecular transistors presupposes the possibility of creating devices that can localize charge carriers and exhibit certain energy levels, occupied by single electrons. To fulfill this, a decoupling between molecular layer and metal surface is necessary. With the prospect of implementing single charges for electronic devices, recent experiments have indeed shown the feasibility for periodic charging at the edges and within self-assembled molecular layers on metals (see subsection 3.2.4).

This chapter reports on the adsorption of self-assembled monolayers of 4,5,9,10-tetrabromopyrimido[4,5,6-gh]perimidine (short: TBPP, $C_{12}H_2Br_4N_4$, see subsection 2.4), on a superconducting Pb(111) substrate. Using SPM methods, the arrangement of TBPP molecules is observed with atomic resolution. By measuring conductance maps (dI/dV), a tip induced electron transfer is investigated above single molecules of this layer. Here, the occurrence of Coulomb rings is seen as typical experimental signature for a charging or discharging event (see subsection 3.2.3).

Hence, in section 5.1 the molecular arrangement of the TBPP molecule on Pb(111) after adsorption and self-assembly is described in details. This includes not only high-resolution STM and AFM images, but also the derivation of an arrangement model in accordance with the SPM images. Furthermore, the influence of different measurement conditions on the imaging is verified by changing the applied bias voltage. In section 5.2 the occurrence of Coulomb rings in dI/dV-maps is investigated depending on the tip-induced bias voltages and different tip-sample distances. Finally, in section 5.3 these investigations are also performed in respect to the observation of a frequency shift (Δf).

5.1 Self-assembled layers of TBPP on Pb(111)

In this section the molecular structure of self-assembled TBPP layers on Pb(111) is shown in detail by STM- and AFM-measurements (see subsection 5.1.1). Furthermore, the influence of different bias voltages on that layers is investigated by evaluating STM-images (see subsection 5.1.2).

5.1.1 Structure determination of TBPP/Pb(111) by STM & AFM

After sublimating TBPP molecules at room temperature onto a Pb(111) surface (see section 2.4), self-assembled molecular islands of TBPP are observable in STM measurements. Due to their row-like structure they are clearly distinguishable from the metal Pb(111) surface (see figure 5.1 a). The molecular islands exhibit a row-like arrangement, whose alignment differ in various rotational angles. These angles are integer multiples of 60° and can be explained by the 3-fold rotational symmetry of the Pb(111) surface. The apparent height of a TBPP layer in STM amounts always to ≈ 1.2 Å, which refers to a coverage of 1 ML.

However, the exact model, how single molecules are arranged in this phase can not be deducted from figure 5.1 a) and a higher resolution is necessary. In figure 5.1 b) a detailed STM image of the TBPP layer with higher magnification than in figure a) is shown. Here, the row-like structure becomes more evident, but it is still not possible to assign the features in the STM image to individual components of the TBPP molecule. Noticeable are white dot-like structures, which are characteristic for the regular rows. They form a unit cell with the dimensions of $a = 9.8$ Å within the rows, $b = 15.4$ Å between the rows and an angle of $\theta = 85°$ (see red arrows). In accordance with the structural formula of the molecule, they correspond probably with the Br atoms at the ends, as these protrude from the basic structure of the molecule and, moreover, Br has a very high electronegativity.

Only by applying AFM, an atomic resolution of the TBPP layer can be achieved (see figure 5.1 c). Particularly noticeable is here a structure made up of two point-like features, which have a lower Δf than other features and therefore appear white in AFM. They occur either side by side (in a row of four points) or offset from one another in pairs. In comparison to the structural model of the TBPP molecule, it is advisable to interpret them as the Br atoms, since they are expected to be present as pairs at each side of the molecule.

In figure 5.1 d) structural models of the TBPP molecule are superimposed to the AFM image. It indicates that the TBPP molecules are arranged in two rows, which either exhibit a straight sequence of molecules (S) or a tilted arrangement (T). Hereby, the molecules in S-rows are arranged consecutively with a small lateral shift of ≈ 1 Å. The molecules in T-rows are shifted in such a way that the Br atoms at the end of a molecule are in one line with the Br atoms of the neighboring molecules. The molecular arrangement in T-rows is rotated by approx 50° compared to that in the S-rows.

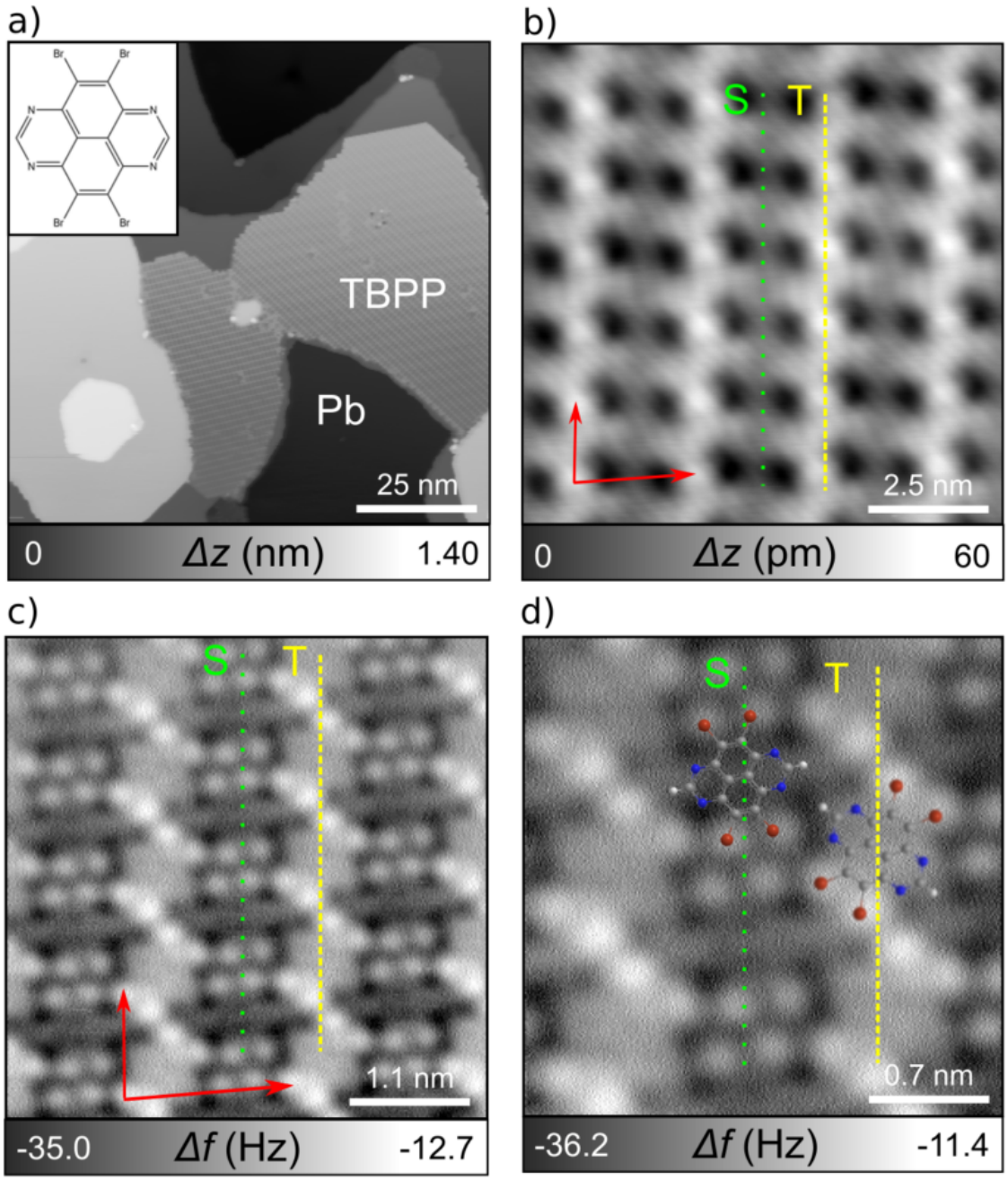

Figure 5.1: Structure of molecular arrangement. *For images (b)-(d) the straight (S) and tilted (T) molecular assembly is marked with a line. The unit cell of the TBPP layer is marked with red arrows.* ***(a)*** *STM overview image of Pb(111) after deposition of TBPP molecules (V_s = 1.0 V, I_t = 1 pA, inset: molecular structure of TBPP).* ***(b)*** *Detailed STM image of molecular TBPP layer (V_s = 0.7 V, I_t = 0.8 pA).* ***(c)*** *AFM image of molecular TBPP layers, showing rows with two different orientations.* ***(d)*** *Detailed AFM image of molecular TBPP layers, showing the molecular arrangement of straight (S) and tilted (T) assembly (model of TBPP is superimposed).*

The AFM-image in figure 5.1 d) also shows a slight contrast between the S and T rows: The molecules in S-rows appear with more negative frequency shift indicating a larger distance to the tip. In contrast to that, the molecules in T-rows appear with bright contrast and moreover, the shape of the benzene and pyrimidine rings differs stronger from the background. Thus, the TBPP layer seems to be slightly folded between S- and T-rows. Transferring this result to the STM measurement shown in figure 5.1 b), this means, that most likely the Br atoms of the T-rows can be considered as the cause of the point-like features.

5.1.2 Influence of bias voltage on TBPP/Pb(111)

Principally, the model deducted from AFM images in figure 5.1 d) helps for the interpretation of further STM measurements. Hence, for a selected surface area a sequence of STM measurements at sample bias voltages V_s between 5 mV and 1.0 V (see figure 5.2) has been taken compared to the results from AFM.

At low V_s of 5-10 mV (see figure 5.2 a+b), the orbitals of individual components of the TBPP molecule can be resolved by STM. Here, the TBPP molecules in an S-arrangement appear much brighter than those in the T-arrangement, which is in contrast to the AFM measurements. The pairs of Br atoms exhibit in the S-rows a weaker apparent height than eight other dot-like features, which can be interpreted as signature of the 4 N atoms and further C atoms (most likely from the ones bond to the Br). In the T-rows only four features are clearly observable, which can be assigned to the Br-atoms.

At $V_s = 40$ mV (see figure 5.2 c), the S- and T-rows appear with similar contrast and in both rows the dominating features are in the same position as the Br atoms in figure 5.1 d). Still, within the S-rows, the orbitals representing C- and N-atoms can be observed, but much weaker as for lower bias voltages. For the T-rows, this part of the molecule appears only as one smeared cloud of electron density.

For $V_s \geq 100$ mV (see figure 5.2 d+e), the TBPP molecules in the T-arrangement appear clearly brighter than the ones in S-rows. This can be almost exclusively ascribed to the four Br atoms, which appear in AFM in a row. For a bias of 400 mV (see figure 5.2 e), they can no longer be distinguished from each other, but merge all into a kind of dot-like charge clouds, whose distances have been used to characterize the unit cell illustrated in figure 5.1 b).

At $V_s = 1.0$ V (see figure 5.2 f), the dots of the T-rows seem to merge with each other and form a zig-zag structure, resembling the former sequence of tilted TBPP-molecules. However, here, the S-rows exhibit a dramatic contrast to the other measurements at lower bias voltages: Round-shaped clouds of electron density appear along each S-row and their center seems to be in the middle of every TBPP molecule (cf. model structure in figure 5.2 g).

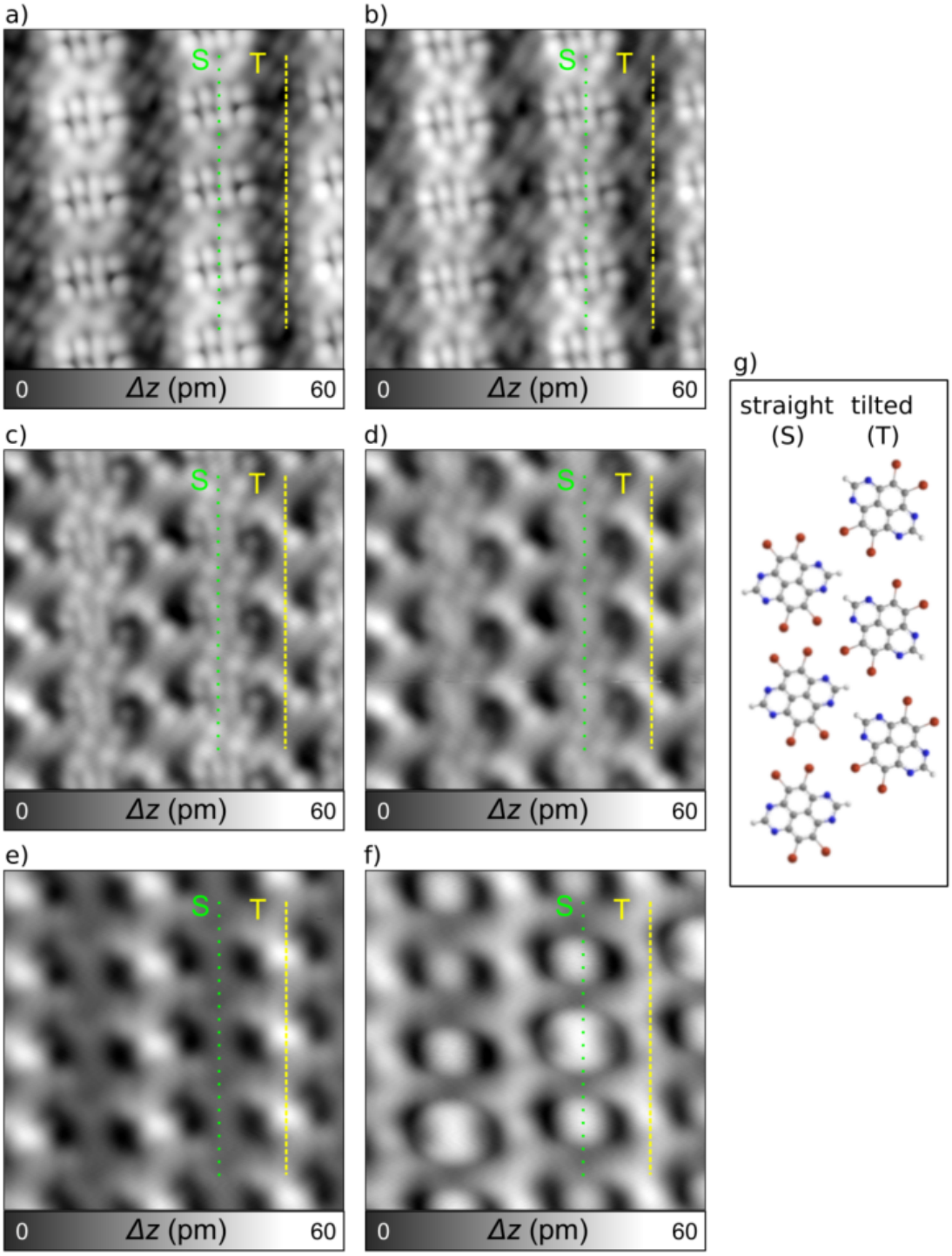

Figure 5.2: Serie of STM-measurements on TBPP. *Sample bias voltages V_s are between 5 mV and 1.0 V (Size: 4 nm × 4 nm, I_t = 0.8 pA). For all images the straight (S) and tilted (T) molecular assembly is marked with a line:* ***(a)*** *V_s = 5 mV.* ***(b)*** *V_s = 10 mV.* ***(c)*** *V_s = 40 mV.* ***(d)*** *V_s = 100 mV* ***(e)*** *V_s = 400 mV* ***(f)*** *V_s = 1.0 V* ***(g)*** *Model of the molecular TBPP arrangement.*

The electron density clouds in figure 5.2 f) display different strengths and a certain gradation within individual S-rows, similar to the one reported by Isabel Fernández-Torrente *et al.* for monolayers of two different molecules [27]. At the same time, there is also an interaction with neighboring rows, since the shape of the charge ring is repeated synchronously in the neighboring S-row with a shift by one molecule position. In accordance with the literature [27–30], this bias dependent appearance of features, related to confined charges, is a hint for the behavior of a molecular QD.

5.2 Arrays of Coulomb rings in molecular TBPP layers

According to the emergence of hints for an electron transfer in figure 5.2 f), the following investigations deal with the appearance and the shape of Coulomb rings as typical characteristic for single-electron transfer. In subsection 5.2.1, STM measurements are carried out for sample bias voltages V_s in a small interval above and below 1.0 V in order to examine this behavior in more detail. Similar measurements have also been performed for negative V_s, but no electron transfer was observable. Analogous to the results of Fernández-Torrente *et al.* [27], the measurements are carried out for different molecular rows of the TBPP layer in order to check, whether individual molecular rows differ in their charge state. In subsection 5.2.2, these measurements are continued by varying the tip-sample distances up to 140 pm. Finally, in subsection 5.2.3 the correlation between charge transfer and tip position is characterized.

5.2.1 Influence of bias voltage on Coulomb rings

To investigate the characteristics and lateral distribution of the charging behavior, dI/dV-maps for V_s between 0.85 V and 1.30 V were carried out on a larger scale of 30×30 nm^2 (see figure 5.3 a-d). For $V_s = 0.85$ V only a few Coulomb rings are observable, which are irregularly distributed on the surface and differ significantly in their characteristics (see figure 5.3 a). All of them have their center above the S-rows. Slight contrast differences in the TBPP layer indicate possible defects.

At $V_s = 1.0$ V (see figure 5.3 b), the Coulomb rings appear on the entire TBPP layer. They exhibit within the molecular S-rows a periodic array of Coulomb rings. This array is aligned along certain axes (marked in red) that are rotated by 55° in respect of the S- and T-rows. The higher conductance above single molecules along these axes varies and affects every 4th or 5th molecule in the S-rows. The mean distance of the red axes within the S-row amounts to 4.1 nm, which corresponds to 4.24 times the molecular distance $a = 9.8$ Å. Therefore, the origin for the graduation is not entirely commensurate with the molecular lattice of the TBPP layer.

By increasing to $V_s = 1.15$ V (see figure 5.3 c), more Coulomb rings appear and the radius of the rings described before increases significantly. At $V_s = 1.30$ V (see figure 5.3 d) they start to overlap each other, but the periodicity along the rows is not affected by this.

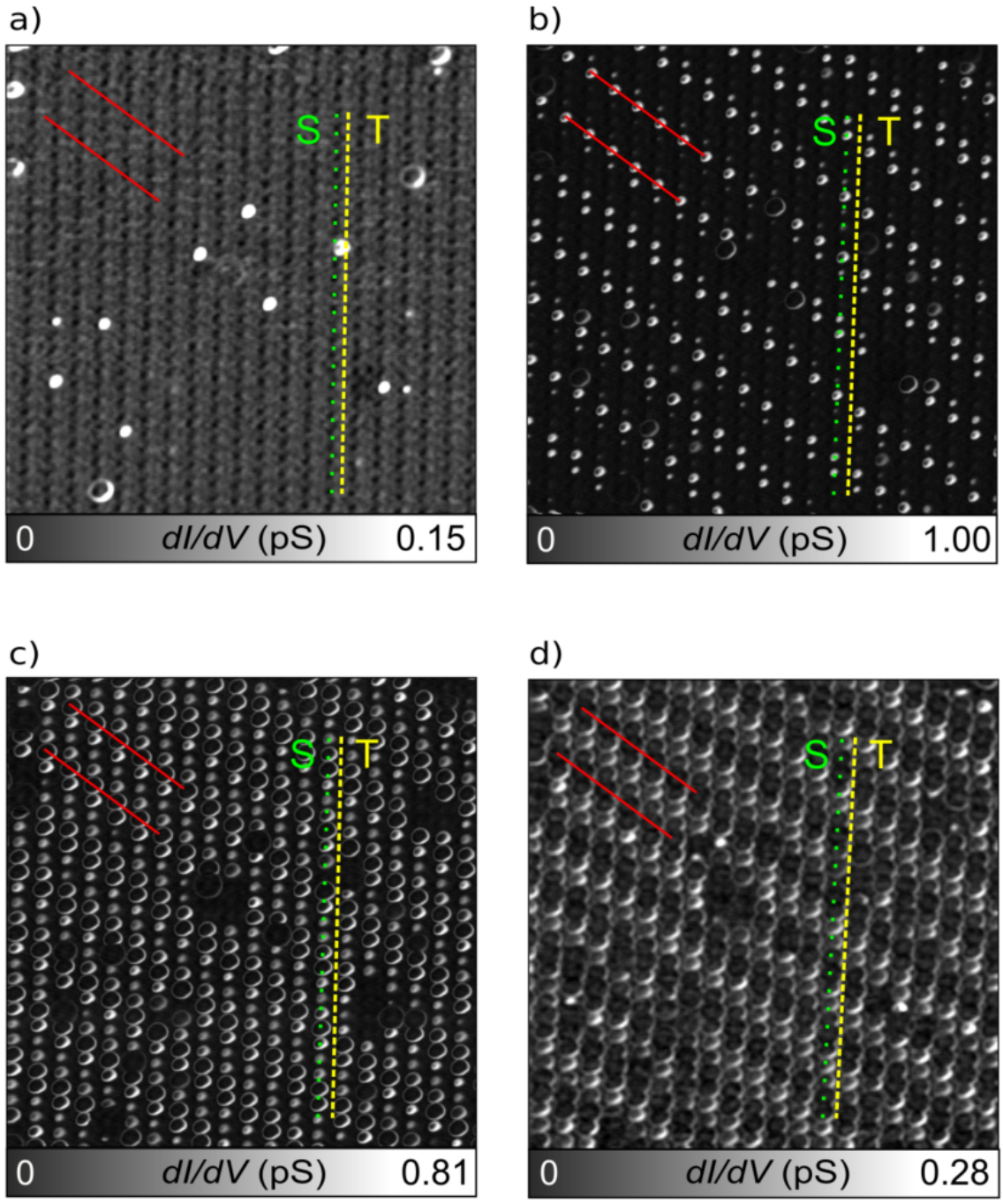

Figure 5.3: dI/dV**-measurements on TBPP for various voltages.** ***a-d:*** *Serie of* dI/dV*-measurements on TBPP for sample voltages* V_s *between 0.85 V and 1.3 V (Size: 30 nm* $\times$ *30 nm,* I_t *= 0.8 pA). For all images the straight (S) and tilted (T) molecular assembly is marked with dashed lines. The axes, along which Coulomb rings appear strongest, are marked by red lines.* ***a:*** V_s *= 0.85 V.* ***b:*** V_s *= 1.00 V.* ***c:*** V_s *= 1.15 V.* ***d:*** V_s *= 1.30 V.*

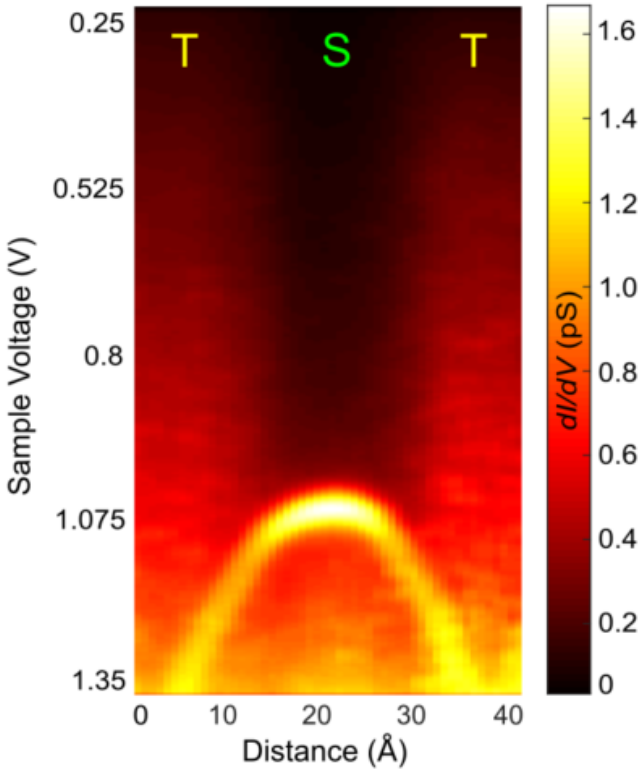

Figure 5.4: Cross section $dI/dV(V_s, x)$ on TBPP layer versus sample voltage along a length $x = 40$ Å. *The position of the straight (S) and tilted (T) rows of the TBPP layer are marked with letters.*

A continuous change of the radius can be shown with the help of a $dI/dV(V_s, x)$ cross section depending of V_s and the lateral distance x (see figure 5.4). It indicates a threshold voltage for any charging event at $V_s \approx 1.0$ V. The radius of the Coulomb rings increases for higher V_s until it is ≈ 15 Å for voltages of 1.35 V. The higher conductance for T-rows in the range of 0.4-1.0 V is in accordance with figure 5.2.

The increasing radius for higher V_s is analogous to the observations of Fernández-Torrente *et al.* (see section 3.2.4) [27]. There, it has been related to the increasing tip-sample distance, which causes a lower electric field on the molecule. According to subsection 3.2.3, this mechanism influences the shift of the molecular energy levels and thus the emergence of the Coulomb rings, which represent the electron transfer betweeen tip and molecule. The threshold marks the sample voltage V_s, which is needed to shift the occupied state above the chemical potential of the surface μ_S. Only when the energy level of the state crosses μ_S, an electron can be locally removed or added by the electrical field of the tip.

The quantitative amount of this shift can be identified by the double barrier tunneling junction (DBTJ) model [24]. Here, the shift ΔE can be expressed as $\Delta E = e\alpha V_s$ [23], where e is the elementary charge, α the so-called lever arm [28], depending on the

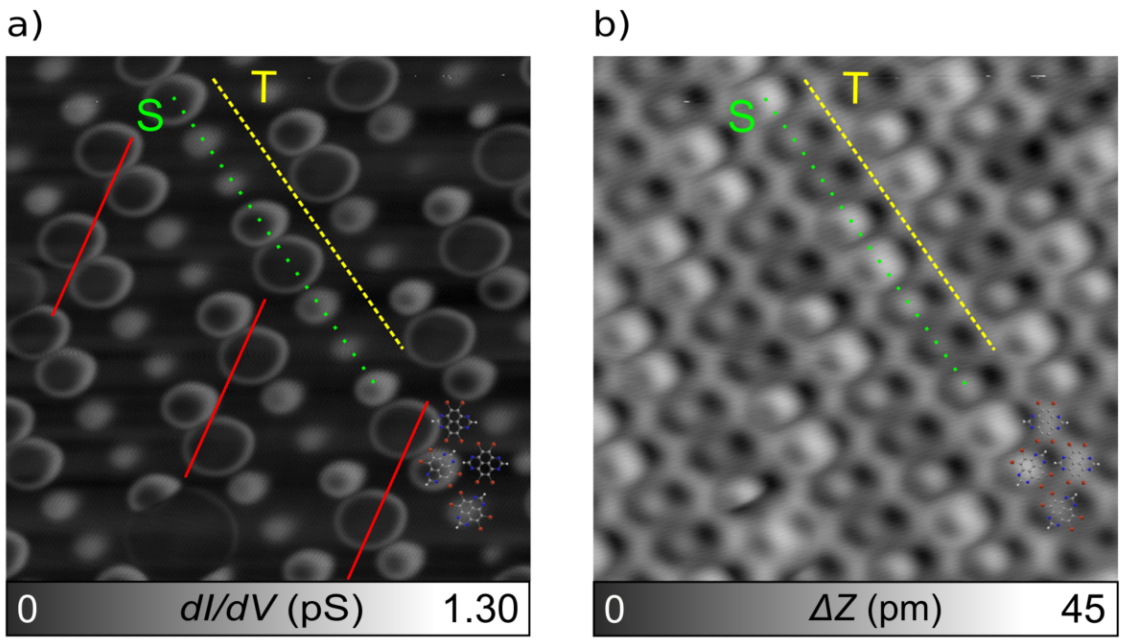

Figure 5.5: Graduation along the Coulomb rings. ***(a)*** *dI/dV and* ***(b)*** *STM-image (Size: 10 nm × 10 nm, V_s = 1.3 V, I_t = 5 pA). For both images the straight (S) and tilted (T) molecular assembly is marked with a line. The axes, along which Coulomb rings appear strongest, are marked by red lines.*

tip-sample distance z and V_s the applied sample bias voltage. In accordance with Fernández-Torrente *et al.* [27], the positive dI/dV refers to a local increase of the tunneling current and thus to a local discharging event.

Hence, the superstructure of the Coulomb rings is the result of periodic variations in the tip-induced shift of the energy levels, which have its origin in interactions between molecular layer and metal substrate. This strong dependence of the discharging events on the lateral position is illustrated in figure 5.5 a), which provides a dI/dV map with a detailed view on the gradation of the Coulomb rings within a row. Here, a sample bias of V_s = 1.3 V has been chosen analogously to figure 5.3 d), but due to the different lateral position the radius of the rings is significantly smaller. Nevertheless, the graduation within the S-rows shows similar irregularities. This asynchronicity within the graduation of the rings, clearly indicates that the axes of the superstructure (marked red) are to be found between single molecules. In figure 5.5 b) the simultaneously measured STM image corresponds to the dI/dV-map, but shows the differences in graduation less clearly. Recent measurements of molecular QDs on oxygen-intercalated graphene on Ir(111) attribute this lateral dependence to Peierls instabilities at low temperatures [253].

To qualify the charge transfer as charging or discharging, dI/dV-spectra for positive and negative V_s have to be measured. While on the T-rows no peak or dip, indicating a charge transfer event, is observable, dI/dV-spectra on the S-rows only exhibit the

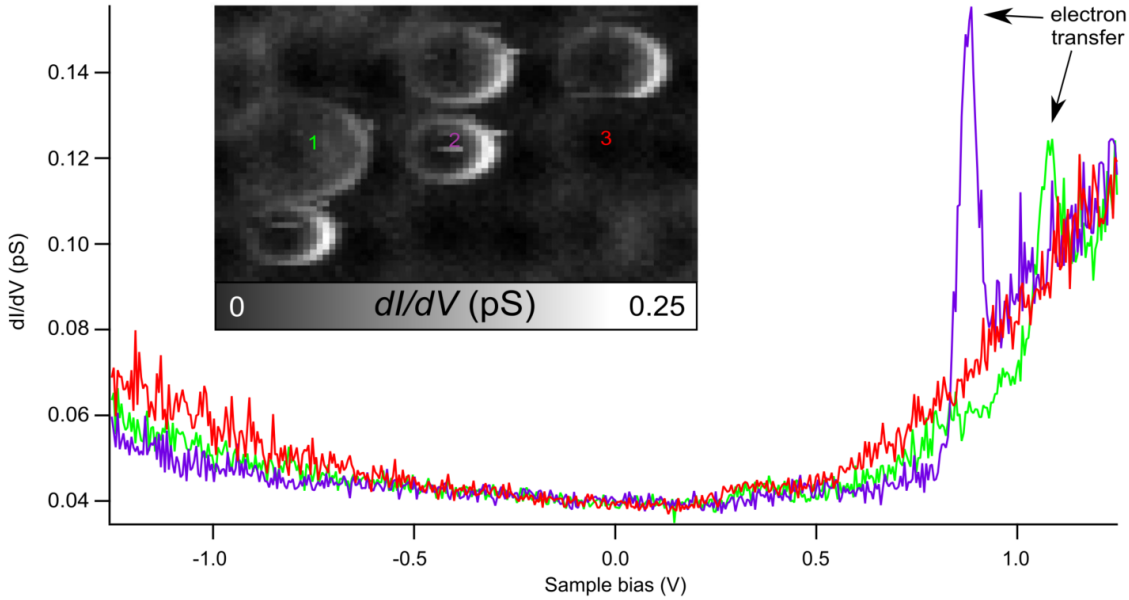

Figure 5.6: Full dI/dV-spectra at different locations within the Coulomb rings *(locations marked in dI/dV-map, size: 4.5 nm × 3.0 nm, V_s = 1.15 V, I_t = 1 pA).*

mentioned peak for positive V_s. In figure 5.6 dI/dV-spectra for three lateral positions along S-rows are shown. According to a dI/dV-measurement at $V_s = 1.15$ V (see inset) they are located within a Coulomb ring of large radius (red), small radius (purple) and without any ring. At each place, the spectrum was measured for V_s between -1.25 V and +1.25 V.

In conclusion, discharging events on S-rows for positive V_s are observed. Assuming an anionic ground state for the S-rows of the TBPP layer, which could be deduced to an electron-acceptor behavior, the tip influences the removal of an electron and creates a neutral state. More detailed results on the origin of the anionic state of the molecules in S-series could obtained from DFT simulations.

5.2.2 Influence of tip-sample distance on Coulomb rings

To investigate the dependence of the discharging events, further measurements independent from lateral fluctuations within the TBPP layer are performed. According to the DBTJ model, the interaction between tip and QD can be described as capacitor with the capacitance C_T. Therefore, the relationship between the position of the discharging peak depending on various z-offset has to be discovered. In the following, a fixed lateral position is selected and the dI/dV-spectra are measured depending on different tip-sample distances z.

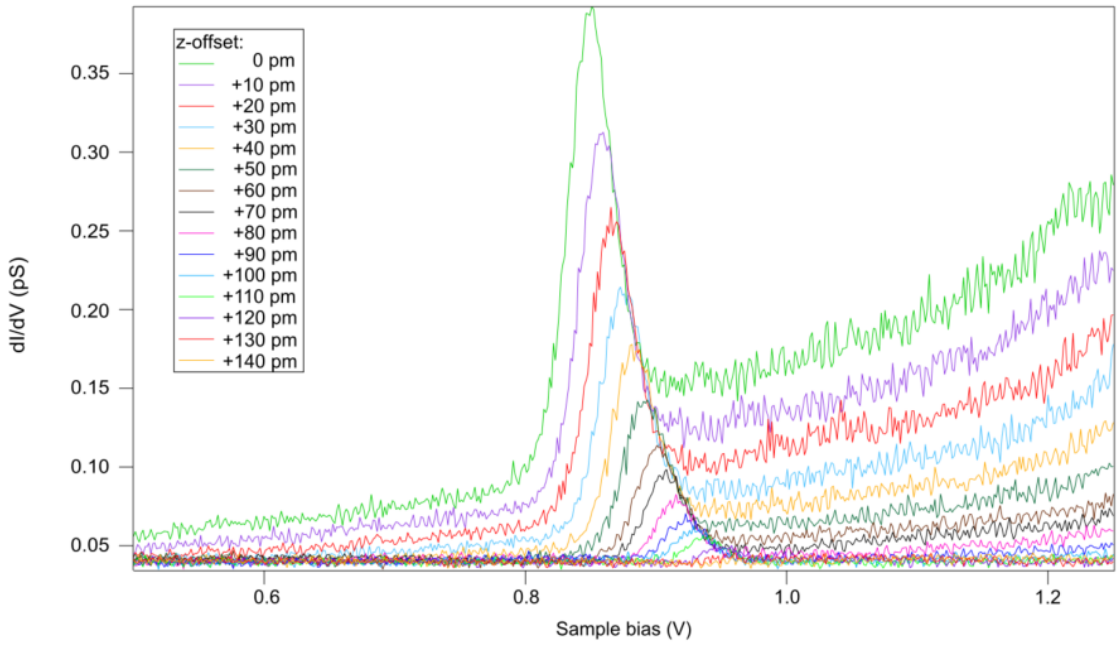

Figure 5.7: Series of dI/dV spectra *(raw data) for an exemplary selected position with a variation of the tip-sample distance z by offsets between 0 and 140 pm.*

Figure 5.7 shows $dI/dV(z)$-spectra of Coulomb rings at a fixed lateral position above an TBPP molecule for varied tip-sample separations z of up to 140 pm. Each peak represents the discharging event and shifts for increasing z to higher bias voltages. The magnitude of the conductance peaks decreases with higher tip-sample distances, which can be explained by the larger tunneling barrier between tip and molecule.

To determine the exact position of the maxima, the background of the spectra has to be removed. For this reason, a fit of the background had to be developed to subtract it afterwards from the raw data. To do so, first the data points at the position of the peak were removed from the spectra and the remaining points fitted with an polynomial of eighth order (see figure 5.8).

In the next step, this background was subtracted from the raw data and thus the peak became separated (see figure 5.9). The individual spectra are fitted by Gaussian curves and the positions of the individual maxima are determined.

In figure 5.10 the voltages of the dI/dV-peaks are plotted versus the increase of the tip-sample separation Δz. It exhibits a proportional relationship, which refers to the voltage of a plate capacitor, which depends similarly on the distance of the plates. Approximating these data with a linear fitting line shows a very good agreement. Only the maximum from the curve for 140 pm offset had to be removed, since its intensity was already too small for a reasonable fit.

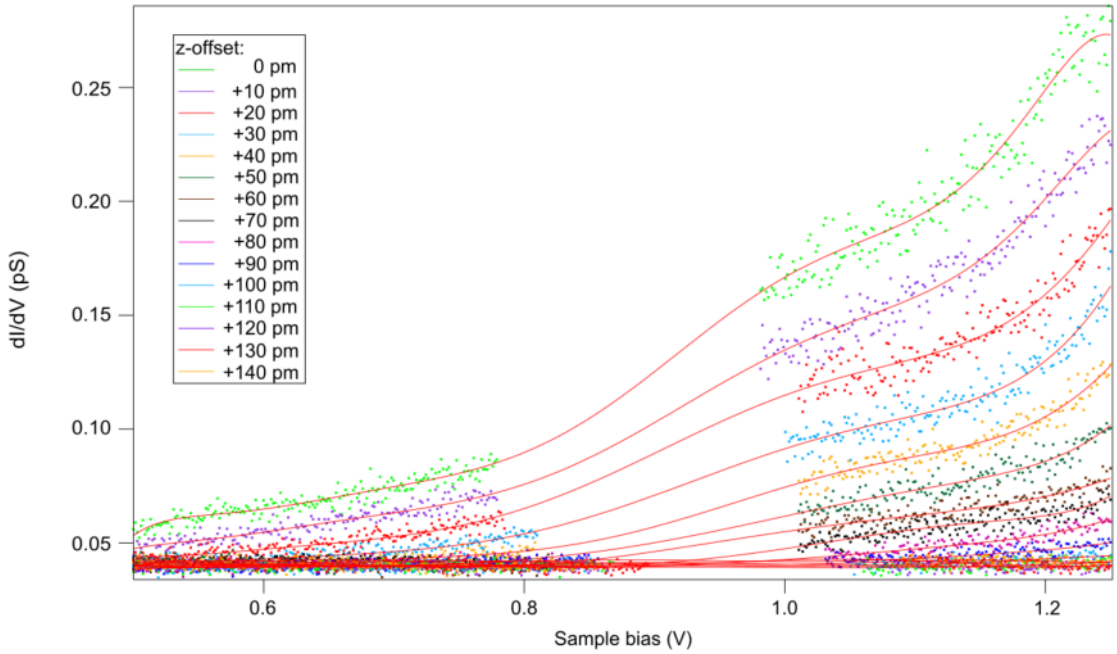

Figure 5.8: Series of dI/dV spectra *(raw data and polynomial fitting curve of eighth order) with a variation of the tip-sample distance z by offsets between 0 and 140 pm. The peaks of each curve have been removed.*

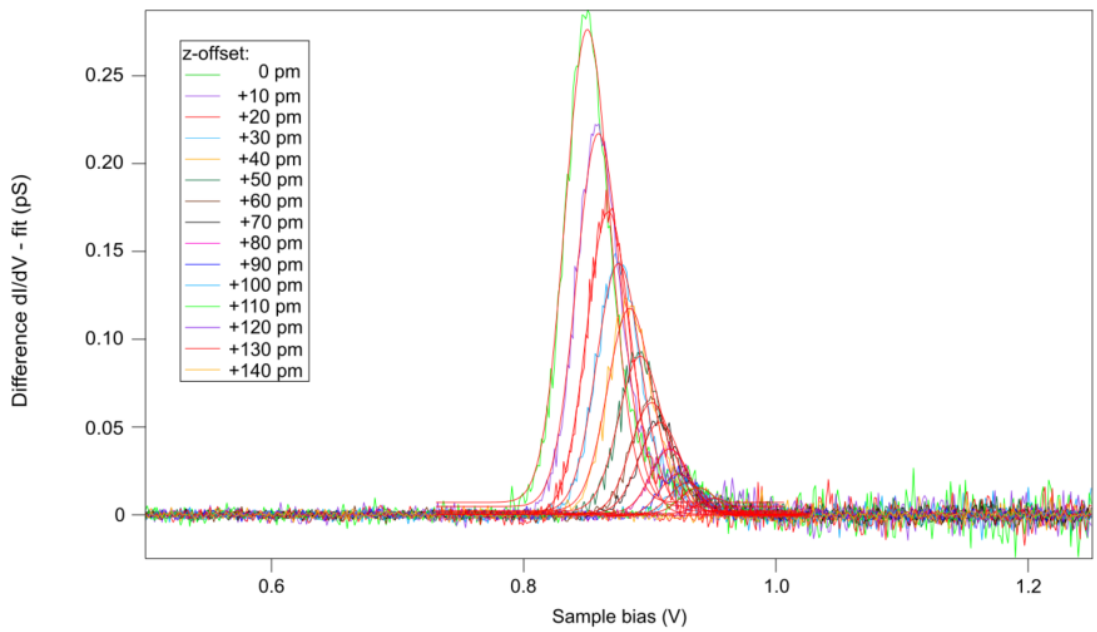

Figure 5.9: Series of dI/dV spectra *with a variation of the tip-sample distance z by offsets between 0 and 140 pm. The background from figure 5.8 has been removed to illustrate only the maximum caused by electron transfers.*

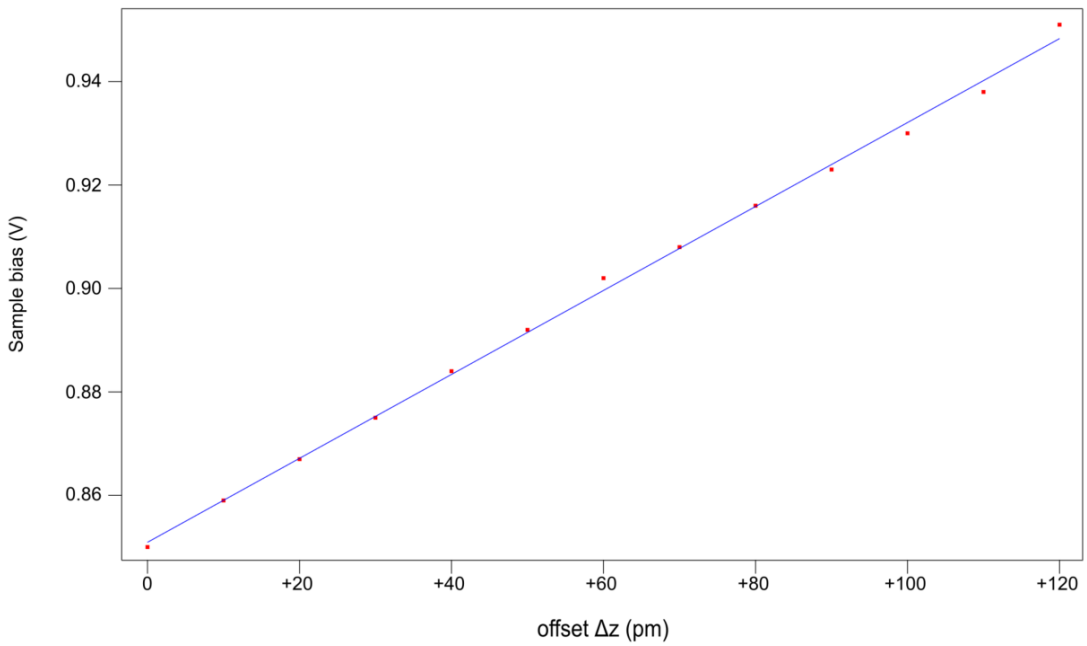

Figure 5.10: Maxima of the dI/dV spectra illustrated in figure 5.9 with a z variation of Δz = 0-120 pm

5.2.3 Distance dependence of the charge transfer based on dI/dV

To characterize the distance dependence of the charge transfer, shown in figure 5.10, one can assume a simple plate capacitor with the permittivity ϵ, plate area A and distance d.

$$C_T = \varepsilon \frac{A}{d} \tag{5.1}$$

With the help of $Q = C \cdot U$ and $d = z + \Delta z$, where Δz is the additional offset, one can get from equation 5.1:

$$U(\Delta z) = \frac{Q}{A \cdot \varepsilon} \cdot d = \frac{Qz}{A \cdot \varepsilon} + \frac{Q}{A \cdot \varepsilon} \cdot \Delta z \tag{5.2}$$

Equation 5.2 represents the linear correlation shown in figure 5.10. The term $i = \frac{Qz}{A \cdot \varepsilon}$ denotes the intercept and $s = \frac{Q}{A \cdot \varepsilon}$ the slope of the line. From the fit line it follows $i = (0.85092 \pm 0.000785)$ V and $s = (8.1154 \cdot 10^8 \pm 1.11 \cdot 10^7) \frac{\mathrm{V}}{\mathrm{pm}}$. According to this, the tip-sample distance z for the starting position ($\Delta z = 0$, $V_S = 1$ V and $I_t = 1$ pA) can be calculated as:

$$z = \frac{i}{s} = \frac{(0.85092 \pm 0.000785)\ \mathrm{V}}{(8.1154 \cdot 10^8 \pm 1.11 \cdot 10^7) \frac{\mathrm{V}}{\mathrm{pm}}} = (1.05 \pm 0.01)\ \mathrm{nm} \tag{5.3}$$

This result can only be interpreted as an approximation, since it is questionable whether the linear behavior can also be transferred for small z [29]. In addition, the assumption of the tip and the molecule as a plate of the same area A is unrealistic.

5.3 Frequency shift due to Coulomb rings

Single electron charge transfer can also be demonstrated by the frequency shift Δf in AFM measurements [25, 28–30, 187–189, 206]. The contrast of AFM might differ drastically from STM and dI/dV. Figure 5.11 gives a first impression on this topic by comparing STM-, dI/dV- and AFM-measurements of the same surface area.

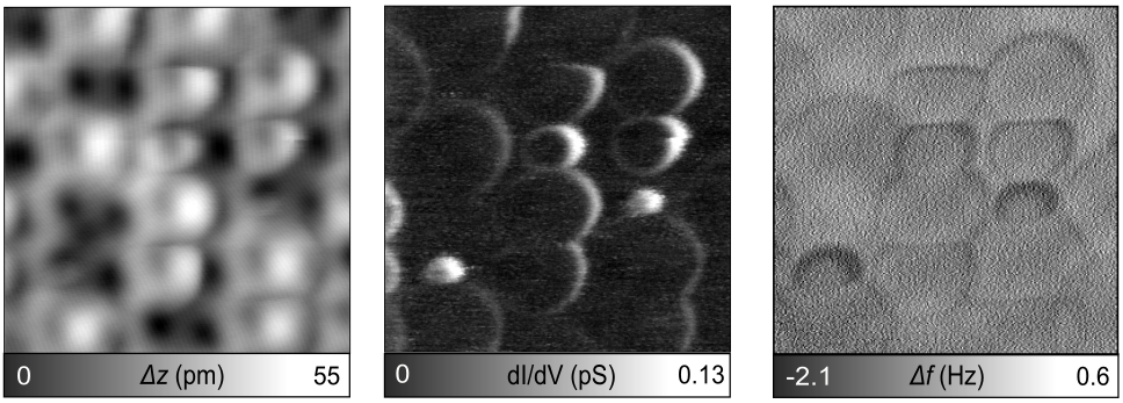

Figure 5.11: Comparison between STM, dI/dV and AFM-measurements at the same area *(Size: 5 nm × 5 nm, V_s = 1.3 V, I_t = 1 pA). (**a:**) STM, (**b:**) dI/dV and (**c:**) AFM-measurements.*

In figure 5.11 can be seen that all Coulomb rings, which are illustrated in the dI/dV image can also be observed by AFM. However, in the AFM measurement they exhibit a slightly larger radius and are characterized by a negative shift, which is why they appear as indentation. Nevertheless, this in accordance with previous reports on Coulomb rings in AFM [25, 28–30].

Further information can be obtained analogously to the dI/dV-measurements by means of Δf spectra. Hence, in this section, the relationship between tip sample distance and bias voltage is examined with the help of $\Delta f(V_s)$-spectroscopy (see subsection 5.3.1). These results are compared with the characterization from conductance measurements (see subsection 5.3.2).

5.3.1 Influence of tip-sample distance on Coulomb rings in AFM

In Figure 5.12 the raw data of Δf spectra with different z-offsets of 0-160 pm are shown. As expected from the indentation of the rings, the Coulomb oscillation, representing the discharging event, is here characterized by a dip. To fit these dips, the dips have to be separated analogously. In relation to the principle of this technique (see figure 1.8), the background has to be fitted with a parabola. After subtracting the background from the raw data, each individual dip was fitted with a Gaussian curve (see figure 5.13).

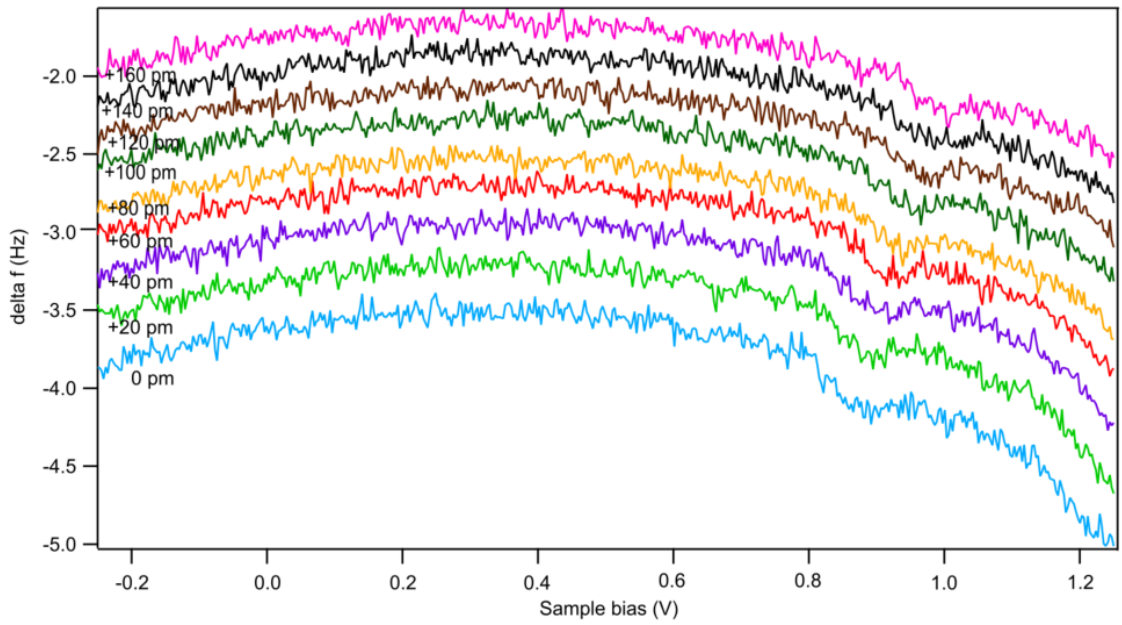

Figure 5.12: Series of Δf spectra *(raw data) for an exemplary selected position with a variation of the tip-sample distance z by offsets between 0 and 160 pm.*

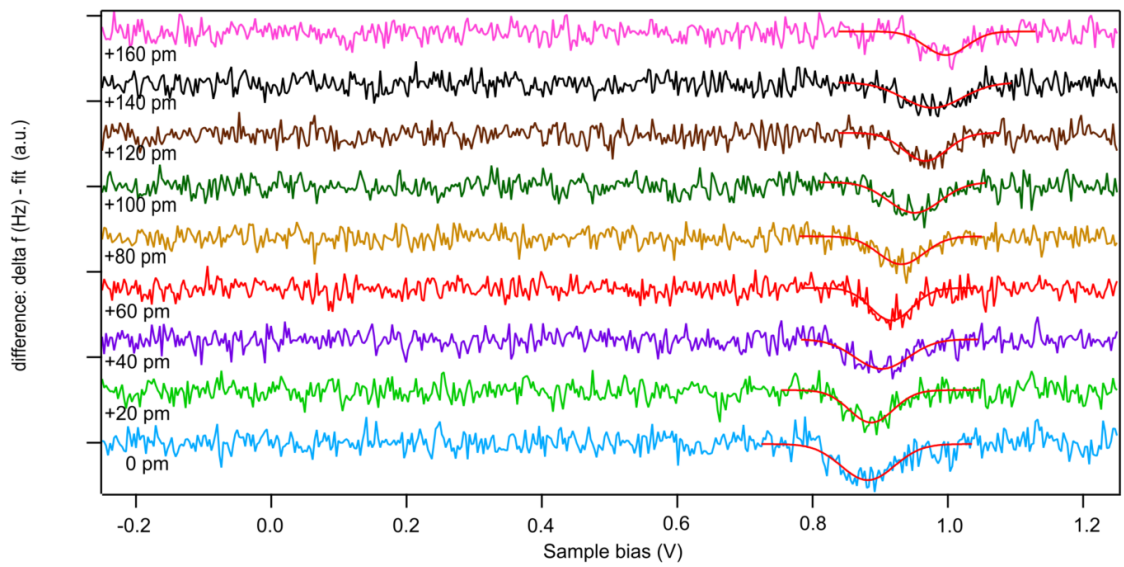

Figure 5.13: Series of Δf spectra *for an exemplary selected position with a variation of the tip-sample distance z by offsets between 0 and 160 pm. Here, the peak of the discharging event has been removed analogously to figure 5.8 and the minimum of each curve is fitted.*

After plotting the positions of these minima according to the sample bias against the z-offset again a proportional relationship is observable. Approximating the data with a linear fitting line (see figure 5.14) shows analogously to figure 5.10 a very good agreement.

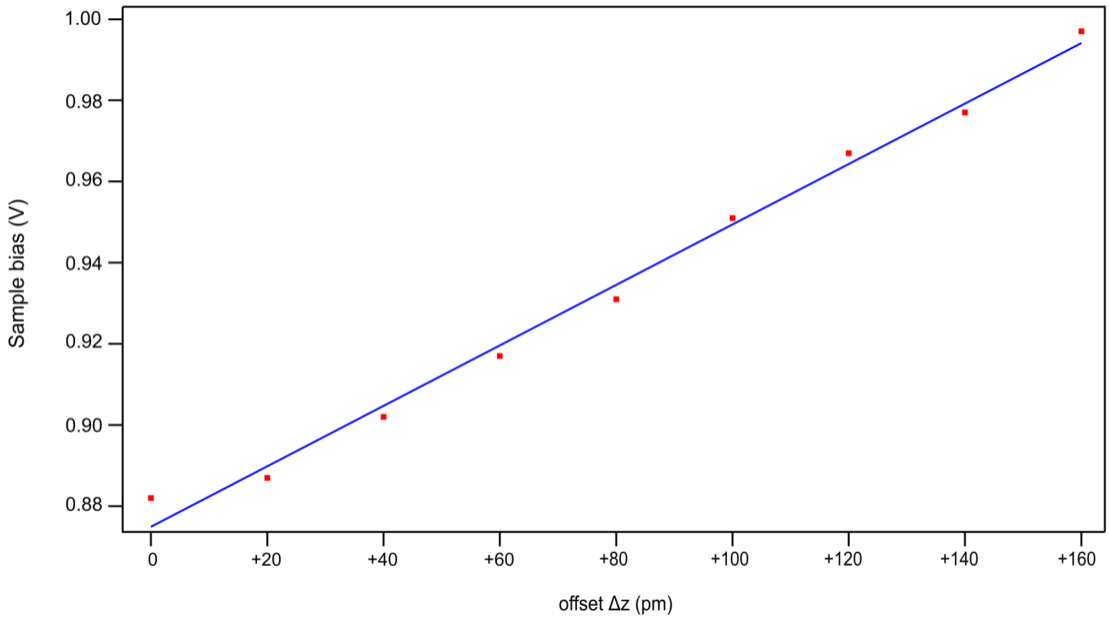

Figure 5.14: Minima of the Δf spectra illustrated in figure 5.13 with a z variation of Δz = 0-160 pm

5.3.2 Distance dependence of the charge transfer based on AFM

Analogous to subsection 5.2.3 the characterization of the distance dependence for the charge transfer can also be evaluated with Δf spectra. The fit line in figure 5.14 has an intercept of $i = (0.87496 \pm 0.00241)$ V and a slope of $s = (7.45 \cdot 10^8 \pm 2.53 \cdot 10^7)\frac{\mathrm{V}}{\mathrm{pm}}$. According to this, the tip-sample distance z for the starting position ($\Delta z = 0$, $V_S = 1$ V and $I_t = 1$ pA) can be calculated as:

$$z = \frac{i}{s} = \frac{(0.87496 \pm 0.00241)\ \mathrm{V}}{(7.45 \cdot 10^8 \pm 2.53 \cdot 10^7)\frac{\mathrm{V}}{\mathrm{pm}}} = (1.17 \pm 0.05)\ \mathrm{nm} \tag{5.4}$$

Even if here the slope deviates slightly from the result calculated in subsection 5.2.3, the linear z dependence in both, the dI/dV- and Δf-spectra confirms the good approximation of the plate capacitor model in the range of the investigated tip-sample distances. Future investigations with simulations on this system might proof, whether it can be deduced to smaller tip sample distances and thus also assess the validity of the calculated tip sample distance.

5.4 Summary

In this chapter it is shown that TBPP molecules on Pb(111) exhibit an electron transfer by the application of a sample bias voltage V_S in the range of 1 V. This is detected by the presence of Coulomb rings around single molecules in dI/dV measurements. The TBPP layer has been resolved atomically in AFM-measurements, showing two different molecular arrangements, a straight (S) and a tilted (T) row.

Due to the atomic resolution of the TBPP layer, it was possible to assign the electron transfer solely to the S-rows. Since the signature for the electron transfer in dI/dV is positive (showing a peak in the spectra), it was interpreted as a discharging event. Additionally, in the array of Coulomb rings, a periodic superstructure has been detected, which influences laterally the graduation of the Coulomb rings. It is not fully commensurate with the TBPP lattice and seems to originate from interactions between the molecular layer and the metal substrate.

Furthermore, the size of the Coulomb rings depends on V_S, which is connected to the tip-sample distance z. Below a certain threshold, no discharging event is detectable and with increasing V_S the radii of the rings widen. A similar dependence can also be observed by varying z directly and measuring the position of the discharging peak in dI/dV- and Δf-spectra.

Finally, a simple plate capacitor model is tested for the data showing the dependency on Δz. It agrees well with the measurements, but its application for lower tip-sample distances remains questionable.

All in all, the results can be seen as very promising for the development of new nanoscale devices. Possible applications are in the field of quantum computing or quantum sensing.

Conclusion

This thesis examines two fields that are relevant to the question if Pb surfaces are suitable for the realization of qubits: On the one hand the adsorption of CO, NaCl and Fe atoms, which might play a role for the tip-controlled manipulation of atomic chains, hosting Majorana bound states (MBS) and on the other hand the adsorption of 2D TBPP layers, which exhibit a signature for single-electron charging analogous to quantum dots.

To address this question, chapter 3.1 reviews superconductivity in general and introduces the topic of magnetic impurities and their use to create MBS in topological superconductors in particular. The detection of MBS with scanning probe microscopy techniques is discussed in detail, giving an overview of previously published literature in that field.

Thereafter, in chapter 3.2 the phenomenon of single-electron charging is characterized and a review of quantum dots and their observation as Coulomb rings with scanning probe microscopy techniques is given. Furthermore, the occurrence of an analogous behavior to quantum dots in molecular layers is reported and concluded as molecular quantum dots.

The experimental results of chapter 4 report on the systematic characterization by STM at low temperature (4.7 K) of the adsorption of carbon monoxide (CO) and sodium chloride (NaCl) as precondition for a more detailed investigation and manipulation of adsorbed Fe atoms on the superconducting Pb(111) surface. STM measurements show an absence of a topographic signature for CO molecules on Pb(111), which is imputed to their high tendency of diffusing under gentle scanning conditions. Nevertheless they contribute to a higher resolution if adsorbed to the scanning tip. In contrast, CO molecules on Pb(110) were observed by STM, which is supposed to be due to their adsorption in the trenches of the (110) surface.

Furthermore, it is shown that NaCl deposition on Pb(111) leads to bilayer islands similar to the literature data. Lastly, cold-temperature deposition ($\leq$ 15 K) of iron on Pb(111) leads to the adsorption of adatoms and small Fe clusters. Using tip-induced lateral manipulations, the exchange of Fe single atoms between these clusters is demonstrated and characterizes the variation of apparent STM height of each cluster as a function of the number of atoms.

All in all, the results on the adsorption of CO, NaCl and Fe upon the prototypical Pb superconducting surface provide new insights on high-resolution STM/AFM imaging with terminated tips, on decoupling of atomic and molecular adsorbates from fully conducting Pb substrates and on tip-induced lateral manipulation of single Fe atoms. Future investigations might succeed with the formation of Fe chains in various lengths and investigations of these chains with CO-functionalized tips.

The investigations of TBPP molecules on Pb(111), shown in chapter 5, indicate the possibility of single electron transfer in molecular layers, which is controllable by SPM methods. The TBPP layer has been atomically resolved and shows two different molecular arrangements, a straight (S) and a tilted (T) row. This is in analogy to measurements dealing with self-assembled TAPE layers on Ag(111) [28–30]. But while the TAPE/Ag(111) layer only shows charging events at the edges of the layer, the TBPP layer exhibits them in every S-row. This is again in analogy to a mixed TMTTF-TCNQ layer on Au(111) [27]. The array of Coulomb rings exhibits a periodic superstructure, which is not commensurate with the TBPP lattice and seems to originate from interactions between molecules and substrate. While on TMTTF-TCNQ/Au(111), the herring-bone reconstruction has been assumed as essential for the different graduation along molecular rows [27], it can be in the case of Pb mainly deduced to the mismatch between the Pb- and the TBPP-lattice.

The observed z-dependence of the Coulomb rings can be described with a simple plate capacitor model, which agrees well with the measurements for the investigated distances, but might not be transferred easily to small distances, as already discussed in the literature [29]. Nevertheless, the model illustrates the increase of the threshold voltage for larger distances and therefore underlines the necessity of SPM to control TBPP charge arrays. Overall, local discharging in TBPP seems very promising for applications in the field of quantum computing or quantum sensing. As an example, the high bit density of 0.7 bit/nm^2 can be considered (cf. figure 5.3).

In conclusion, the potential of Pb as a basis for the realization of qubits can thus be affirmed. In the field of Majorana bound states in atomic chains, a continuation of the investigations with the aim of being able to manipulate single atoms to chains on Pb seems desirable. For the investigation of quantum dots the results of this work clearly show that Pb can exhibit a confinement of electrons in adsorbed molecular layers. Further investigations regarding to the influence of superconductivity appear to be promising.

Bibliography

[1] Moore, G. E. Cramming more components onto integrated circuits. *Electronics* **38**, 114 (1965). URL https://cdn3.weka-fachmedien.de/media_uploads/documents/1429521922-13-gordonmoore1965article.pdf.

[2] Theis, T. N. & Wong, H.-S. P. The End of Moore's Law: A New Beginning for Information Technology. *Computing in Science Engineering* **19**, 41–50 (2017). URL https://doi.org/10.1109/MCSE.2017.29.

[3] Waldrop, M. M. The chips are down for Moore's law. *Nature News* **530**, 144 (2016). URL http://www.nature.com/news/the-chips-are-down-for-moore-s-law-1.19338. Section: News Feature.

[4] Deutsch, D. & Penrose, R. Quantum theory, the Church–Turing principle and the universal quantum computer. *Proceedings of the Royal Society of London. A. Mathematical and Physical Sciences* **400**, 97–117 (1985). URL https://royalsocietypublishing.org/doi/10.1098/rspa.1985.0070. Publisher: Royal Society.

[5] Feynman, R. P. Simulating physics with computers. *International Journal of Theoretical Physics* **21**, 467–488 (1982). URL https://doi.org/10.1007/BF02650179.

[6] Aumasson, J.-P. The impact of quantum computing on cryptography. *Computer Fraud & Security* **2017**, 8–11 (2017). URL https://www.sciencedirect.com/science/article/pii/S1361372317300519.

[7] Arute, F. *et al.* Quantum supremacy using a programmable superconducting processor. *Nature* **574**, 505–510 (2019). URL https://www.nature.com/articles/s41586-019-1666-5. Number: 7779 Publisher: Nature Publishing Group.

[8] Gambetta, J. IBM's Roadmap for Scaling Quantum Technology (2020). URL https://www.ibm.com/blogs/research/2020/09/ibm-quantum-roadmap/. Last revised: 7th May 2021.

[9] Gibney, E. Quantum gold rush: the private funding pouring into quantum start-ups. *Nature* **574**, 22–24 (2019). URL https://www.nature.com/articles/d41586-019-02935-4. Publisher: Nature Publishing Group.

[10] Loss, D. & DiVincenzo, D. P. Quantum computation with quantum dots. *Physical Review A* **57**, 120–126 (1998). URL https://link.aps.org/doi/10.1103/PhysRevA.57.120. Publisher: American Physical Society.

[11] Kloeffel, C. & Loss, D. Prospects for spin-based quantum computing in quantum dots. *Annual Review of Condensed Matter Physics* **4**, 51–81 (2013). URL https://doi.org/10.1146/annurev-conmatphys-030212-184248.

[12] Kitaev, A. Y. Unpaired Majorana fermions in quantum wires. *Physics-Uspekhi* **44**, 131–136 (2001). URL https://iopscience.iop.org/article/10.1070/1063-7869/44/10S/S29/meta.

[13] Majorana, E. Teoria simmetrica dell'elettrone e del positrone. *Il Nuovo Cimento* **14**, 171 (1937). URL https://doi.org/10.1007/BF02961314.

[14] Fu, L. & Kane, C. L. Superconducting Proximity Effect and Majorana Fermions at the Surface of a Topological Insulator. *Physical Review Letters* **100**, 096407 (2008). URL http://adsabs.harvard.edu/abs/2008PhRvL.100i6407F.

[15] Mourik, V. *et al.* Signatures of majorana fermions in hybrid superconductor-semiconductor nanowire devices. *Science* **336**, 1003–1007 (2012). URL https://science.sciencemag.org/content/336/6084/1003.

[16] Meissner, W. & Ochsenfeld, R. Ein neuer Effekt bei Eintritt der Supraleitfähigkeit. *Naturwissenschaften* **21**, 787–788 (1933). URL https://doi.org/10.1007/BF01504252.

[17] Nadj-Perge, S. *et al.* Observation of Majorana fermions in ferromagnetic atomic chains on a superconductor. *Science* **346**, 602–607 (2014). URL https://science.sciencemag.org/content/346/6209/602.

[18] Ruby, M. *et al.* End states and subgap structure in proximity-coupled chains of magnetic adatoms. *Phys. Rev. Lett.* **115**, 197204 (2015). URL https://link.aps.org/doi/10.1103/PhysRevLett.115.197204.

[19] Pawlak, R. *et al.* Probing atomic structure and Majorana wavefunctions in mono-atomic Fe chains on superconducting Pb surface. *npj Quantum Information* **2**, 16035 (2016). URL https://doi.org/10.1038/npjqi.2016.35.

[20] Kim, H. *et al.* Toward tailoring Majorana bound states in artificially constructed magnetic atom chains on elemental superconductors. *Science Advances* **4**, eaar5251 (2018). URL https://advances.sciencemag.org/content/4/5/eaar5251. Publisher: American Association for the Advancement of Science.

[21] Kamlapure, A., Cornils, L., Wiebe, J. & Wiesendanger, R. Engineering the spin couplings in atomically crafted spin chains on an elemental superconductor. *Nature Communications* **9**, 3253 (2018). URL https://www.nature.com/articles/s41467-018-05701-8. Number: 1 Publisher: Nature Publishing Group.

[22] Woodside, M. T. & McEuen, P. L. Scanned Probe Imaging of Single-Electron Charge States in Nanotube Quantum Dots. *Science* **296**, 1098–1101 (2002). URL https://science.sciencemag.org/content/296/5570/1098. Publisher: American Association for the Advancement of Science Section: Report.

[23] Nazin, G. V., Qiu, X. H. & Ho, W. Charging and Interaction of Individual Impurities in a Monolayer Organic Crystal. *Physical Review Letters* **95**, 166103 (2005). URL https://link.aps.org/doi/10.1103/PhysRevLett.95.166103.

[24] Pradhan, N. A., Liu, N., Silien, C. & Ho, W. Atomic Scale Conductance Induced by Single Impurity Charging. *Physical Review Letters* **94**, 076801 (2005). URL `https://link.aps.org/doi/10.1103/PhysRevLett.94.076801`. Publisher: American Physical Society.

[25] Cockins, L. *et al.* Energy levels of few-electron quantum dots imaged and characterized by atomic force microscopy. *Proceedings of the National Academy of Sciences* **107**, 9496–9501 (2010). URL `http://www.pnas.org/cgi/doi/10.1073/pnas.0912716107`.

[26] Song, C.-L. *et al.* Gating the charge state of single Fe dopants in the topological insulator Bi_2Se_3 with a scanning tunneling microscope. *Physical Review B* **86**, 045441 (2012). URL `https://link.aps.org/doi/10.1103/PhysRevB.86.045441`. Publisher: American Physical Society.

[27] Fernández-Torrente, I., Kreikemeyer-Lorenzo, D., Stróżecka, A., Franke, K. J. & Pascual, J. I. Gating the Charge State of Single Molecules by Local Electric Fields. *Physical Review Letters* **108**, 036801 (2012). URL `https://link.aps.org/doi/10.1103/PhysRevLett.108.036801`.

[28] Kocić, N. *et al.* Periodic Charging of Individual Molecules Coupled to the Motion of an Atomic Force Microscopy Tip. *Nano Letters* **15**, 4406–4411 (2015). URL `https://pubs.acs.org/doi/10.1021/acs.nanolett.5b00711`.

[29] Kocić, N., Decurtins, S., Liu, S.-X. & Repp, J. Forces from periodic charging of adsorbed molecules. *The Journal of Chemical Physics* **146**, 092327 (2017). URL `http://aip.scitation.org/doi/10.1063/1.4975607`.

[30] Kocić, N. *et al.* Implementing Functionality in Molecular Self-Assembled Monolayers. *Nano Letters* **19**, 2750–2757 (2019). URL `https://pubs.acs.org/doi/10.1021/acs.nanolett.8b03960`.

[31] Heavy metals in watercourses (2021). URL `https://www.bafu.admin.ch/bafu/en/home/topics/water/info-specialists/state-of-waterbodies/state-of-watercourses/water-quality-in-watercourses/heavy-metals-in-watercourses.html`. Publisher: Swiss Federal Office for the Environment FOEN, last revised: 7th May 2021.

[32] Binnig, G., Rohrer, H., Gerber, C. & Weibel, E. Tunneling through a controllable vacuum gap. *Applied Physics Letters* **40**, 178–180 (1982). URL `http://aip.scitation.org/doi/10.1063/1.92999`.

[33] Curie, J. & Curie, P. Développement par compression de l'électricité polaire dans les cristaux hémièdres à faces inclinées. *Bulletin de Minéralogie* **3**, 90–93 (1880). URL `https://www.persee.fr/doc/bulmi_0150-9640_1880_num_3_4_1564`. Publisher: Persée - Portail des revues scientifiques en SHS.

[34] Simpson, A. M. & Wolfs, W. Thermal expansion and piezoelectric response of PZT Channel 5800 for use in low-temperature scanning tunneling microscope designs. *Review of Scientific Instruments* **58**, 2193–2195 (1987). URL `https://doi.org/10.1063/1.1139486`.

[35] Binnig, G. & Rohrer, H. Scanning tunneling microscopy—from birth to adolescence. *Reviews of Modern Physics* **59**, 615–625 (1987). URL https://link.aps.org/doi/10.1103/RevModPhys.59.615. Publisher: American Physical Society.

[36] Binnig, G., Rohrer, H., Gerber, C. & Weibel, E. Surface studies by scanning tunneling microscopy. *Phys. Rev. Lett.* **49**, 57–61 (1982). URL https://link.aps.org/doi/10.1103/PhysRevLett.49.57.

[37] Binnig, G., Rohrer, H., Gerber, C. & Weibel, E. 7×7 Reconstruction on Si(111) Resolved in Real Space. *Phys. Rev. Lett.* **50**, 120–123 (1983). URL https://link.aps.org/doi/10.1103/PhysRevLett.50.120. Publisher: American Physical Society.

[38] Becker, R. S., Golovchenko, J. A. & Swartzentruber, B. S. Atomic-scale surface modifications using a tunnelling microscope. *Nature* **325**, 419–421 (1987). URL https://doi.org/10.1038/325419a0. Publisher: American Institute of Physics.

[39] Eigler, D. M. & Schweizer, E. K. Positioning single atoms with a scanning tunnelling microscope. *Nature* **344**, 524–526 (1990). URL http://www.nature.com/articles/344524a0.

[40] Repp, J., Meyer, G., Olsson, F. E. & Persson, M. Controlling the Charge State of Individual Gold Adatoms. *Science* **305**, 493 (2004). URL http://science.sciencemag.org/content/305/5683/493.abstract.

[41] Repp, J., Meyer, G., Stojković, S. M., Gourdon, A. & Joachim, C. Molecules on Insulating Films: Scanning-Tunneling Microscopy Imaging of Individual Molecular Orbitals. *Physical Review Letters* **94**, 026803 (2005). URL https://link.aps.org/doi/10.1103/PhysRevLett.94.026803.

[42] Merzbacher, E. The early history of quantum tunneling. *Physics Today* **55**, 44–49 (2002). URL https://doi.org/10.1063/1.1510281.

[43] Schottky, W. *Physikalische Zeitschrift* **32**, 833 (1931).

[44] Frenkel, J. *Wave Mechanics, Elementary Theory* (Clarendon Press, Oxford, UK, 1932).

[45] Hund, F. Zur Deutung der Molekelspektren. I. *Zeitschrift für Physik* **40**, 742–764 (1927). URL https://doi.org/10.1007/BF01400234.

[46] Hund, F. Zur Deutung der Molekelspektren. III. *Zeitschrift für Physik* **43**, 805–826 (1927). URL https://doi.org/10.1007/BF01397249.

[47] Nordheim, L. Zur Theorie der thermischen Emission und der Reflexion von Elektronen an Metallen. *Zeitschrift für Physik* **46**, 833–855 (1928). URL https://doi.org/10.1007/BF01391020.

[48] Frenkel, J. On the Electrical Resistance of Contacts between Solid Conductors. *Physical Review* **36**, 1604–1618 (1930). URL https://link.aps.org/doi/10.1103/PhysRev.36.1604.

[49] Wiesendanger, R. *Scanning Probe Microscopy and Spectroscopy* (Cambridge University Press, 1994).

[50] Chen, C. *Introduction to Scanning Tunneling Microscopy* (OUP Oxford, 2008).

[51] Bardeen, J. Tunnelling from a Many-Particle Point of View. *Physical Review Letters* **6**, 57–59 (1961). URL `https://link.aps.org/doi/10.1103/PhysRevLett.6.57`. Publisher: American Physical Society.

[52] Tersoff, J. & Hamann, D. R. Theory and Application for the Scanning Tunneling Microscope. *Physical Review Letters* **50**, 1998–2001 (1983). URL `https://link.aps.org/doi/10.1103/PhysRevLett.50.1998`. Publisher: American Physical Society.

[53] Chen, C. J. Theory of scanning tunneling spectroscopy. *Journal of Vacuum Science & Technology A* **6**, 319–322 (1988). URL `https://avs.scitation.org/doi/abs/10.1116/1.575444`. Publisher: American Vacuum Society.

[54] Besocke, K. An easily operable scanning tunneling microscope. *Surface Science* **181**, 145–153 (1987). URL `https://www.sciencedirect.com/science/article/pii/0039602887901518`.

[55] Frohn, J., Wolf, J. F., Besocke, K. & Teske, M. Coarse tip distance adjustment and positioner for a scanning tunneling microscope. *Review of Scientific Instruments* **60**, 1200–1201 (1989). URL `https://doi.org/10.1063/1.1140287`. `https://doi.org/10.1063/1.1140287`.

[56] Güntherodt, H.-J. & Wiesendanger, R. *Scanning Tunneling Microscopy I* (Springer-Verlag Berlin Heidelberg, 1992).

[57] Binnig, G. *et al.* Tunneling Spectroscopy and Inverse Photoemission: Image and Field States. *Physical Review Letters* **55**, 991–994 (1985). URL `https://link.aps.org/doi/10.1103/PhysRevLett.55.991`. Publisher: American Physical Society.

[58] Becker, R. S., Golovchenko, J. A. & Swartzentruber, B. S. Electron Interferometry at Crystal Surfaces. *Physical Review Letters* **55**, 987–990 (1985). URL `https://link.aps.org/doi/10.1103/PhysRevLett.55.987`.

[59] Vitali, L. *et al.* Portrait of the potential barrier at metal–organic nanocontacts. *Nature Materials* **9**, 320–323 (2010). URL `https://www.nature.com/articles/nmat2625`. Publisher: Nature Publishing Group.

[60] Binnig, G., Quate, C. F. & Gerber, C. Atomic Force Microscope. *Physical Review Letters* **56**, 930–933 (1986). URL `https://link.aps.org/doi/10.1103/PhysRevLett.56.930`. Publisher: American Physical Society.

[61] Schmaltz, G. Über Glätte und Ebenheit als physikalisches und physiologisches Problem. *Zeitschrift des Vereins Deutscher Ingenieure* **73**, 1461–1467 (1929). Publisher: Verein Deutscher Ingenieure (VDI).

[62] Young, R. D. Surface microtopography. *Physics Today* **24**, 42 (1971). URL `https://physicstoday.scitation.org/doi/abs/10.1063/1.3022432`. Publisher: American Institute of PhysicsAIP.

[63] Teague, E. C., Scire, F. E., Baker, S. M. & Jensen, S. W. Three-dimensional stylus profilometry. *Wear* **83**, 1–12 (1982). URL `https://www.sciencedirect.com/science/article/pii/0043164882903350`.

[64] Israelachvili, J. N. *Intermolecular and Surface Forces* (Elsevier, 2011). URL https://linkinghub.elsevier.com/retrieve/pii/C20090215601.

[65] Voigtländer, B. *Atomic Force Microscopy.* NanoScience and Technology (Springer International Publishing, 2019), 2 edn. URL https://www.springer.com/de/book/9783030136536.

[66] Giessibl, F. J. Advances in atomic force microscopy. *Reviews of Modern Physics* **75**, 949–983 (2003). URL https://link.aps.org/doi/10.1103/RevModPhys.75.949.

[67] Kavli Prize Laureates 2016. URL http://kavliprize.org/prize-landing/laureates/2016. Publisher: The Kavli Foundation.

[68] Meyer, E., Heinzelmann, H., Rudin, H. & Güntherodt, H. J. Atomic resolution on LiF (001) by atomic force microscopy. *Zeitschrift für Physik B Condensed Matter* **79**, 3–4 (1990). URL http://link.springer.com/10.1007/BF01387818.

[69] Albrecht, T. R., Grütter, P., Horne, D. & Rugar, D. Frequency modulation detection using high-Q cantilevers for enhanced force microscope sensitivity. *Journal of Applied Physics* **69**, 668–673 (1991). URL https://aip.scitation.org/doi/10.1063/1.347347. Publisher: American Institute of Physics.

[70] Giessibl, F. J. Atomic Resolution of the Silicon (111)-(7×7) Surface by Atomic Force Microscopy. *Science* **267**, 68–71 (1995). URL https://science.sciencemag.org/content/267/5194/68. Publisher: American Association for the Advancement of Science Section: Reports.

[71] Gross, L., Mohn, F., Moll, N., Liljeroth, P. & Meyer, G. The Chemical Structure of a Molecule Resolved by Atomic Force Microscopy. *Science* **325**, 1110–1114 (2009). URL https://www.sciencemag.org/lookup/doi/10.1126/science.1176210.

[72] Nonnenmacher, M., O'Boyle, M. P. & Wickramasinghe, H. K. Kelvin probe force microscopy. *Applied Physics Letters* **58**, 2921–2923 (1991). URL https://doi.org/10.1063/1.105227. Publisher: American Institute of Physics.

[73] Cugnon, J. The Casimir Effect and the Vacuum Energy: Duality in the Physical Interpretation. *Few-Body Systems* **53**, 181–188 (2012). URL https://doi.org/10.1007/s00601-011-0250-9.

[74] Hamaker, H. C. The London—van der Waals attraction between spherical particles. *Physica* **4**, 1058–1072 (1937). URL https://www.sciencedirect.com/science/article/pii/S0031891437802037.

[75] Hudlet, S., Saint Jean, M., Guthmann, C. & Berger, J. Evaluation of the capacitive force between an atomic force microscopy tip and a metallic surface. *The European Physical Journal B - Condensed Matter and Complex Systems* **2**, 5–10 (1998). URL https://doi.org/10.1007/s100510050219.

[76] Guggisberg, M. *et al.* Contrast inversion in nc-AFM on Si(111)7×7 due to short-range electrostatic interactions. *Applied Physics A* **72**, S19–S22 (2001). URL https://doi.org/10.1007/s003390100629.

[77] Gross, L. *et al.* Measuring the Charge State of an Adatom with Noncontact Atomic Force Microscopy. *Science* **324**, 1428–1431 (2009). URL `https://science.sciencemag.org/content/324/5933/1428`. Publisher: American Association for the Advancement of Science Section: Report.

[78] Bocquet, F., Nony, L. & Loppacher, C. Polarization effects in noncontact atomic force microscopy: A key to model the tip-sample interaction above charged adatoms. *Physical Review B* **83**, 035411 (2011). URL `https://link.aps.org/doi/10.1103/PhysRevB.83.035411`. Publisher: American Physical Society.

[79] Morse, P. M. Diatomic Molecules According to the Wave Mechanics. II. Vibrational Levels. *Physical Review* **34**, 57–64 (1929). URL `https://link.aps.org/doi/10.1103/PhysRev.34.57`. Publisher: American Physical Society.

[80] Guggisberg, M. *et al.* Separation of interactions by noncontact force microscopy. *Physical Review B* **61**, 11151–11155 (2000). URL `https://link.aps.org/doi/10.1103/PhysRevB.61.11151`.

[81] Pauli, W. Über den Zusammenhang des Abschlusses der Elektronengruppen im Atom mit der Komplexstruktur der Spektren. *Zeitschrift für Physik* **31**, 765–783 (1925). URL `https://doi.org/10.1007/BF02980631`.

[82] Martin, Y., Williams, C. C. & Wickramasinghe, H. K. Atomic force microscope–force mapping and profiling on a sub 100-Å scale. *Journal of Applied Physics* **61**, 4723–4729 (1987). URL `https://doi.org/10.1063/1.338807`. Publisher: American Institute of Physics.

[83] Zhong, Q., Inniss, D., Kjoller, K. & Elings, V. B. Fractured polymer/silica fiber surface studied by tapping mode atomic force microscopy. *Surface Science* **290**, L688 – L692 (1993). URL `http://www.sciencedirect.com/science/article/pii/0039602893905825`.

[84] Thomson (1st Baron Kelvin), W. Contact electricity of metals. *The London, Edinburgh, and Dublin Philosophical Magazine and Journal of Science* **46**, 82–120 (1898). URL `https://doi.org/10.1080/14786449808621172`. Publisher: Taylor & Francis.

[85] Sadewasser, S. & Glatzel, T. *Experimental Technique and Working Modes*. Springer Series in Surface Sciences (Springer International Publishing, Cham, 2018). URL `https://doi.org/10.1007/978-3-319-75687-5`.

[86] Weaver, J. M. R. High resolution atomic force microscopy potentiometry. *Journal of Vacuum Science & Technology B: Microelectronics and Nanometer Structures* **9**, 1559 (1991). URL `http://scitation.aip.org/content/avs/journal/jvstb/9/3/10.1116/1.585423`.

[87] Glatzel, T., Sadewasser, S. & Lux-Steiner, M. Amplitude or frequency modulation-detection in Kelvin probe force microscopy. *Applied Surface Science* **210**, 84–89 (2003). URL `https://linkinghub.elsevier.com/retrieve/pii/S0169433202014848`.

[88] Mohn, F., Gross, L., Moll, N. & Meyer, G. Imaging the charge distribution within a single molecule. *Nature Nanotechnology* **7**, 227–231 (2012). URL `https://www.nature.com/articles/nnano.2012.20`. Number: 4 Publisher: Nature Publishing Group.

[89] Schuler, B. *et al.* Contrast Formation in Kelvin Probe Force Microscopy of Single π-Conjugated Molecules. *Nano Letters* **14**, 3342–3346 (2014). URL https://doi.org/10.1021/nl500805x. Publisher: American Chemical Society.

[90] Burke, S. A. *et al.* Determination of the local contact potential difference of PTCDA on NaCl: a comparison of techniques. *Nanotechnology* **20**, 264012 (2009). URL https://doi.org/10.1088/0957-4484/20/26/264012. Publisher: IOP Publishing.

[91] Fauster, T., Hammer, L., Heinz, K. & Schneider, M. A. *Surface Physics* (De Gruyter Oldenbourg, 2020). URL https://www.degruyter.com/document/doi/10.1515/9783110636697/html.

[92] Knudsen, M. Die Gesetze der Molekularströmung und der inneren Reibungsströmung der Gase durch Röhren. *Annalen der Physik* **333**, 75–130 (1909). URL https://onlinelibrary.wiley.com/doi/abs/10.1002/andp.19093330106.

[93] Knudsen, M. Die Molekularströmung der Gase durch Öffnungen und die Effusion. *Annalen der Physik* **333**, 999–1016 (1909). URL https://onlinelibrary.wiley.com/doi/abs/10.1002/andp.19093330505.

[94] Becker, T., Hövel, H., Tschudy, M. & Reihl, B. Applications with a new low-temperature UHV STM at 5 K. *Applied Physics A* **66**, S27–S30 (1998). URL https://doi.org/10.1007/s003390051093.

[95] Meyer, G. A simple low-temperature ultrahigh-vacuum scanning tunneling microscope capable of atomic manipulation. *Review of Scientific Instruments* **67**, 2960–2965 (1996). URL https://aip.scitation.org/doi/abs/10.1063/1.1147080. Publisher: American Institute of Physics.

[96] Elrod, S. A., de Lozanne, A. L. & Quate, C. F. Low-temperature vacuum tunneling microscopy. *Applied Physics Letters* **45**, 1240–1242 (1984). URL https://aip.scitation.org/doi/abs/10.1063/1.95077. Publisher: American Institute of Physics.

[97] Giaever, I. Energy Gap in Superconductors Measured by Electron Tunneling. *Physical Review Letters* **5**, 147–148 (1960). URL https://link.aps.org/doi/10.1103/PhysRevLett.5.147. Publisher: American Physical Society.

[98] Giaever, I. Electron tunneling and superconductivity. *Reviews of Modern Physics* **46**, 245–250 (1974). URL https://link.aps.org/doi/10.1103/RevModPhys.46.245. Publisher: American Physical Society.

[99] Gaisch, R. *et al.* Low-temperature ultra-high-vacuum scanning tunneling microscope. *Ultramicroscopy* **42-44**, 1621–1626 (1992). URL https://www.sciencedirect.com/science/article/pii/0304399192904956.

[100] ScientaOmicron. LT STM – Ultimate SPM performance below 5 K (2017). URL https://scientaomicron.com/Downloads/Brochures/SPM/LT_STM_III_SO_Brochure_02_2017.pdf.

[101] Giessibl, F. J. High-speed force sensor for force microscopy and profilometry utilizing a quartz tuning fork. *Applied Physics Letters* **73**, 3956–3958 (1998). URL https://aip.scitation.org/doi/10.1063/1.122948. Publisher: American Institute of Physics.

[102] Giessibl, F. J. Vorrichtung zum berührungslosen Abtasten von Oberflächen und Verfahren dafür (1996). URL https://register.dpma.de/DPMAregister/pat/register?AKZ=196335469&CURSOR=14. Publisher: Deutsches Patent- und Markenamt, Patent Nr. DE 196 33 546 C 2.

[103] Giessibl, F. J. Atomic resolution on Si(111)-(7×7) by noncontact atomic force microscopy with a force sensor based on a quartz tuning fork. *Applied Physics Letters* **76**, 1470–1472 (2000). URL https://doi.org/10.1063/1.126067. Publisher: American Institute of Physics.

[104] Güthner, P., Fischer, U. C. & Dransfeld, K. Scanning near-field acoustic microscopy. *Applied Physics B* **48**, 89–92 (1989). URL https://doi.org/10.1007/BF00694423.

[105] Berger, J. *et al.* Characterization of the mechanical properties of qPlus sensors. *Beilstein Journal of Nanotechnology* **4**, 1–9 (2013). URL https://dx.doi.org/10.3762%2Fbjnano.4.1. Publisher: Beilstein Institut.

[106] Melmed, A. J. The art and science and other aspects of making sharp tips. *Journal of Vacuum Science & Technology B: Microelectronics and Nanometer Structures* **9**, 601 (1991). URL http://scitation.aip.org/content/avs/journal/jvstb/9/2/10.1116/1.585467.

[107] Biegelsen, D. K., Ponce, F. A., Tramontana, J. C. & Koch, S. M. Ion milled tips for scanning tunneling microscopy. *Applied Physics Letters* **50**, 696–698 (1987). URL https://aip.scitation.org/doi/abs/10.1063/1.98070. Publisher: American Institute of Physics.

[108] Bartels, L., Meyer, G. & Rieder, K.-H. Controlled vertical manipulation of single CO molecules with the scanning tunneling microscope: A route to chemical contrast. *Applied Physics Letters* **71**, 213–215 (1997). URL http://aip.scitation.org/doi/10.1063/1.119503.

[109] Gross, L. *et al.* Atomic Resolution on Molecules with Functionalized Tips. In Morita, S., Giessibl, F. J., Meyer, E. & Wiesendanger, R. (eds.) *Noncontact Atomic Force Microscopy: Volume 3*, NanoScience and Technology, 223–246 (Springer International Publishing, Cham, 2015). URL https://doi.org/10.1007/978-3-319-15588-3_12.

[110] Lee, H. J. & Ho, W. Single-Bond Formation and Characterization with a Scanning Tunneling Microscope. *Science* **286**, 1719–1722 (1999). URL https://science.sciencemag.org/content/286/5445/1719. Publisher: American Association for the Advancement of Science Section: Report.

[111] Nečas, D. & Klapetek, P. Gwyddion: an open-source software for SPM data analysis. *Open Physics* **10**, 181–188 (2012). URL https://www.degruyter.com/document/doi/10.2478/s11534-011-0096-2/html. Publisher: Versita Section: Open Physics.

[112] Wyckoff, R. W. G. *Crystal Structures - Volume 1.* (Interscience Publishers, New York, 1963), 2nd edn.

[113] Varga, P., Schmid, M. & Redinger, J. Hochauflösende Rastertunnelmikroskopie unterscheidet Atome. *Physik in unserer Zeit* **31**, 215–221 (2000). URL https://doi.org/10.1002/1521-3943(200009)31:5<215::AID-PIUZ215>3.0.CO;2-0.

[114] Schmid, M., Hebenstreit, W., Varga, P. & Crampin, S. Quantum Wells and Electron Interference Phenomena in Al due to Subsurface Noble Gas Bubbles. *Physical Review Letters* **76**, 2298–2301 (1996). URL `https://link.aps.org/doi/10.1103/PhysRevLett.76.2298`.

[115] Kamerlingh Onnes, H. *Phys. Lab. Univ. Leiden Suppl.* **29** (1911).

[116] Zhou, Z., Chu, S.-I. & Han, S. Quantum computing with superconducting devices: A three-level SQUID qubit. *Physical Review B* **66**, 054527 (2002). URL `https://link.aps.org/doi/10.1103/PhysRevB.66.054527`. Publisher: American Physical Society.

[117] Chiarello, F. Quantum computing with superconducting quantum interference devices: a possible strategy. *Physics Letters A* **277**, 189–193 (2000). URL `https://www.sciencedirect.com/science/article/pii/S0375960100007143`.

[118] Koch, R. H., DiVincenzo, D. P. & Clarke, J. Model for $1/f$ Flux Noise in SQUIDs and Qubits. *Physical Review Letters* **98**, 267003 (2007). URL `https://link.aps.org/doi/10.1103/PhysRevLett.98.267003`. Publisher: American Physical Society.

[119] Braumüller, J. *et al.* Characterizing and Optimizing Qubit Coherence Based on SQUID Geometry. *Physical Review Applied* **13**, 054079 (2020). URL `https://link.aps.org/doi/10.1103/PhysRevApplied.13.054079`. Publisher: American Physical Society.

[120] Beenakker, C. Search for Majorana Fermions in Superconductors. *Annual Review of Condensed Matter Physics* **4**, 113–136 (2013). URL `https://www.annualreviews.org/doi/10.1146/annurev-conmatphys-030212-184337`. Publisher: Annual Reviews.

[121] Veldhorst, M., Molenaar, C. G., Verwijs, C. J. M., Hilgenkamp, H. & Brinkman, A. Optimizing the Majorana character of SQUIDs with topologically nontrivial barriers. *Physical Review B* **86**, 024509 (2012). URL `https://link.aps.org/doi/10.1103/PhysRevB.86.024509`. Publisher: American Physical Society.

[122] Bardeen, J., Cooper, L. N. & Schrieffer, J. R. Microscopic Theory of Superconductivity. *Physical Review* **106**, 162–164 (1957). URL `https://link.aps.org/doi/10.1103/PhysRev.106.162`. Publisher: American Physical Society.

[123] Bardeen, J., Cooper, L. N. & Schrieffer, J. R. Theory of Superconductivity. *Physical Review* **108**, 1175–1204 (1957). URL `https://link.aps.org/doi/10.1103/PhysRev.108.1175`. Publisher: American Physical Society.

[124] Sigrist, M. & M. Rice, T. Paramagnetic Effect in High T c Superconductors -A Hint for d-Wave Superconductivity. *Journal of the Physical Society of Japan* **61**, 4283–4286 (1992). URL `https://journals.jps.jp/doi/abs/10.1143/JPSJ.61.4283`. Publisher: The Physical Society of Japan.

[125] Van Harlingen, D. J. Phase-sensitive tests of the symmetry of the pairing state in the high-temperature superconductors—Evidence for $d_{x^2-y^2}$ symmetry. *Reviews of Modern Physics* **67**, 515–535 (1995). URL `https://link.aps.org/doi/10.1103/RevModPhys.67.515`. Publisher: American Physical Society.

[126] Balian, R. & Werthamer, N. R. Superconductivity with Pairs in a Relative p Wave. *Physical Review* **131**, 1553–1564 (1963). URL https://link.aps.org/doi/10.1103/PhysRev.131.1553. Publisher: American Physical Society.

[127] Mackenzie, A. P. & Maeno, Y. p-wave superconductivity. *Physica B: Condensed Matter* **280**, 148–153 (2000). URL https://www.sciencedirect.com/science/article/pii/S092145269901546X.

[128] Talantsev, E. F. *et al.* p-wave superconductivity in iron-based superconductors. *Scientific Reports* **9**, 14245 (2019). URL https://www.nature.com/articles/s41598-019-50687-y. Number: 1 Publisher: Nature Publishing Group.

[129] Kamerlingh Onnes, H. *Phys. Lab. Univ. Leiden Suppl.* **133d** (1913).

[130] Suhl, H., Matthias, B. T. & Walker, L. R. Bardeen-Cooper-Schrieffer Theory of Superconductivity in the Case of Overlapping Bands. *Physical Review Letters* **3**, 552–554 (1959). URL https://link.aps.org/doi/10.1103/PhysRevLett.3.552. Publisher: American Physical Society.

[131] Choi, H. J., Roundy, D., Sun, H., Cohen, M. L. & Louie, S. G. The origin of the anomalous superconducting properties of MgB 2. *Nature* **418**, 758–760 (2002). URL https://www.nature.com/articles/nature00898. Number: 6899 Publisher: Nature Publishing Group.

[132] Floris, A., Sanna, A., Massidda, S. & Gross, E. K. U. Two-band superconductivity in Pb from ab initio calculations. *Physical Review B* **75**, 054508 (2007). URL https://link.aps.org/doi/10.1103/PhysRevB.75.054508. Publisher: American Physical Society.

[133] Ruby, M., Heinrich, B. W., Pascual, J. I. & Franke, K. J. Experimental Demonstration of a Two-Band Superconducting State for Lead Using Scanning Tunneling Spectroscopy. *Physical Review Letters* **114**, 157001 (2015). URL https://link.aps.org/doi/10.1103/PhysRevLett.114.157001. Publisher: American Physical Society.

[134] Sato, M. & Fujimoto, S. Majorana Fermions and Topology in Superconductors. *Journal of the Physical Society of Japan* **85**, 072001 (2016). URL https://journals.jps.jp/doi/full/10.7566/JPSJ.85.072001. Publisher: The Physical Society of Japan.

[135] Bogoljubov, N. N. On a new method in the theory of superconductivity. *Il Nuovo Cimento (1955-1965)* **7**, 794–805 (1958). URL https://doi.org/10.1007/BF02745585.

[136] De Gennes, P.-G. *Superconductivity of Metals and Alloys* (W.A. Benjamin, NewYork, 1966).

[137] Yu, L. Bound state in superconductors with paramagnetic impurities. *Acta Physica Sinica* **21.1**, 75 (1965). URL https://en.cnki.com.cn/Article_en/CJFDTotal-WLXB196501007.htm.

[138] Shiba, H. Classical Spins in Superconductors. *Progress of Theoretical Physics* **40**, 435–451 (1968). URL https://doi.org/10.1143/PTP.40.435.

[139] Rusinov, A. I. On the theory of gapless superconductivity in alloys containing paramagnetic impurities. *Soviet Physics JETP* **29**, 1101 (1969). URL http://www.jetp.ac.ru/cgi-bin/dn/e_029_06_1101.pdf.

[140] Andreev, A. F. Thermal conductivity of the intermediate state of superconductors. *Soviet Physics JETP* **20**, 1490 (1965). URL http://jetp.ac.ru/cgi-bin/dn/e_020_06_1490.pdf.

[141] Salkola, M. I., Balatsky, A. V. & Schrieffer, J. R. Spectral properties of quasiparticle excitations induced by magnetic moments in superconductors. *Physical Review B* **55**, 12648–12661 (1997). URL https://link.aps.org/doi/10.1103/PhysRevB.55.12648. Publisher: American Physical Society.

[142] Zitko, R., Bodensiek, O. & Pruschke, T. Effects of magnetic anisotropy on the subgap excitations induced by quantum impurities in a superconducting host. *Physical Review B* **83**, 054512 (2011). URL https://link.aps.org/doi/10.1103/PhysRevB.83.054512. Publisher: American Physical Society.

[143] Yazdani, A., Jones, B. A., Lutz, C. P., Crommie, M. F. & Eigler, D. M. Probing the Local Effects of Magnetic Impurities on Superconductivity. *Science* **275**, 1767–1770 (1997). URL https://science.sciencemag.org/content/275/5307/1767. Publisher: American Association for the Advancement of Science.

[144] Ji, S.-H. *et al.* High-Resolution Scanning Tunneling Spectroscopy of Magnetic Impurity Induced Bound States in the Superconducting Gap of Pb Thin Films. *Physical Review Letters* **100**, 226801 (2008). URL https://link.aps.org/doi/10.1103/PhysRevLett.100.226801. Publisher: American Physical Society.

[145] Ruby, M. *et al.* Tunneling Processes into Localized Subgap States in Superconductors. *Physical Review Letters* **115**, 087001 (2015). URL https://link.aps.org/doi/10.1103/PhysRevLett.115.087001. Publisher: American Physical Society.

[146] Heinrich, B. W., Pascual, J. I. & Franke, K. J. Single magnetic adsorbates on s-wave superconductors. *Progress in Surface Science* **93**, 1–19 (2018). URL https://www.sciencedirect.com/science/article/pii/S0079681618300017.

[147] Ruby, M., Peng, Y., von Oppen, F., Heinrich, B. W. & Franke, K. J. Orbital Picture of Yu-Shiba-Rusinov Multiplets. *Physical Review Letters* **117**, 186801 (2016). URL https://link.aps.org/doi/10.1103/PhysRevLett.117.186801. Publisher: American Physical Society.

[148] Alicea, J. New directions in the pursuit of majorana fermions in solid state systems. *Reports on Progress in Physics* **75**, 076501 (2012). URL https://doi.org/10.1088%2F0034-4885%2F75%2F7%2F076501.

[149] Dirac, P. A. M. The quantum theory of the electron. *Proceedings of the Royal Society of London. Series A, Containing Papers of a Mathematical and Physical Character* **117**, 610–624 (1928). URL https://royalsocietypublishing.org/doi/abs/10.1098/rspa.1928.0023. Publisher: Royal Society.

[150] Lutchyn, R. M., Sau, J. D. & Das Sarma, S. Majorana Fermions and a Topological Phase Transition in Semiconductor-Superconductor Heterostructures. *Physical Review Letters* **105**, 077001 (2010). URL `https://link.aps.org/doi/10.1103/PhysRevLett.105.077001`. Publisher: American Physical Society.

[151] Oreg, Y., Refael, G. & von Oppen, F. Helical Liquids and Majorana Bound States in Quantum Wires. *Physical Review Letters* **105**, 177002 (2010). URL `https://link.aps.org/doi/10.1103/PhysRevLett.105.177002`. Publisher: American Physical Society.

[152] Pientka, F., Glazman, L. I. & von Oppen, F. Topological superconducting phase in helical Shiba chains. *Physical Review B* **88**, 155420 (2013). URL `https://link.aps.org/doi/10.1103/PhysRevB.88.155420`.

[153] Klinovaja, J., Stano, P., Yazdani, A. & Loss, D. Topological Superconductivity and Majorana Fermions in RKKY Systems. *Physical Review Letters* **111**, 186805 (2013). URL `https://link.aps.org/doi/10.1103/PhysRevLett.111.186805`.

[154] Nadj-Perge, S., Drozdov, I. K., Bernevig, B. A. & Yazdani, A. Proposal for realizing Majorana fermions in chains of magnetic atoms on a superconductor. *Physical Review B* **88**, 020407 (2013). URL `https://link.aps.org/doi/10.1103/PhysRevB.88.020407`.

[155] Li, J. *et al.* Topological superconductivity induced by ferromagnetic metal chains. *Physical Review B* **90**, 235433 (2014). URL `https://link.aps.org/doi/10.1103/PhysRevB.90.235433`. Publisher: American Physical Society.

[156] Peng, Y., Pientka, F., Glazman, L. I. & von Oppen, F. Strong Localization of Majorana End States in Chains of Magnetic Adatoms. *Physical Review Letters* **114**, 106801 (2015). URL `https://link.aps.org/doi/10.1103/PhysRevLett.114.106801`. Publisher: American Physical Society.

[157] Hui, H.-Y., Brydon, P. M. R., Sau, J. D., Tewari, S. & Sarma, S. D. Majorana fermions in ferromagnetic chains on the surface of bulk spin-orbit coupled s-wave superconductors. *Scientific Reports* **5**, 8880 (2015). URL `https://www.nature.com/articles/srep08880`. Number: 1 Publisher: Nature Publishing Group.

[158] Sau, J. D. & Brydon, P. Bound States of a Ferromagnetic Wire in a Superconductor. *Physical Review Letters* **115**, 127003 (2015). URL `https://link.aps.org/doi/10.1103/PhysRevLett.115.127003`. Publisher: American Physical Society.

[159] Rokhinson, L. P., Liu, X. & Furdyna, J. K. The fractional a.c. Josephson effect in a semiconductor–superconductor nanowire as a signature of Majorana particles. *Nature Physics* **8**, 795–799 (2012). URL `https://www.nature.com/articles/nphys2429`. Number: 11 Publisher: Nature Publishing Group.

[160] Das, A. *et al.* Zero-bias peaks and splitting in an Al–InAs nanowire topological superconductor as a signature of Majorana fermions. *Nature Physics* **8**, 887–895 (2012). URL `https://www.nature.com/articles/nphys2479`. Number: 12 Publisher: Nature Publishing Group.

[161] Deng, M. T. *et al.* Anomalous Zero-Bias Conductance Peak in a Nb–InSb Nanowire–Nb Hybrid Device. *Nano Letters* **12**, 6414–6419 (2012). URL https://doi.org/10.1021/nl303758w. Publisher: American Chemical Society.

[162] Sarma, S. D., Freedman, M. & Nayak, C. Majorana zero modes and topological quantum computation. *npj Quantum Information* **1**, 1–13 (2015). URL https://www.nature.com/articles/npjqi20151. Publisher: Nature Publishing Group.

[163] Feldman, B. E. *et al.* High-resolution studies of the Majorana atomic chain platform. *Nature Physics* **13**, 286–291 (2017). URL https://www.nature.com/articles/nphys3947. Publisher: Nature Publishing Group.

[164] Jeon, S. *et al.* Distinguishing a Majorana zero mode using spin-resolved measurements. *Science* **358**, 772–776 (2017). URL https://science.sciencemag.org/content/358/6364/772. Publisher: American Association for the Advancement of Science.

[165] Ruby, M., Heinrich, B. W., Peng, Y., von Oppen, F. & Franke, K. J. Exploring a Proximity-Coupled Co Chain on Pb(110) as a Possible Majorana Platform. *Nano Letters* **17**, 4473–4477 (2017). URL https://doi.org/10.1021/acs.nanolett.7b01728. Publisher: American Chemical Society.

[166] Kleinert (Ruby), M. Magnetic Impurities on a Superconductor: from Single Atoms to Coupled Chains (2017). URL http://dx.doi.org/10.17169/refubium-5059. PhD Thesis, FU Berlin, Evaluator: Prof. Dr. Katharina J. Franke.

[167] Ruby, M., Heinrich, B. W., Peng, Y., von Oppen, F. & Franke, K. J. Wave-Function Hybridization in Yu-Shiba-Rusinov Dimers. *Physical Review Letters* **120**, 156803 (2018). URL https://link.aps.org/doi/10.1103/PhysRevLett.120.156803. Publisher: American Physical Society.

[168] Stroscio, J. A. & Eigler, D. M. Atomic and molecular manipulation with the scanning tunneling microscope. *Science* **254**, 1319–1326 (1991). URL https://science.sciencemag.org/content/254/5036/1319.

[169] Pawlak, R. *et al.* Single-Molecule Tribology: Force Microscopy Manipulation of a Porphyrin Derivative on a Copper Surface. *ACS Nano* **10**, 713–722 (2016). URL https://doi.org/10.1021/acsnano.5b05761.

[170] Pawlak, R. *et al.* Single-molecule manipulation experiments to explore friction and adhesion. *Journal of Physics D: Applied Physics* **50**, 113003 (2017). URL https://doi.org/10.1088/1361-6463/aa599d.

[171] Kawai, S. *et al.* Quantifying the atomic-level mechanics of single long physisorbed molecular chains. *Proceedings of the National Academy of Sciences* **111**, 3968–3972 (2014). URL http://www.pnas.org/content/111/11/3968.

[172] Kawai, S. *et al.* Superlubricity of graphene nanoribbons on gold surfaces. *Science* **351**, 957–961 (2016). URL http://science.sciencemag.org/content/351/6276/957.

[173] Pawlak, R. *et al.* Conformations and cryo-force spectroscopy of spray-deposited single-strand DNA on gold. *Nature Communications* **10**, 685 (2019). URL https://www.nature.com/articles/s41467-019-08531-4.

[174] Pawlak, R. *et al.* Sequential Bending and Twisting around C–C Single Bonds by Mechanical Lifting of a Pre-Adsorbed Polymer. *Nano Letters* **20**, 652–657 (2020). URL https://doi.org/10.1021/acs.nanolett.9b04418.

[175] Celotta, R. J. *et al.* Invited article: Autonomous assembly of atomically perfect nanostructures using a scanning tunneling microscope. *Review of Scientific Instruments* **85**, 121301 (2014). URL https://doi.org/10.1063/1.4902536.

[176] Khajetoorians, A. A., Wegner, D., Otte, A. F. & Swart, I. Creating designer quantum states of matter atom-by-atom. *Nature Reviews Physics* **1**, 703–715 (2019). URL https://www.nature.com/articles/s42254-019-0108-5.

[177] Limot, L., Kröger, J., Berndt, R., Garcia-Lekue, A. & Hofer, W. A. Atom Transfer and Single-Adatom Contacts. *Physical Review Letters* **94**, 126102 (2005). URL https://link.aps.org/doi/10.1103/PhysRevLett.94.126102. Publisher: American Physical Society.

[178] Hla, S. W. Atom-by-atom assembly. *Reports on Progress in Physics* **77**, 056502 (2014). URL https://doi.org/10.1088/0034-4885/77/5/056502. Publisher: IOP Publishing.

[179] Pawlak, R., Hoffman, S., Klinovaja, J., Loss, D. & Meyer, E. Majorana fermions in magnetic chains. *Progress in Particle and Nuclear Physics* **107**, 1–19 (2019). URL https://linkinghub.elsevier.com/retrieve/pii/S0146641019300316.

[180] van Houten, H. & Beenakker, C. W. J. Comment on "Conductance oscillations periodic in the density of a one-dimensional electron gas". *Physical Review Letters* **63**, 1893–1893 (1989). URL https://link.aps.org/doi/10.1103/PhysRevLett.63.1893. Publisher: American Physical Society.

[181] Kastner, M. A. *et al.* Kastner et al. reply:. *Physical Review Letters* **63**, 1894–1894 (1989). URL https://link.aps.org/doi/10.1103/PhysRevLett.63.1894. Publisher: American Physical Society.

[182] Glazman, L. I. & Shekhter, R. I. Coulomb oscillations of the conductance in a laterally confined heterostructure. *Journal of Physics: Condensed Matter* **1**, 5811–5815 (1989). URL https://doi.org/10.1088/0953-8984/1/33/027. Publisher: IOP Publishing.

[183] Kouwenhoven, L. P. *et al.* Single electron charging effects in semiconductor quantum dots. *Zeitschrift für Physik B Condensed Matter* **85**, 367–373 (1991). URL https://doi.org/10.1007/BF01307632.

[184] Kastner, M. A. The single-electron transistor. *Reviews of Modern Physics* **64**, 849–858 (1992). URL https://link.aps.org/doi/10.1103/RevModPhys.64.849. Publisher: American Physical Society.

[185] Zhu, J., Brink, M. & McEuen, P. L. Frequency shift imaging of quantum dots with single-electron resolution. *Applied Physics Letters* **87**, 242102 (2005). URL https://aip.scitation.org/doi/full/10.1063/1.2139623. Publisher: American Institute of Physics.

[186] Fallahi, P. *et al.* Imaging a Single-Electron Quantum Dot. *Nano Letters* **5**, 223–226 (2005). URL https://doi.org/10.1021/nl048405v. Publisher: American Chemical Society.

[187] Stomp, R. *et al.* Detection of Single-Electron Charging in an Individual InAs Quantum Dot by Noncontact Atomic-Force Microscopy. *Physical Review Letters* **94**, 056802 (2005). URL https://link.aps.org/doi/10.1103/PhysRevLett.94.056802.

[188] Dâna, A. & Yamamoto, Y. Electrostatic force spectroscopy of near surface localized states. *Nanotechnology* **16**, S125–S133 (2005). URL https://doi.org/10.1088/0957-4484/16/3/023. Publisher: IOP Publishing.

[189] Azuma, Y., Kanehara, M., Teranishi, T. & Majima, Y. Single Electron on a Nanodot in a Double-Barrier Tunneling Structure Observed by Noncontact Atomic-Force Spectroscopy. *Physical Review Letters* **96**, 016108 (2006). URL https://link.aps.org/doi/10.1103/PhysRevLett.96.016108. Publisher: American Physical Society.

[190] Zhu, J., Brink, M. & McEuen, P. L. Single-Electron Force Readout of Nanoparticle Electrometers Attached to Carbon Nanotubes. *Nano Letters* **8**, 2399–2404 (2008). URL https://pubs.acs.org/doi/10.1021/nl801295y.

[191] Fernández-Torrente, I., Franke, K. J. & Pascual, J. I. Vibrational Kondo Effect in Pure Organic Charge-Transfer Assemblies. *Physical Review Letters* **101**, 217203 (2008). URL https://link.aps.org/doi/10.1103/PhysRevLett.101.217203. Publisher: American Physical Society.

[192] Fu, Y.-S. *et al.* Identifying Charge States of Molecules with Spin-Flip Spectroscopy. *Physical Review Letters* **103**, 257202 (2009). URL https://link.aps.org/doi/10.1103/PhysRevLett.103.257202. Publisher: American Physical Society.

[193] Scheuerer, P., Patera, L. L. & Repp, J. Manipulating and Probing the Distribution of Excess Electrons in an Electrically Isolated Self-Assembled Molecular Structure. *Nano Letters* **20**, 1839–1845 (2020). URL https://doi.org/10.1021/acs.nanolett.9b05063. Publisher: American Chemical Society.

[194] Thouless, D. J. Maximum Metallic Resistance in Thin Wires. *Physical Review Letters* **39**, 1167–1169 (1977). URL https://link.aps.org/doi/10.1103/PhysRevLett.39.1167. Publisher: American Physical Society.

[195] Averin, D. V. & Likharev, K. K. Coulomb blockade of single-electron tunneling, and coherent oscillations in small tunnel junctions. *Journal of Low Temperature Physics* **62**, 345–373 (1986). URL https://doi.org/10.1007/BF00683469.

[196] Kastner, M. A. Artificial Atoms. *Physics Today* **46**, 24–31 (1993). URL https://physicstoday.scitation.org/doi/10.1063/1.881393. Publisher: American Institute of Physics.

[197] Meirav, U., Kastner, M. A., Heiblum, M. & Wind, S. J. One-dimensional electron gas in GaAs: Periodic conductance oscillations as a function of density. *Physical Review B* **40**, 5871–5874 (1989). URL https://link.aps.org/doi/10.1103/PhysRevB.40.5871. Publisher: American Physical Society.

[198] Foxman, E. B. *et al.* Effects of quantum levels on transport through a Coulomb island. *Physical Review B* **47**, 10020–10023 (1993). URL `https://link.aps.org/doi/10.1103/PhysRevB.47.10020`. Publisher: American Physical Society.

[199] Blick, R. H. *et al.* Single-electron tunneling through a double quantum dot: The artificial molecule. *Physical Review B* **53**, 7899–7902 (1996). URL `https://link.aps.org/doi/10.1103/PhysRevB.53.7899`. Publisher: American Physical Society.

[200] Leatherdale, C. A., Woo, W.-K., Mikulec, F. V. & Bawendi, M. G. On the Absorption Cross Section of CdSe Nanocrystal Quantum Dots. *The Journal of Physical Chemistry B* **106**, 7619–7622 (2002). URL `https://doi.org/10.1021/jp025698c`. Publisher: American Chemical Society.

[201] van Driel, A. F. *et al.* Frequency-Dependent Spontaneous Emission Rate from CdSe and CdTe Nanocrystals: Influence of Dark States. *Physical Review Letters* **95**, 236804 (2005). URL `https://link.aps.org/doi/10.1103/PhysRevLett.95.236804`. Publisher: American Physical Society.

[202] Bera, D., Qian, L., Tseng, T.-K. & Holloway, P. H. Quantum Dots and Their Multimodal Applications: A Review. *Materials* **3**, 2260–2345 (2010). URL `https://www.mdpi.com/1996-1944/3/4/2260`. Number: 4 Publisher: Molecular Diversity Preservation International.

[203] Bracker, A. S. *et al.* Binding energies of positive and negative trions: From quantum wells to quantum dots. *Physical Review B* **72**, 035332 (2005). URL `https://link.aps.org/doi/10.1103/PhysRevB.72.035332`. Publisher: American Physical Society.

[204] Hardman, R. A Toxicologic Review of Quantum Dots: Toxicity Depends on Physicochemical and Environmental Factors. *Environmental Health Perspectives* **114**, 165–172 (2006). URL `https://ehp.niehs.nih.gov/doi/10.1289/ehp.8284`. Publisher: Environmental Health Perspectives.

[205] Kouwenhoven, L. P. *et al.* Electron Transport in Quantum Dots. In Sohn, L. L., Kouwenhoven, L. P. & Schön, G. (eds.) *Mesoscopic Electron Transport*, NATO ASI Series, 105–214 (Springer Netherlands, Dordrecht, 1997). URL `https://doi.org/10.1007/978-94-015-8839-3_4`.

[206] Schönenberger, C. & Alvarado, S. F. Observation of single charge carriers by force microscopy. *Physical Review Letters* **65**, 3162–3164 (1990). URL `https://link.aps.org/doi/10.1103/PhysRevLett.65.3162`.

[207] Bachtold, A. *et al.* Scanned Probe Microscopy of Electronic Transport in Carbon Nanotubes. *Physical Review Letters* **84**, 6082–6085 (2000). URL `https://link.aps.org/doi/10.1103/PhysRevLett.84.6082`. Publisher: American Physical Society.

[208] Bockrath, M. *et al.* Resonant Electron Scattering by Defects in Single-Walled Carbon Nanotubes. *Science* **291**, 283–285 (2001). URL `https://science.sciencemag.org/content/291/5502/283`. Publisher: American Association for the Advancement of Science.

[209] Bleszynski, A. C. *et al.* Scanned Probe Imaging of Quantum Dots inside InAs Nanowires. *Nano Letters* **7**, 2559–2562 (2007). URL https://doi.org/10.1021/nl0621037. Publisher: American Chemical Society.

[210] Pioda, A. *et al.* Spatially Resolved Manipulation of Single Electrons in Quantum Dots Using a Scanned Probe. *Physical Review Letters* **93**, 216801 (2004). URL https://link.aps.org/doi/10.1103/PhysRevLett.93.216801. Publisher: American Physical Society.

[211] Ponomarenko, L. A. *et al.* Chaotic Dirac Billiard in Graphene Quantum Dots. *Science* **320**, 356–358 (2008). URL https://science.sciencemag.org/content/320/5874/356. Publisher: American Association for the Advancement of Science Section: Report.

[212] Brar, V. W. *et al.* Gate-controlled ionization and screening of cobalt adatoms on a graphene surface. *Nature Physics* **7**, 43–47 (2011). URL https://www.nature.com/articles/nphys1807. Number 1. Publisher: Nature Publishing Group.

[213] Wong, D. *et al.* Characterization and manipulation of individual defects in insulating hexagonal boron nitride using scanning tunnelling microscopy. *Nature Nanotechnology* **10**, 949–953 (2015). URL https://www.nature.com/articles/nnano.2015.188. Number: 11. Publisher: Nature Publishing Group.

[214] Qiao, J.-B. *et al.* Bound states in nanoscale graphene quantum dots in a continuous graphene sheet. *Physical Review B* **95**, 081409 (2017). URL https://link.aps.org/doi/10.1103/PhysRevB.95.081409.

[215] Bouvron, S. *et al.* Charge transport in a single molecule transistor probed by scanning tunneling microscopy. *Nanoscale* **10**, 1487–1493 (2018). URL https://pubs.rsc.org/en/content/articlelanding/2018/nr/c7nr06860c. Publisher: Royal Society of Chemistry.

[216] Velasco, J. *et al.* Visualization and Control of Single-Electron Charging in Bilayer Graphene Quantum Dots. *Nano Letters* **18**, 5104–5110 (2018). URL https://doi.org/10.1021/acs.nanolett.8b01972. Publisher: American Chemical Society.

[217] Walkup, D. *et al.* Tuning single-electron charging and interactions between compressible Landau level islands in graphene. *Physical Review B* **101**, 035428 (2020). URL https://link.aps.org/doi/10.1103/PhysRevB.101.035428. Publisher: American Physical Society.

[218] Li, H. *et al.* Imaging local discharge cascades for correlated electrons in WS2/WSe2 Moiré superlattices. *arXiv:2102.09986 [cond-mat]* (2021). URL http://arxiv.org/abs/2102.09986.

[219] Nazin, G. V., Qiu, X. H. & Ho, W. Vibrational spectroscopy of individual doping centers in a monolayer organic crystal. *The Journal of Chemical Physics* **122**, 181105 (2005). URL http://aip.scitation.org/doi/10.1063/1.1908719.

[220] Marczinowski, F., Wiebe, J., Meier, F., Hashimoto, K. & Wiesendanger, R. Effect of charge manipulation on scanning tunneling spectra of single Mn acceptors in InAs. *Physical Review B* **77**, 115318 (2008). URL https://link.aps.org/doi/10.1103/PhysRevB.77.115318. Publisher: American Physical Society.

[221] Steurer, W. *et al.* Manipulation of the Charge State of Single Au Atoms on Insulating Multilayer Films. *Physical Review Letters* **114**, 036801 (2015). URL `https://link.aps.org/doi/10.1103/PhysRevLett.114.036801`. Publisher: American Physical Society.

[222] Stolyarov, V. S. *et al.* Double Fe-impurity charge state in the topological insulator Bi_2Se_3. *Applied Physics Letters* **111**, 251601 (2017). URL `http://aip.scitation.org/doi/10.1063/1.5002567`.

[223] Wu, S. W., Nazin, G. V., Chen, X., Qiu, X. H. & Ho, W. Control of Relative Tunneling Rates in Single Molecule Bipolar Electron Transport. *Physical Review Letters* **93**, 236802 (2004). URL `https://link.aps.org/doi/10.1103/PhysRevLett.93.236802`.

[224] Swart, I., Sonnleitner, T. & Repp, J. Charge State Control of Molecules Reveals Modification of the Tunneling Barrier with Intramolecular Contrast. *Nano Letters* **11**, 1580–1584 (2011). URL `https://doi.org/10.1021/nl104452x`. Publisher: American Chemical Society.

[225] Steurer, W., Fatayer, S., Gross, L. & Meyer, G. Probe-based measurement of lateral single-electron transfer between individual molecules. *Nature Communications* **6**, 8353 (2015). URL `http://www.nature.com/articles/ncomms9353`.

[226] Amman, M., Wilkins, R., Ben-Jacob, E., Maker, P. D. & Jaklevic, R. C. Analytic solution for the current-voltage characteristic of two mesoscopic tunnel junctions coupled in series. *Physical Review B* **43**, 1146–1149 (1991). URL `https://link.aps.org/doi/10.1103/PhysRevB.43.1146`. Publisher: American Physical Society.

[227] Hanna, A. E. & Tinkham, M. Variation of the Coulomb staircase in a two-junction system by fractional electron charge. *Physical Review B* **44**, 5919–5922 (1991). URL `https://link.aps.org/doi/10.1103/PhysRevB.44.5919`. Publisher: American Physical Society.

[228] Nowak, M. P. & Szafran, B. Spin-orbit coupling effects in two-dimensional circular quantum rings: Elliptical deformation of confined electron density. *Physical Review B* **80**, 195319 (2009). URL `https://link.aps.org/doi/10.1103/PhysRevB.80.195319`. Publisher: American Physical Society.

[229] Steele, G. A. *et al.* Strong Coupling Between Single-Electron Tunneling and Nanomechanical Motion. *Science* **325**, 1103–1107 (2009). URL `https://science.sciencemag.org/content/325/5944/1103`. Publisher: American Association for the Advancement of Science Section: Report.

[230] Renaud, N., Hliwa, M. & Joachim, C. Single Molecule Logical Devices. In Metzger, R. M. (ed.) *Unimolecular and Supramolecular Electronics II: Chemistry and Physics Meet at Metal-Molecule Interfaces*, Topics in Current Chemistry, 217–268 (Springer, Berlin, Heidelberg, 2012). URL `https://doi.org/10.1007/128_2011_222`.

[231] Aviram, A. & Ratner, M. A. Molecular rectifiers. *Chemical Physics Letters* **29**, 277–283 (1974). URL `http://www.sciencedirect.com/science/article/pii/0009261474850311`.

[232] Meier, T. *et al.* Donor–Acceptor Properties of a Single-Molecule Altered by On-Surface Complex Formation. *ACS Nano* **11**, 8413–8420 (2017). URL https://doi.org/10.1021/acsnano.7b03954.

[233] Fuechsle, M. *et al.* A single-atom transistor. *Nature Nanotechnology* **7**, 242–246 (2012). URL https://doi.org/10.1038/nnano.2012.21.

[234] Gross, L. Recent advances in submolecular resolution with scanning probe microscopy. *Nature Chemistry* **3**, 273–278 (2011). URL https://www.nature.com/articles/nchem.1008.

[235] Heinrich, B. W., Braun, L., Pascual, J. I. & Franke, K. J. Protection of excited spin states by a superconducting energy gap. *Nature Physics* **9**, 765–768 (2013). URL https://www.nature.com/articles/nphys2794.

[236] Heinrich, B. W., Braun, L., Pascual, J. I. & Franke, K. J. Tuning the Magnetic Anisotropy of Single Molecules. *Nano Letters* **15**, 4024–4028 (2015). URL https://doi.org/10.1021/acs.nanolett.5b00987.

[237] Hirjibehedin, C. F., Lutz, C. P. & Heinrich, A. J. Spin Coupling in Engineered Atomic Structures. *Science* **312**, 1021–1024 (2006). URL https://science.sciencemag.org/content/312/5776/1021.

[238] Repp, J. *et al.* Charge-State-Dependent Diffusion of Individual Gold Adatoms on Ionic Thin NaCl Films. *Physical Review Letters* **117**, 146102 (2016). URL https://link.aps.org/doi/10.1103/PhysRevLett.117.146102.

[239] Jäck, B. *et al.* Observation of a Majorana zero mode in a topologically protected edge channel. *Science* **364**, 1255–1259 (2019). URL https://science.sciencemag.org/content/364/6447/1255. Publisher: American Association for the Advancement of Science.

[240] Palacio-Morales, A. *et al.* Atomic-scale interface engineering of Majorana edge modes in a 2D magnet-superconductor hybrid system. *Science Advances* **5**, eaav6600 (2019). URL https://advances.sciencemag.org/content/5/7/eaav6600. Publisher: American Association for the Advancement of Science.

[241] Chang, S. H. *et al.* Electronic growth of Pb islands on Si(111) at low temperature. *Physical Review B* **65**, 245401 (2002). URL https://link.aps.org/doi/10.1103/PhysRevB.65.245401.

[242] Song, S. Y. & Seo, J. Observation of enhanced superconductivity in the vicinity of Ar-induced nano-cavities in Pb(111). *Scientific Reports* **7**, 12177 (2017). URL https://www.nature.com/articles/s41598-017-12505-1.

[243] Pawlak, R. *et al.* Quantitative determination of atomic buckling of silicene by atomic force microscopy. *Proceedings of the National Academy of Sciences* **117**, 228–237 (2020). URL https://www.pnas.org/content/117/1/228.

[244] Auwärter, W. *et al.* A surface-anchored molecular four-level conductance switch based on single proton transfer. *Nature Nanotechnology* **7**, 41–46 (2012). URL https://www.nature.com/articles/nnano.2011.211.

[245] Choi, D.-J. *et al.* Mapping the orbital structure of impurity bound states in a superconductor. *Nature Communications* **8**, 15175 (2017). URL `https://www.nature.com/articles/ncomms15175`.

[246] Fremy-Koch, S. *et al.* Controlled switching of a single CuPc molecule on Cu(111) at low temperature. *Physical Review B* **100**, 155427 (2019). URL `https://link.aps.org/doi/10.1103/PhysRevB.100.155427`.

[247] Feng, M., Lin, C., Zhao, J. & Petek, H. Orthogonal intermolecular interactions of co molecules on a one-dimensional substrate. *Annu. Rev. Phys. Chem.* **63**, 201–224 (2012). URL `https://doi.org/10.1146/annurev-physchem-032210-103353`.

[248] Repp, J., Meyer, G. & Rieder, K.-H. Snell's Law for Surface Electrons: Refraction of an Electron Gas Imaged in Real Space. *Physical Review Letters* **92**, 036803 (2004). URL `https://link.aps.org/doi/10.1103/PhysRevLett.92.036803`.

[249] Hla, S.-W., Braun, K.-F. & Rieder, K.-H. Single-atom manipulation mechanisms during a quantum corral construction. *Physical Review B* **67**, 201402 (2003). URL `https://link.aps.org/doi/10.1103/PhysRevB.67.201402`.

[250] Hla, S.-W. Scanning tunneling microscopy single atom/molecule manipulation and its application to nanoscience and technology. *Journal of Vacuum Science & Technology B: Microelectronics and Nanometer Structures Processing, Measurement, and Phenomena* **23**, 1351–1360 (2005). URL `https://avs.scitation.org/doi/abs/10.1116/1.1990161`.

[251] Bartels, L., Meyer, G. & Rieder, K.-H. Basic Steps of Lateral Manipulation of Single Atoms and Diatomic Clusters with a Scanning Tunneling Microscope Tip. *Physical Review Letters* **79**, 697–700 (1997). URL `https://link.aps.org/doi/10.1103/PhysRevLett.79.697`.

[252] Emmrich, M. *et al.* Subatomic resolution force microscopy reveals internal structure and adsorption sites of small iron clusters. *Science* **348**, 308–311 (2015). URL `https://science.sciencemag.org/content/348/6232/308`.

[253] Kumar, A. *et al.* Electronic characterization of a charge-transfer complex monolayer on graphene. *ACS Nano* (2021). URL `https://doi.org/10.1021/acsnano.1c01430`.

Nomenclature

Symbols

Latin letters

A	Area
a, b	Lattice parameters
C	Capacitance
C_B	Capacitance between tip and molecule
C_T	Capacitance between tip and substrate
d	Distance
E	Energy
E_{LJ}	Lennard-Jones potential
E_F	Fermi energy
E_{vac}	Vacuum level
e	Elementary charge
e^-	Electron
F	Force
F_{chem}	Chemical force between tip and sample
F_{el}	Electrostatic force
F_{ts}	Total tip-sample force
F_{vdW}	Van der Waals force
f	Frequency
H	Hamaker constant
h	Height
i	Intercept
I_t	Tunneling current
k	Stiffness parameter
k_B	Boltzmann constant
L	Orbital angular momentum

m	Mass
p	Pressure
Q	Quality factor / charge
R	Radius of curvature of the tip
r	Radius
S	Total spin
s	Slope
T	Temperature
T_C	Critical temperature
U	Potential difference between tip and sample
V_B	Bias voltage
V_S	Bias sample voltage
x	Coordinate of one horizontal axis in the sample surface plane
y	Coordinate of one horizontal axis in the sample surface plane
z	Coordinate of the vertical axis between tip and sample
z_{offset}	Offset distance

Greek letters

α	Lever arm
Δ	Superconducting gap
Δf	Frequency shift
$\Delta\phi$	Work function difference
ε	Permittivity
θ	Angle between the lattice vectors
μ_s	Chemical surface potential
ρ	Electron density
Ψ	Total wave function
ω	Angular frequency of the oscillation

Abbreviations

AFM	Atomic force microscopy/microscope
AM	Amplitude-modulation
BCS	Bardeen-Cooper-Schrieffer
BE	Binding energy
CB	Coulomb blockade
CS	Coulomb staircase
CPD	Contact potential difference
DBTJ	Double barrier tunnel junction
DFT	Density functional theory
DOS	Density of states
fcc	Face centered cubic
FET	Field effect transistor
FIB	Focused ion beam
FM	Frequency-modulation
IGP	Ion getter pump
KPFM	Kelvin Probe Force Microscopy
KPFS	Kelvin Probe Force Spectroscopy
LCPD	Local contact potential difference
LDOS	Local density of states
LT	Low temperature
MBS	Majorana bound state
ML	Monolayer
MOSFET	Metal-oxide-semiconductor field-effect transistor
MZM	Majorana zero mode
NC	Non contact
PZT	Lead zirconate titanate
QD	Quantum dot
QMB	Quartz micro balance
QMB	Quartz tuning fork
qubit	Quantum bit
RT	Room temperature
SEM	Scanning electron microscopy/microscope
SET	Single electron transistor
SPM	Scanning probe microscopy/microscope
SQUID	Superconducting quantum interference device
STM	Scanning tunneling microscopy/microscope
STS	Scanning tunneling spectroscopy
TBPP	4,5,9,10-**t**etra**b**romo**p**yrimido[4,5,6-gh]**p**erimidine ($C_{12}H_2Br_4N_4$)
TCNQ	Tetracyanoquinodimethane

TM	Tapping mode
TMP	Turbo molecular pump
TSP	Titanium sublimation pump
TMTTF	Tetramethyltetrathiafulvalene
UHV	Ultra-high vacuum
YSR	Yu-Shiba-Rusinov
ZBCP	Zero-bias conductance peak
2D	Two-dimensional
3D	Three-dimensional

Acknowledgements

Last but not least, I want to thank everyone, who supported me during the work on this thesis. It was very great for me, that so many people helped me directly in scientific problems and in the evaluations or indirectly by moral support and encouragements.

First I want to thank Prof. Ernst Meyer, who gave me the opportunity to spend the last four years in his group. I always enjoyed it very much to work here and I would like to emphasize the excellent work atmosphere, which he significantly promotes. From the first interview on I always felt totally right in Basel, so that I have never regretted the decision to work here.

I also thank Prof. Katharina J. Franke to evaluate this thesis as external expert and Prof. Martino Poggio, Prof. Sabine Maier and PD Dr. Thilo Glatzel to complete the examination commission.

Special thanks go to Dr. Rémy Pawlak, who is also member of the examination commission and supervised me over the last four years. He introduced me to the LT-system, had always time to support me, proofread my drafts and was very patient with my questions and problems. It was great to work with him and I learned a lot from his enormous experimental experience.

I further like to acknowledge Roland Steiner, Yves Pellmont and the teams around Sascha Martin and Michael Steinacher from the workshops for their excellent support in mechanical or electronic problems. Special thanks go also to Dominik Sifrig and Patrick Stöcklin for providing liquid helium and nitrogen.

Additionally, I thank Dr. Shi-Xia Liu, Prof. Silvio Decurtins and their team from the University of Bern for providing me the molecules I investigated in this thesis and the good collaboration.

Acknowledgements

Of course I want to express my gratitude to all members of the Nanolino Group for the fruitful collaboration and the many nice contacts and conversations. In particular, I want to mention my colleagues Philipp D'Astolfo, who collaborated directly with me on the LT system and helped me both in scientific questions and organizing skiing excursions, Dr. Tobias Meier, who helped me getting started with the LT system and in the teaching, Dr. José Guilherme Vilhena, who was motivating me so often and became a very valuable companion not only in scientific questions, Germaine Weaver, who helped me very kindly in administrative questions and gave me a very warm welcome in the beginning and Dr. Thilo Glatzel, Dr. Antoine Hinaut, Dr. Sara Freund, Alexina Ollier and Marco Zutter, who shared the office 3.04 with me, helped me in scientific problems and contributed a lot to the fact that I always had a pleasure to work at the university.

In this context I want to mention particularly the wonderful excursions to the Blauenpass (2018), to Engelberg (2019) and Adelboden (2020, shortly before the pandemic!), the shared apartments at the DPG spring conferences in Berlin (2018) and Regensburg (2019), various joint Barbecue evenings and our daily lunch together in the mensa. All of this has come to an abrupt end due to the corona pandemic, but it should be resumed as soon as possible, since it characterizes the special "Nanolino spirit".

I would also like to take this opportunity to thank all of my friends, who I have met in Switzerland over the past four years and who I appreciate very much. They have contributed a lot to the fact that Switzerland has become a new home for me and that I now feel here just as familiar as in Bavaria. I would particularly like to mention my comrades in the table tennis club TTC Victoria Bottmingen, in the music club Bottmingen, in the catholic university parish Basel, as well as Gabriel Müggler and his family.

Finally, I thank all my relatives and further friends in Munich, Bremen, Graz, Berlin, Pragersko, Madrid and other places for their absolutely reliable, longstanding support and the diverse motivations via E-Mail, SMS, letter or even parcel (!). I want to mention in particular "an Mutz", "an Papa", "d'Adi", "d'Possi", "an Max" and "d'Mena", as well as Prof. Hans Bokelmann and Msgr. Georg Schuster, who have been the most inspiring role models to me.

List of publications & communications

Peer-reviewed journal publications

1. **Drechsel, C.**; D'Astolfo, P.; Liu, J.-C.; Liu, X.; Liu, S.-X.; Decurtins, S.; Pawlak, R.; Meyer, E. Observation of 2D molecular quantum dot arrays on superconducting Pb. *paper in preparation*

2. D'Astolfo, P.; Vilhena, J. G.; **Drechsel, C.**; Liu, X.; Decurtins, S.; Liu, S.-X.; Pawlak, R.; Meyer, E. On-surface synthesis and mechanical stabilization of sterically frustrated polymers. *paper in preparation*

3. Liu, J.-C.; Pawlak, R.; Wang, X.; D'Astolfo, P.; **Drechsel, C.**; Zhou, P.; Decurtins, S.; Aschauer, U.; Liu, S.-X.; Wulfhekel, W.; Meyer, E. Proximity-Induced Superconductivity in Atomically Precise Nanographene. *submitted* arXiv:2202.00460 **(2022)**. DOI: 10.48550/arXiv.2202.00460

4. **Drechsel, C.**; D'Astolfo, P.; Liu, J.-C.; Glatzel, Th.; Pawlak, R.; Meyer, E. Topographic signatures and manipulations of Fe atoms, CO molecules and NaCl islands on superconducting Pb(111). *Beilstein J. Nanotechnol.* **13,** 1-9 **(2022)**. DOI: 10.3762/bjnano.13.1

5. Pawlak, R.; Liu, X.; Ninova, S.; D'Astolfo, P.; **Drechsel, C.**; Liu, J.-C.; Häner, R.; Decurtins, S.; Aschauer, U.; Liu, S.-X.; Meyer, E. On-Surface Synthesis of Nitrogen-Doped Kagome Graphene. *Angew. Chem. Int. Ed.* **60,** 15, 8370-8375 **(2021)**. DOI: 10.1002/anie.202016469

6. Pawlak, R.; Liu, X.; Ninova, S.; D'Astolfo, P.; **Drechsel, C.**; Sangtarash, S.; Häner, R.; Decurtins, S.; Sadeghi, H.; Lambert, C. J.; Aschauer, U.; Liu, S.-X.; Meyer, E. Bottom-up Synthesis of Nitrogen-Doped Porous Graphene Nanoribbons. *J. Am. Soc.* **142,** 29, 12568-12573 **(2020)**. DOI: 10.1021/jacs.0c03946

7. Pawlak, R.; **Drechsel, C.**; D'Astolfo, P.; Kisiel, M.; Meyer, E.; Cerda, J. I. Quantitative determination of atomic buckling of silicene by atomic force microscopy. *PNAS* **117,** 1, 228-237 **(2019)**. DOI: 10.1073/pnas.1913489117

8. Blatnik, M.; **Drechsel, C.**; Tsud, N.; Surnev, S.; Netzer, F.P. Decomposition of Methanol on Mixed CuO-$CuWO_4$ Surfaces. *J. Phys. Chem. B* **122,** 2, 679-687 **(2018)**. DOI: 10.1021/acs.jpcb.7b06233

Talks

1. Controlled charging of self-assembled molecules on superconducting lead. **Drechsel, C.**; D'Astolfo, P.; Liu, J.-C.; Liu, X.; Liu, S.-X.; Decurtins, S.; Pawlak, R.; Meyer, E. *ICSPM28*, 2020–12–11, virtual, Japan.

2. Adsorption of atomic Fe-clusters on superconducting Pb. **Drechsel, C.**; Pawlak, R.; D'Astolfo, P.; Meyer, E. *DPG Spring Meeting 2019*, 2019–04–04, Regensburg, Germany.

Posters

1. Adsorption of atomic Fe-clusters on superconducting Pb. **Drechsel, C.**; Pawlak, R.; D'Astolfo, P.; Meyer, E. *Swiss NanoConvention 2019*, 2019–06–06, Lausanne, Switzerland.

2. Majorana bound states in monoatomic Fe-nanowires on superconducting Pb. **Drechsel, C.**; Pawlak, R.; Kisiel, M.; Klinowaja, J.; Meier, T., Kawai, S.; Glatzel, Th.; Loss, D.; Meyer, E. *ÖPG annual meeting*, 2018–09–11, Graz, Austria.

3. Majorana bound states in monoatomic Fe-nanowires on superconducting Pb. **Drechsel, C.**; Pawlak, R.; Kisiel, M.; Klinowaja, J.; Meier, T., Kawai, S.; Glatzel, Th.; Loss, D.; Meyer, E. *optima18*, 2018–04–09, Dresden, Germany.

4. Majorana bound states in monoatomic Fe-nanowires on superconducting Pb. **Drechsel, C.**; Pawlak, R.; Kisiel, M.; Klinowaja, J.; Meier, T., Kawai, S.; Glatzel, Th.; Loss, D.; Meyer, E. *DPG Spring Meeting 2018*, 2018–03–12, Berlin, Germany.

Awards at conferences

1. Best poster award at the *Swiss NanoConvention 2019*, sponsored by the Swiss Micro & Nanotechnology Network, 2019–06–06, Lausanne, Switzerland.

Curriculum Vitae

Name: Carl Ludwig Moritz Drechsel
Date of birth: February 27, 1991 in München-Pasing
Contact: carldrechsel[at]gmx.net

Education

2017 – 2021	PhD in Phyiscs, University of Basel, Switzerland
2014 – 2017	Master of Science in Physics, University of Graz, Austria
2010 – 2013	Bachelor of Science in Physics, University of Bremen, Germany
2010	Matriculation standard, Kippenberg-Gymnasium, Bremen, Germany

Teaching

2017 – 2021	Teaching assistant and full organization of exams, University of Basel – "Introduction to Physics I" (Mechanics, Thermodynamics) – "Einführung in die Physik II" (Electricity, Optics, Modern Physics)
2016	Tutor in the practical course, University of Graz – "Fortgeschrittene Experimentiertechniken" (Modern Physics)
2011 – 2013	Tutor for pre-courses and in the practical course, University of Bremen – "Physik für Elektrotechniker 1" (Mechanics) – "Physik für Elektrotechniker 2" (Optics, Thermodynamics)

Non-academic work experience

since 2021	Process Engineer (Advanced Packaging) Evatec AG, Trübbach, St. Gallen, Switzerland
2013 – 2014	Internship and employment as manager in "network planning" FlixBus GmbH, München, Bavaria, Germany